KU Leuven
Biomedical Sciences Group
Faculty of Medicine
Department of Cardiovascular Sciences

NOVEL BEAMFORMING METHODS FOR FAST VOLUMETRIC CARDIAC IMAGING USING ULTRASOUND

Alejandra ORTEGA CASTRILLON

Promoter: Prof. Jan D'hooge

Jury:
Prof. Stefan Janssens (chair)
Prof. Jens-Uwe Voigt
Prof. Paul Suetens
Prof. Piero Tortoli
Dr. Tore Grüner Bjåstad

Dissertation presented in partial fulfillment of the requirements for the degree of Doctor in biomedical sciences

December 2016

Acknowledgements

This journey started more than four years ago, and has been a constant and challenging learning process in many aspects of my life. During this thesis, I received a lot of help and support from many people and I would like to take the opportunity to thank them. It wouldn't have been possible without any of you.

To the members of the jury, I would like to express my gratitude for the interest and time taken to help me to improve my thesis. Professor Voigt and Professor Suetens, thank you very much for your guidance during my PhD. Both of you contributed significantly from your medical and engineering background, to make of this thesis a solid contribution to the biomedical field. Professor Tortoli and Doctor Bjåstad, thank you for giving me challenging comments which enhanced the quality of this thesis. It is an honor for me that the four of you are part of the examining committee.

To my supervisor, Professor Jan D'hooge. I deeply admire you as a researcher and as a person. You are one of the kindest and smartest people I know. Thank you for taking a chance on me and letting me be part of your '*dream team*'. It changed my life and took me to places I never expected to go. Your dedication to science, to your family, to the numerous sports that you practice and to us (your fellows), is inspiring. I have learned a lot under your guidance and I have gained many memories that will be always close to my heart. I owe you a lot, thank you.

Special thanks to Doctor Jean Provost and Doctor Mathieu Pernot, from the Institut Langevin in Paris, for helping me to corroborate our proposed methods on your research scanner. Thank you for all the time invested to make it work and for receiving me in your laboratory several times. I have learned a lot from our fruitful collaboration.

To the secretaries of the cardiology department, Christel and Karen. Thank you for helping me through the jungle of paperwork, administration and logistics over the years. Thank you for pushing things whenever I needed it urgently (very often to get my visa in order). You both were always very kind and helpful, I deeply appreciate it.

To my colleagues. One of the things that I enjoyed the most during my PhD, was the ability to work in an international group, including more than 17 nationalities. The fact that we were mostly foreigners created a very special bond between us. We could easily relate with what the other one was going through: the cultural shocks, the weather with its 4 seasons in a single day, the food from the cafeteria and for some of us the *witloof*. There was a lot of solidarity, understanding, support and curiosity about each-others cultural background. I learned a lot from all of you and your costumes. You all have largely contributed to making me a more open-minded person. I will never forget the tasty Tuesdays, a sweet excuse to share a treat together every week. Also, we were incredibly lucky to be able to share so many other learning spaces out of the lab, like the international conferences, and the summer and winter schools. Thank you for all the laughs and magnificent moments.

Ling, thank you for your time and your patience, I owe you almost everything I know about beamforming. You were always very helpful even while overseas. Natasa, thank you for allowing me to run several hundred simulations on your computer without asking for anything in return. I wouldn't have made it to the deadlines without you!. Also, thank you for the tasty and healthy dinners always accompanied by good wine. Natalia, who was going through all steps on the PhD

voyage at the same time as I did. Thank you for being so kind and considering. You always tried to make us happy by volunteering to make us presents (including delicious cakes). The fact that we went through this experience together while living in similar circumstances made it very special. Brecht, thank you for your moral support and pleasant company. Caro, it was very nice having you in the lab. You brought a special light in the group by being always so active and planning so many different after-work activities. Margot and Tom S., thank you for the after-work philosophical chats, it was something to look forward to every week. To the Portuguese gentlemen: Nuno, Pedro S., João, Pedro M., Sandro and Daniel. Every one of you is so kind, helpful and respectful that it makes me think that Portugal is something like wonderland. I still have to pay you a visit there though. João, I also want to thank you for taking me to beautiful places around Leuven while road-cycling, it really made me appreciate the Belgian landscapes. Also, thank you for being my hands in the lab when the remote access was not working, you were an angel in the difficult times!. Pedro S., thank you for the many inspiring conversations about beamforming and for always wearing a big smile. Bidisha, you are a very cool and joyful person. I enjoyed a lot of your company and I learned a lot about your culture. By the way, all my family remembers you for your outstanding dancing skills. Anna, thank you for being so sweet and caring. I really admire how sincere and direct you are. Thank you Hang, Adriyana, Raja, Jurgen, for all the joyful moments. Also to the ones that are no longer in the lab: Nina, Maja, Ruta, Guido, Frederick; Razavan, Oana, Martino; and to the ones that arrived when I was almost leaving: Vangjush, Mavesh and Hanan.

To the other researchers in the Louvre that I had the pleasure to meet. Stijn, thank you very much for enlightening me about so many different topics while on our way from/to the summing pool. You motivated me very often (not as often as we would have liked it) to take time for a refreshing break. Igor, your relaxed mood was contagious, always so: “don’t worry be happy”. I enjoyed our south American friendship which allowed me to complain about your national proud every time I could: Neymar. Matthew, you are one of the kindest people I met in the Louvre. You were always very considered and helpful. Thanks for all chats about the life (present and future), the LaTeX support and for reviewing my English every now and then. Professor Bogaert, thank you for cheering for Colombian in every sport event and for being so attentive about any news involving my country. Furthermore, thanks to all the other people whom I had the pleasure to meet and with whom I had many interesting conversations.

To my Colombian friends, whom despite of the distance have been with me in every step of this process. Ana, Karen, Juancho, Albert, Patas and Paula, thank you for making our friendship invariant to any change of geographic coordinates. I also want to express my gratitude to the friends I have made here. Tom B., my deepest gratitude with you for teaching me and helping me so much with C++. Thank you for all the time you invested in me and for your infinite patience. You are another kind, smart and sportive person to admire. Xochitl, a Spanish oasis in Leuven. It was always a relief to be able to speak in Spanish with you until we realized that so many people could understand our conversations! My friendship with you has been one of the things that made me learn the most in my development as a person, Gracias totales!. Dafne, thank you for your everlasting good mood and pleasant company. Thank you for taking care of me as if I were your little sister. All of you have been witness of the ups and downs of this roller coaster, and stood by me no matter what. Thank you all for your support in the difficult moments and for sharing my joy in the good times.

To the people I want to dedicate this thesis to: my family. A mí mamá y a mí papá, gracias por apoyarme siempre. Gracias por haberme dado tantas oportunidades a pesar de los sacrificios que estas requerían. Este logro es tan mío como suyo, sin ustedes nada de esto hubiera sido posible. Gracias por su acompañamiento incansable e incondicional. Gracias por haberme impulsado a salir a descubrir el mundo y dejarme hacer las cosas a mí manera. A mí hermana, gracias por enseñarnos

tanto de la vida y por tu generosa nobleza. Al papito, gracias por ser una fuente interminable de sabiduría y por enseñarnos la importancia del estudio. Los amo.

To my new family, Marc and Rosine, family Vanhees-Roose and family Leysen-Vanhees. Thank you very much for taking me into your family as one of yours. Your loving support and company have made it a lot easier to be so far from home. As from the first moment in Belgium, you all made me feel very welcome and you have done a lot of effort through the years to make me feel at home. I also want to thank the bigger family for being always so kind and caring. Thank you all for doing your best to make me feel comfortable in your country and accepting me into your family.

To my soulmate, my hubby, mi amorcito. Matthias, no words can express how lucky and grateful I am for having you in my life. Thank you for filling my life with love, happiness and adventure. Thank you for your support, help and understanding. Thank you for giving me all the best of you. Thank you for taking me with you to discover the world. You challenge me and inspire me to be a better person. I would not have taken as many risks, which led to so many great things without your support. As part of my family, I also want to dedicate this thesis to you. Ik hou van jou!.

Finally, I would like to acknowledge the financial support received from the European Research Council under the European Union's Seventh Framework programme (FP7/2007- 2013)/ERC Grant Agreement number 281748, which lead to the results of this thesis.

Abstract

Novel beamforming methods for fast volumetric cardiac imaging using ultrasound

Cardiovascular diseases are the leading cause of death in the world. There is thus a need for advanced diagnostic tools that allow for an early detection of such pathologies. In the last decade, volumetric (3D) cardiac ultrasound has gained clinical interest as it offers several advantages over the traditionally used 2D echocardiography. However, state-of-the-art 3D ultrasound scanners currently have a limited frame rate of approximately 20-25Hz despite of the fact that they acquire data over 4-6 consecutive cardiac cycles at reduced spatial resolution, and despite of the use of excessive parallel beamforming (16 and more).

Although these frame rates are typically sufficient to visualize global heart motion in real-time, they only describe cardiac kinematics in a very rough way as some of the cardiac phases are known to be associated with very fast motion and deformation of the cardiac muscle. With the available ultrasound methodologies, these cardiac phases can therefore not be studied accurately, while these time periods contain potentially important diagnostic information. It would thus be of both diagnostic and potentially therapeutic benefit to be able to study these short-lived cardiac phases in more detail. An imaging technique with an ultra-high temporal resolution (in the order of several hundreds of Hz) was therefore required.

Hence, the aim of this Ph.D. project was to develop novel beamforming methods to enable volumetric ultrasound cardiac imaging at high temporal resolution. More specifically, novel parallelized scan sequences were investigated. Their capability to generate 3D images with adequate image quality for functional myocardial imaging was demonstrated. Furthermore, an anatomical scan sequence was proposed to image the anatomical relevant space only at high frame rate. In this way, a frame rate of about 500-1000 Hz could be achieved.

Abstract

Nieuwe reconstructie methode voor snelle, volumetrische, cardiale beeldvorming met behulp van ultrasone golven

Cardiovasculaire aandoeningen zijn de voornaamste doodsoorzaak ter wereld. Er is dus nood aan een geavanceerde diagnostische methode voor vroegtijdige detectie van dergelijke aandoeningen. In het laatste decennium heeft volumetrische, cardiale beeldvorming aan klinische interesse gewonnen daar het verschillende voordelen biedt, vergeleken met 2D echocardiografie. Hoewel de nieuwste generatie 3D echocardiografische scanners data verzamelen gedurende 4 tot 6 opeenvolgende cardiale cycli aan een verminderde spatiale resolutie en met behulp van excessieve parallele reconstructie methoden (16 en meer), hebben deze scanners slechts een beperkte tijdsresolutie van ongeveer 20-25Hz.

Deze tijdsresolutie laat toe om de globale cardiale beweging te visualiseren in ‘real time’ en zodoende de cardiale kinematica rudimentair te beschrijven. Sommige mechanische, cardiale fasen zorgen echter voor zeer snelle bewegingen en vervormingen van de hartspier, die met de huidige echografische methoden niet (accuraat) bestudeerd kunnen worden waardoor er potentieel belangrijke diagnostische informatie verloren gaat. Het zou dus zowel diagnostisch als therapeutisch voordelig zijn om deze korte cardiale fasen meer gedetailleerd te kunnen bestuderen. Een beeldvormingstechniek met een ultra-hoge temporele resolutie (in de grootteorde van enkele honderden Hz) is daarvoor noodzakelijk.

Het doel van dit doctoraatswerk was daarom het ontwikkelen van een nieuwe reconstructie methode om volumetrische cardiale echografische beeldvorming aan hoge temporele resolutie toe te laten. Meer specifiek werden nieuwe geparallelizede scan’ sequenties onderzocht. Hun vermogen om 3D beelden te vormen met voldoende beeldkwaliteit voor functionele cardiale beeldvorming werd aangetoond. Bovendien werd een anatomische scan sequentie voorgesteld om enkel de anatomisch relevante gebieden aan hoge tijdsresolutie weer te geven. Zodoende zal een tijdsresolutie van ongeveer 500-1000Hz bereikt kunnen worden.

List of Acronyms

1D	One-dimensional
2D	Two-dimensional
3D	Three-dimensional
AWG	Arbitrary waveform generator
BPM	Beat per minute
BW	Beam width
CNR	Contrast-to-noise ratio
DW	Diverging wave imaging
ECG	Electrocardiography
FPS	Frame per second
HFR	High frame rate
Hz	Hertz
IR	Impulse response
IQ	In-phase Quadrature
IVC	Isovolumetric contraction
LV	Left ventricle
MI	Mechanical index
MLA	Multi-line acquisition
MLT	Multi-line transmit
PRF	Pulse repetition frequency
PSF	Point-spread-function
PW	Plane wave imaging
RF	Radio-frequency
ROI	Region of interest
US	Ultrasound
Vs	Versus
SLA	Single line acquisition
SLT	Single line transmit
SNR	Signal-to-noise ratio

Contents

1 Introduction

1.1 The Heart

The heart is a vital organ responsible for the circulation of blood through the vascular system. In this way, oxygen and nutrients are delivered to all cells in the body and carbon dioxide and other waste products can be removed. Both actions are essential for the correct functioning of the human body. The heart is located between the lungs, with its long axis slightly oriented forwards to the left in the thoracic cavity and it is roughly the size of a closed fist [1].

1.1.1 Cardiac anatomy

The heart is a muscular organ, which can be divided into three layers: endocardium, myocardium and epicardium being the inner, middle and outer layer respectively. The heart is enclosed by the pericardium, a fibrous sac containing pericardial fluid, which facilitates cardiac motion and reduces resistance with the epicardium. The myocardial tissue is composed of millions of cardiac *myocytes* (small contractile cells), which are arranged into fibers with a complex organization, i.e. a left and right hand helix on the endo/epicardial side resulting in fibers running longitudinal and the endo/epi and circumferential mid.

The internal anatomy of the heart, shown schematically in Fig. 1.1, can be divided based on its function into two pumps (left and right), each of them containing an upper chamber (atrium) and a lower chamber (ventricle). Both sides of the heart are separated by the *septal* wall.

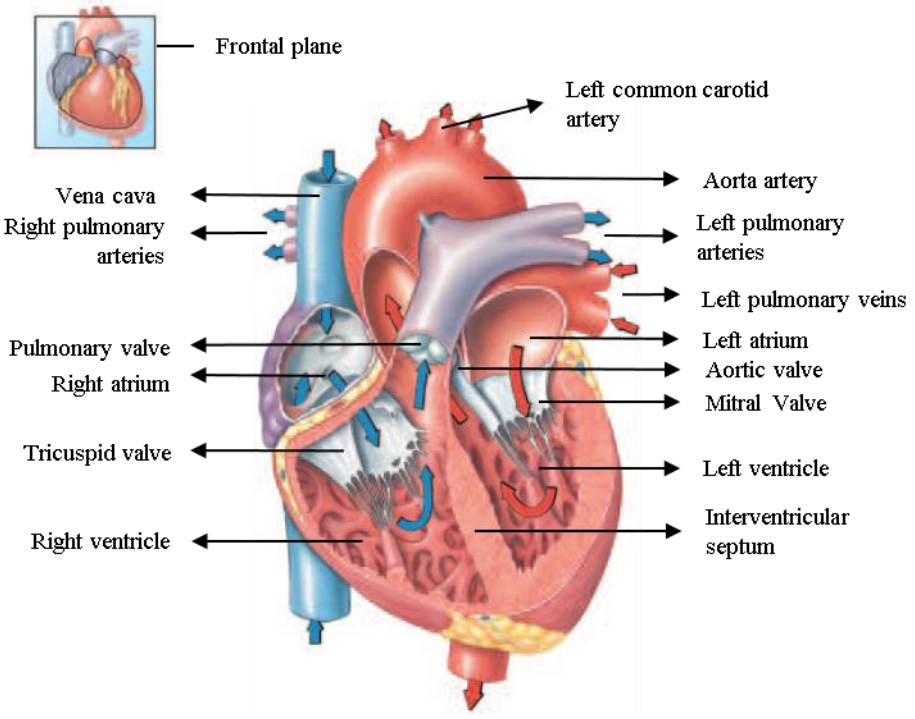

Fig 1.1. Schematic representation of the cardiac anatomy. Modified from [1] with permission.

Despite the anatomical differences between these two pumps, in general, they have a similar way of functioning: the atria are mainly collective chambers but with an important contractile function, while the ventricles have a more active role and are responsible for pumping the blood out of the heart to the rest of the body. The right heart receives the deoxygenated blood from the circulatory system through the inferior and superior vena cava and pumps it to the lungs to be re-oxygenated, while the left heart receives the oxygen-rich blood from the lungs and propels it to the whole body through the aortic artery. A network of coronary arteries is in charge of the oxygen-rich blood supply from the aorta to the myocardium, while the coronary veins are responsible for taking the deoxygenated blood from the myocardium to the coronary sinus and back to the heart's upper right chamber. Given that the left ventricle is responsible for pumping the oxygen-rich blood to the entire circulatory system and thus needs to develop higher pressures, its walls are significantly thicker than those of its right counterpart.

In order to maintain a unidirectional blood flow within the heart, a set of four valves open and close in a coordinated manner. The valve between the right atrium and right ventricle is called *tricuspid valve,* whereas the equivalent valve in the left heart is called *mitral valve.* Meanwhile, in the arteries leaving the heart there are the semilunar valves, the *aortic* (left heart) and the *pulmonary valve* (right heart). The leaflets of the atrio-ventricular valves are connected to the *papillary muscles* via the chordae tendineae, to avoid the valve of prolapsing and leaking blood retrograde into the atria (i.e. valve regurgitation) [2].

1.1.2 Cardiac conduction system

The pumping function of the heart is the result of the contraction and relaxation of the myocardium, which in turn occurs as a consequence of the redistribution of ions within the myocytes. This is associated with conformational changes of contractile proteins. The redistribution of ions can precisely be controlled through the *electrical conduction system* of the heart, which ensures a coordinated stimulation and therefore contraction of the different chambers to pump blood efficiently. The myocardial contraction is triggered in the right atrium by the spontaneous depolarization of the *sino-atrial node* (i.e. the natural "pacemaker"). This electrical impulse, or action potential, makes both atria contract simultaneously and then travels to the *atrio-ventricular node* where it is delayed to ensure that the ventricles are entirely filled before they contract. This depolarization wave continues towards the atrioventricular bundle or *Bundle of His* where it is branched into the left and right bundles along the interventricular septum. Finally, the action potential spreads in the ventricles through the Purkinje fibers. This event is repeated every heartbeat; different pacing mechanisms regulate its frequency.

1.1.3 Cardiac cycle

This electrical excitation makes a normal heart contract (i.e. beat) about 60-75 times per minute, implying that one cardiac cycle takes about 0.8s. The cardiac cycle can be divided into two main phases: *systole* (i.e. the contractile phase, takes about 0.3s), and *diastole* (i.e. relaxation phase, takes about 0.5s). The subsequent cardiac events, as they chronologically occur, are:

i) Isovolumetric contraction (IVC): just after the electrical excitation onset there is a short time delay, called electromechanical coupling phase, after which the ventricular cells start contracting. As a consequence, the pressure builds up rapidly within the ventricle to the point of surpassing the atrial pressure. Then, the atrio-ventricular valves close. This phase is a very short-lived (~ 30ms in a normal heart), where all the valves are closed and the pressure rises from 0 to about 80mmHg.

ii) Ventricular ejection: the ventricular pressure continues to increase until it exceeds the pressure in the arteries. As a result the semilunar valves open and the right and left ventricle eject blood to the lungs and the body respectively.
iii) Isovolumetric relaxation (IVR): towards the end of systole, the pressure starts to decrease and both the aortic and pulmonary valves close. This is also a short-lived event (~80ms), where all the valves are closed and the ventricle starts to relax. Simultaneously, the atria start filling and the atrial pressure increases.
iv) Rapid passive ventricular filling: once the ventricular pressure drops below the atrial pressure, the atrio-ventricular valves open and the blood is quickly sucked into the ventricles. About 60-75% of the filling takes place at this stage [3].
v) Diastasis: the filling continues but at a reduced rate given that the whole heart is at rest.
vi) Atrial contraction: at this stage the sino-atrial node depolarizes and the atria contract to finish filling the ventricles. About 20% of the remaining filling takes place [4] and the cardiac cycle starts over.

These six steps of the cardiac cycle are schematically represented in Fig. 1.2, as described by Dr. D. Penney.

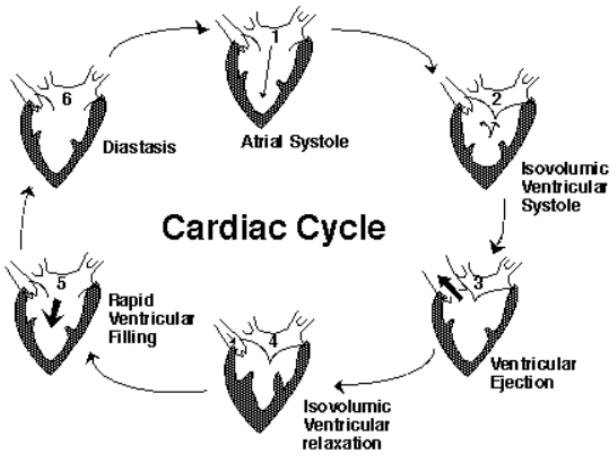

Fig. 1.2. Schematic of the cardiac cycle as described by Dr. D. Penney. Reproduced with permission.

1.1.4 Heart failure

Cardiovascular diseases (CVDs) are a group of disorders affecting the heart and blood vessels and are the number one cause of death globally (nearly the 30%) [5]. In last years, CVDs have extended to people from all socio-economical levels due to rising behavioral risk factors such as tobacco use, unhealthy diet and obesity, physical inactivity and harmful use of alcohol [6][7]. Usually, the presence of a combination of the above-mentioned risk factors and hypertension, diabetes and/or hyperlipidemia, are the cause heart attacks and strokes. Heart failure is also among these disorders, it is most often associated with an unsynchronized contraction of the heart due to problems with the cardiac conduction system. This lack of synchronization leads to further inefficiency of the cardiac pump function.

1.2 Cardiac Ultrasound Imaging

Historically, ultrasonic imaging has made its way from the acoustic detection of submarines (i.e. sonar) during the First World War, to nondestructive testing methods of metals for industrial applications, to the visualization of the morphology and anatomy of organs as well as assessing

their function in clinical practice. In the last decades, it has become a primordial medical imaging modality, thanks to its unique ability of providing noninvasive images in real-time, its good tradeoff between spatial and temporal resolution, its low-cost compared to other imaging modalities, the portability of its equipment, and the safeness for the patient and the practitioner.

Nowadays, cardiac ultrasound imaging (or echocardiography) is the most commonly used imaging modality to visualize and assess the function of the heart, with two-dimensional (2D) echocardiography being the standard method of care [8]. Furthermore, in the last decades, ultrasound imaging has continued to evolve rapidly with major developments in – for example – volumetric (three-dimensional, 3D) cardiac ultrasound that has gained impact on clinical practice.

1.2.1 Physical principles

Ultrasonic waves, also called ultrasound (US), are longitudinal compression waves with a frequency above the audible range of the human hearing, i.e., higher than 20 kHz. Such waves can be generated and detected by piezoelectric crystals, which are able to convert an electric field into mechanical motion, and vice versa. Ultrasound imaging relies on the interaction between the acoustical wave and the tissues in the human body. As the wave travels through the body, it gets partially reflected and refracted whenever it encounters the interface between two media with different acoustic properties (acoustic impedance mismatch). The acoustic impedance (Z) is the opposition that the media presents to the acoustic flow. It is defined as the product of the density of the media (ρ) and the speed of sound (c):

$$Z = \rho c. \tag{1.1}$$

Therefore, the greater the difference between the impedances of the two media, the stronger the reflection and the weaker the transmission. In general, the difference in acoustic properties among soft tissues is rather small, thus most of the energy is effectively transmitted, and the reflected signals are referred to as *specular reflections* [9]. However, reflections do not only occur at tissue boundaries but also appear when the energy of the wave gets scattered while it travels through a media with local acoustic inhomogeneities (i.e., spatial fluctuations in compressibility and/or mass density). This kind of interaction is called *scatter reflections.* Depending on the shape of the inhomogeneity (or scatterer) and its size, relative to the wavelength of the ultrasonic wave, the energy of the acoustic wave is scattered in different directions. If the scatterers retransmit the energy uniformly in all directions, they are referred to as point scatterer. Typically, scatter reflections in soft tissue are much smaller in amplitude than specular reflections [10].

Next to the above described reflections, there are other phenomena that take place during wave propagation or its interaction with tissue such as *refraction*, *diffraction*, *dispersion*, *nonlinear distortion* and *absorption.* Most of these interactions result mainly in the attenuation of the acoustic energy of the wave which limits its propagation in depth. In soft tissue, this attenuation is converted in heat and is primarily due to viscosity. However, diffraction is the result of the interference of a large number of coherent sources. When this interference is adequately manipulated it can be used to focus the acoustic beam creating a peak pressure at a desired point.

1.2.2 Pulse-echo measurement

The underlying fundamental principle of ultrasound imaging is the reconstruction of the reflected signals (or echoes), which carry important information regarding the different tissues that the acoustic wave encounters during its propagation. This information includes acoustic properties, spatial location, tissue boundaries and surrounding media. Essential to disclosing this information, is the determination of the distance between the source of the acoustic wave and the structure that is generating the echo. This distance, *d*, can easily be calculated using the speed of sound, *c*, which is approximately 1540 m/s in soft tissue [11], and the time delay, *t*, between the instant that the

acoustic wave was transmitted and the instant that its echo was recorded. Mathematically, this can be defined as:

$$d = \frac{ct}{2}. \tag{1.2}$$

1.2.3 Phased array transducer

Typically, the same piezoelectric crystal that is used to generate the acoustic wave is also used to detect the energy reflected from the tissue. Indeed, immediately after the crystal has transmitted the ultrasonic wave it is able to start receiving echoes. In modern US systems, an array of these crystals are embedded in a so-called *transducer* or *probe*, which gives a good control on radiation patterns. These crystals are made to be as small as the wavelengths of the ultrasonic wave that they can transmit and receive, and therefore the waves emitted are approximately spherical. The ultrasonic transducers can only transmit and receive a limited band of frequencies; this band is called the bandwidth of the transducer and its center is the central frequency of the transducer. The frequencies of the detected signals correspond to radio waves in the electromechanical spectrum, and are therefore called radiofrequency (RF) signals.

Phased array transducers allow to control the individual elements of the array electronically. Hence, the delays and/or the amplitudes of the spherical waves emitted by different array elements can be easily manipulated to generate a controlled interference pattern. In this way, the transmitted beam can be steered and focused, and the sensitivity of the transducer can be directed while receiving. Phased array transducer are preferred for cardiac applications because of their small footprint (required to fit in the limited acoustic window between the ribs), but at the same time, their capability to provide a rather large field-of-view (FOV) thanks to electronic steering of the ultrasonic beams. Typically, the piezoelectric crystals are arranged as one-dimensional (1D) or 2D rectangular arrays with an inter-element spacing of about half of the central wavelength of the transducer. The conventional 1D and 2D phased array transducer and their respective FOV are illustrated in Fig. 1.3.

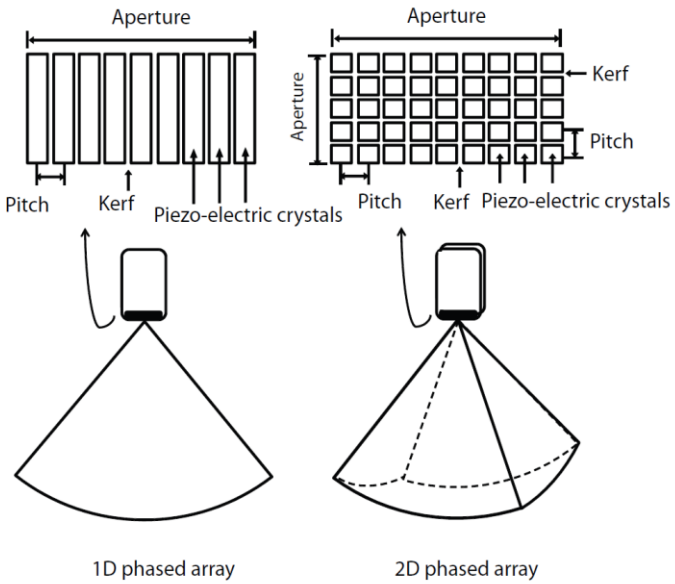

Fig. 1.3 Typical ultrasound 1D (left) and 2D (right) phased array transducers and their corresponding field-of-view. Reproduced with permission from [12].

1.2.4 Data acquisition

In order to generate an image, several pulse-echo measurements are performed along a single or multiple directions. There are three basic imaging modes:

A-mode. Stands for *amplitude imaging* and corresponds to the information of the scanned object along one-dimension. It is the simplest form of ultrasound imaging, where the pulse-echo measurements are performed along a single direction and the reflections are recorded as a function of time.

M-mode. Stands for *motion imaging* and yields a 2D image with time and depth as dimensions. It is performed as a repetition of A-mode images but the received echoes are encoded to gray scales and displayed as an image line in the vertical direction. The final image is the sequential composition of the image lines. Any movement of the scanned object is therefore recorded.

B-mode. Stands for *brightness imaging* and it contains 2D or 3D information of the scanned object. Although it is similar to M-mode imaging, it differs from that the image lines correspond to pulse-echo measurements along different directions. It is the most common imaging mode used in clinical practice for cardiac imaging. The typical FOV created is a fan like sector (for 2D imaging), and a pyramid-like volume (for 3D imaging); for both with the tip being the center of the transducer. Its dimensions are: *axial*, along a given image line, *azimuthal*, perpendicular to the image line within the imaging plane, and *elevation* perpendicular to the imaging plane.

All these imaging modes can also be used for *second-harmonic imaging*, which differs from conventional US imaging in that only the low-frequency of the bandwidth of the transducer is used in transmission. Therefore, higher harmonics are generated during the non-linear wave propagation since the transmit pulses get distorted the further they propagate in the tissue, the higher frequencies built up. Given that reverberations and side lobes either do not contain harmonics or are too low in amplitude, this imaging modality significantly increases image quality for transthoracic scans of the heart (especially in corpulent patients).

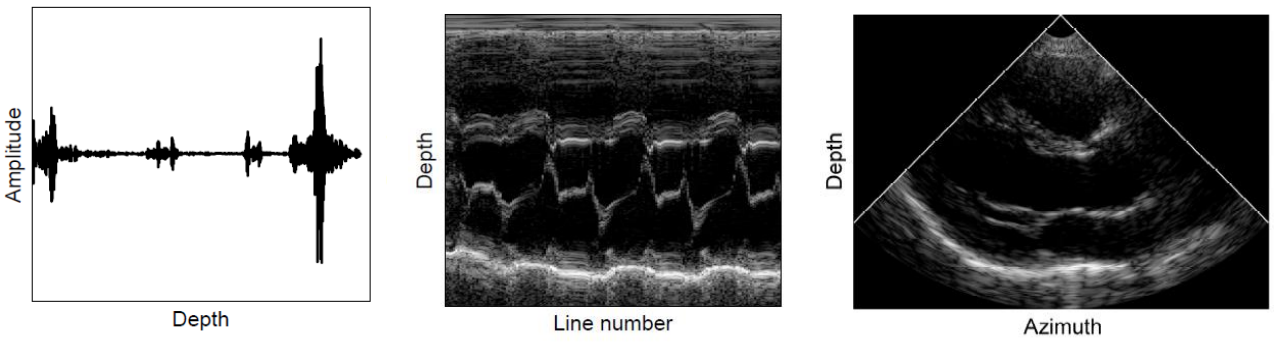

(a) A-mode (b) M-mode (c) B-mode

Fig. 1.4. Data acquisition imaging modes: (a) A-mode, (b) M-mode, (c) B-mode. Reproduced with permission from [12].

1.2.5 Image reconstruction

In order to reconstruct B-mode images, the acquired RF signals undergo several processing steps to become image lines and to finally form the image. First, the signals are *filtered* to remove all high-frequencies noise. Then, the high-frequency information of the filtered signal is also removed by *envelope detection*. This is done because the very fast fluctuations of the RF signals are not relevant

for gray-scale imaging. The envelope detection can be done by means of the Hilbert transformation. However, as this is an expensive process computationally, some real-time applications use more efficient algorithms that involve down mixing, filtering, decimating and detecting the data. Afterwards, given that the echoes from deeper structures are weaker due to attenuation of the incident wave, the attenuation of the media is estimated and a respective compensation is performed to ensure that structures with similar acoustic properties appear with a similar gray value throughout the image. This is called *attenuation correction* or *time gain compensation* because of the linear relation between time and depth in echography. Later, a gray scale transformation is made to reduce the large dynamic range of the signals caused by the very different amplitudes of the scatter and specular reflections, and further *gray scale encode* the signals, this transformation is typically done by *log-compression.* Finally, typically the received signals are coming from different angular directions. Therefore, the resulting image lines are transformed from polar (in 2D) or spherical (in 3D) coordinates to Cartesian coordinates for display, which requires interpolation. This latter process is referred to as *scan conversion*.

1.2.6 Basics of beamforming

Based on the Huygens' principle the transducer surface can be seen as a collection of point sources transmitting spherical waves. Therefore, the resulting interference patterns can easily be modified by manipulating the phase and/or amplitudes of the spherical waves emitted by different array elements in order to create a beam-like transmission. In the same way, the sensitivity of the system can be directed by adapting the signals received by individual elements (Fig. 1.5(a)). This process is referred to as *beamforming* and acts as a spatial filtering process through directive transmission or reception of energy (Fig. 1.5(b)).

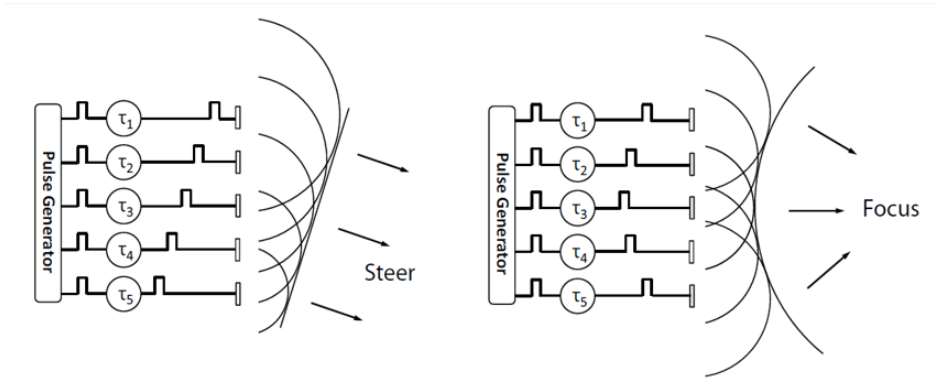

(a) Receive

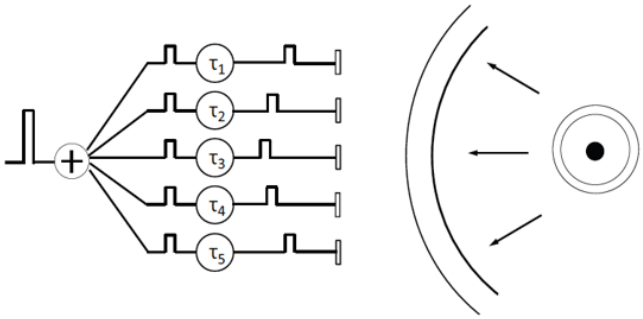

(b) Beamforming

Fig. 1.5. Schematic illustration of the transmit (a), and receive (b) beamforming. Reproduced with permission from [12].

Transmit beamforming

To create a focused beam, the wavefronts of the spherical waves emitted by each element in the transducer should arrive at the same time at a given focal point. This leads to constructive interference of the waves at that point and therefore to a local increase of pressure. Such interference pattern can easily be manipulated by delaying the electrical pulses applied on individual elements of an array transducer. The transmit delay (τ_i^{tx}) that needs to be applied to the i^{th}element in the array can be calculated as:

$$\tau_i^{tx} = \frac{\sqrt{(x_i - p_{fx})^2 + (y_i - p_{fy})^2 + (z_i - p_{fz})^2} - |p_f|}{c}, \tag{1.3}$$

where (x_i, y_i, z_i) is the spatial position of the i^{th} element in the transducer, p_f is the distance from the focus point to the center of the transducer, and c is the sound speed.

Receive beamforming

The same method as the one to beamform the transmitted energy can be applied to the received signals. The received echoes detected by different elements can be delayed in order to align their phases and enhance the energy coming from a desired direction. Moreover, unlike transmit beamforming, during receive the focal point can be changed dynamically in order to follow the propagation of the ultrasonic wave. Therefore, the delay calculation for receive beamforming (τ_i^{rx}) is a function of time and can be calculated as:

$$\tau_i^{rx} = \frac{\sqrt{(x_i - p_{fx}(t))^2 + (y_i - p_{fy}(t))^2 + (z_i - p_{fz}(t))^2} - |p_f(t)|}{c}, \tag{1.4}$$

where (x_i, y_i, z_i) is the spatial position of the i^{th} element in the transducer, p_f is the distance from the focus point to the center of the transducer, c is the sound speed, and t is the time instance being evaluated. The reconstructed image line from a single transmit event is thus the sum of the signals received by all array elements after phase alignment.

Beam profile

The beam profile displays the pressure distribution within the image plane on a logarithmic scale. When observed from a plane perpendicular to the beam axis (i.e., the *lateral beam profile*) at the focal depth, a middle lobe (i.e., *main lobe*) and lobes further out (i.e., *side lobes*) can be distinguished. Similarly, the beam profile could be displayed on a plane along the beam axis (i.e., *range beam profile*). Ideally, to get the best image quality possible, ultrasound beams should have narrow main lobes and low side lobes. Based on the Fraunhofer approximation, the transmit beam width (bwf) at the focal depth can be estimated as [13]:

$$bwf = f_{\#}\lambda, \tag{1.5}$$

where λ is the wavelength of the transmitted wave, and $f_{\#}$ is the *f-number* which is the ratio between the distance from the focal point to the center of the transducer (D_f), and the transducer aperture size (a):

$$f_{\#} = \frac{D_f}{a}. \tag{1.6}$$

In most of ultrasound imaging applications, it is desired to have uniform image resolution with depth, therefore, a constant $f_{\#}$ is typically used on receive by increasing the array aperture following the propagation of the ultrasound pulse (i.e., *expanding aperture*). Also, the range span in which the beam width can be assumed constant (i.e., *focal range*, L_f) can be defined as [13]:

$$L_f = 2f_{\#}^2\lambda. \tag{1.7}$$

The above-described beam profile concepts are illustrated in Fig. 1.6.

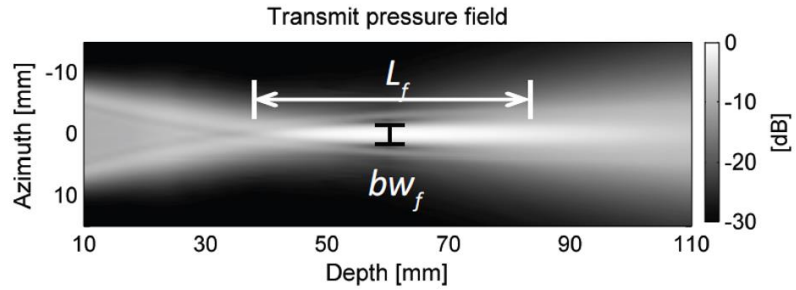

(a)

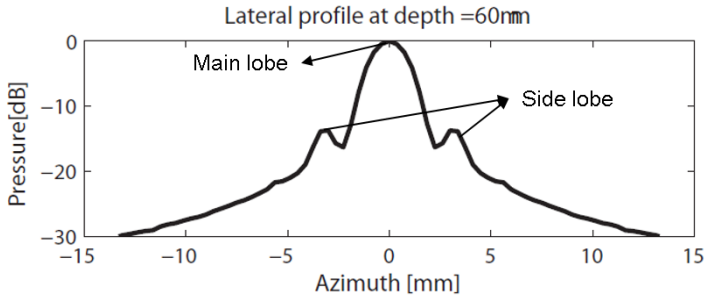

(b)

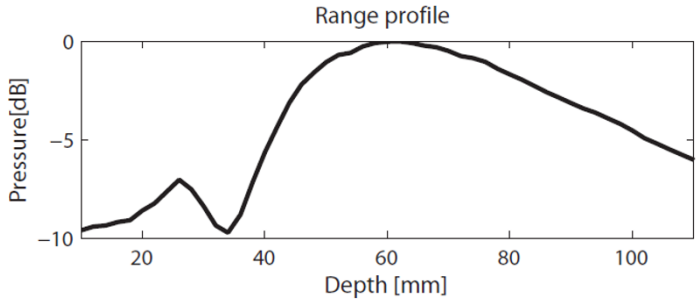

(c)

Fig. 1.6. Beam profile concepts. Modified from [12].

Apodization

In order to reduce the side lobes of the transmit/receive signals, amplitude weighting functions (also called apodization functions) can be implemented. These functions gradually reduce the amplitude at the edges of the transducer aperture to zero in order to suppress side lobes. However, the use of apodization functions implies a reduction of the energy transmitted and comes at the expense of broadening the main lobe. The most common apodization functions used in ultrasound imaging are Hamming, Gaussian, Tukey, and Hanning.

1.2.7 Spatial sampling

Also directly related to the image resolution, is the correct spatial sampling of the FOV (i.e., the line density of the system), to avoid introducing artifacts due to aliasing. Based on the Fraunhofer approximation, the minimum required line density can be defined based on the transmit and two-way beam density, f^{tx} and f^{txrx} respectively, as [13]:

$$f^{tx} = k^{tx}\frac{a^{tx}}{\lambda}, k^{tx} \geq 1, \tag{1.8}$$

$$f^{txrx} = k^{txrx}\frac{(a^{tx}+a^{rx})}{\lambda}, k^{txrx} \geq 1, \tag{1.9}$$

where a^{tx} and a^{rx} are the transmit and receive, respectively, and λ is the wavelength. Meanwhile, k^{tx} and k^{txrx} are the transmit and two-way oversampling rates, respectively. Which are the amount of overlap between the beams to avoid image artifacts due to inter-beam spacing.

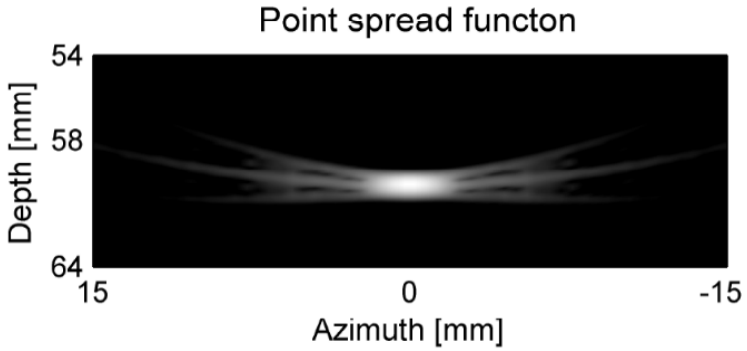

Fig. 1.7. Point spread function of an imaging system, reproduced from [12].

1.2.8 Image quality

The image quality of the system can be evaluated based on two criteria: *spatial resolution* and *image contrast*.

1.2.8.1 Spatial resolution

The spatial resolution is the minimum distance between two targets that the system can distinguish. To evaluate it, the dimension of the point-spread-function (PSF) is typically used, since it describes the response of an imaging system to a point source, as shown in Fig. 1.6. In ultrasound imaging, the resolution can be evaluated as *axial*, *lateral* and *elevation*.

Axial resolution (Δx). Depends on the pulse length (ΔT_{pulse}), and can be approximated by:

$$\Delta x \approx \frac{c \cdot \Delta T_{pulse}}{2} = \frac{c}{2 \cdot \Delta B_{pulse}}, \tag{1.10}$$

where c is the speed of sound and ΔB_{pulse} is the bandwidth of the transmit pulse.

Lateral resolution (Δz). Can be estimated by the beam width of the two-way beam profile at focal depth given by:

$$\Delta z = \frac{\lambda_c \cdot D_f}{a^{tx} + a^{rx}}, \tag{1.11}$$

where λ_c is the central wavelength of the transmit pulse, D_f is the focal depth, $a^{tx}$and a^{rx} are the dimension of the transmit and receive apertures, respectively.

Elevation resolution (Δy). Can be calculated similarly to the lateral resolution but with the corresponding transducer aperture dimensions. In 1D phased array transducers, the beam has a fixed mechanical focus in the elevation direction by the use of an acoustic lens. In contrast, for 2D phased array transducer the focal point can be electrically adjusted.

1.2.8.2 Image contrast

The image contrast is the capability of a system to distinguish between two regions with different scattering properties. It is commonly measured as the contrast-to-noise ratio (CNR) of the system which can be calculated as:

$$CNR = \frac{\mu_{dB\_bck} - \mu_{dB\_cyst}}{\sqrt{\sigma^2_{dB\_bck} + \sigma^2_{dB\_cyst}}}, \quad (1.12)$$

where μ_{dB_bck} and μ_{dB_cyst} are the mean gray levels in the background and cystic regions respectively, and $\sigma^2_{dB\_bck}$ and $\sigma^2_{dB\_cyst}$ are their respective standard deviations.

1.2.9 Frame rate

In US imaging the temporal resolution of a system can be measured as the number of frames that can be acquired per second, i.e., the frame rate of the system. More precisely, the frame rate indicates the capability of the system to capture motion. Therefore, given the dynamic nature of the heart, the temporal resolution of the system plays a critical role in echocardiography.

The frame rate (FR) of the system depends on the time that the acoustic wave takes to travel from the transducer surface to the maximal imaging depth (d_{max}) and back (i.e., time-of-flight), and the number of transmit events (N_{tx}) used to sample the desired FOV. It can be determined as:

$$FR = \frac{c}{2 \cdot N_{tx} d_{max}}, \quad (1.13)$$

where c is the speed of sound. Conventionally, from each transmit beam one image line is reconstructed, in which case N_{tx} corresponds to the number of image lines. Since the sound velocity of the wave is determined by the soft tissues it propagates through, and the maximal imaging depth is defined by the anatomical dimensions of the heart (typically 15cm in adults), the number of transmit events should be reduced in order to increase the FR.

1.3 Volumetric cardiac imaging

Despite of 2D cardiac ultrasound imaging being the modality of choice for routine cardiac diagnosis, it has two main limitations:

1. The provided images are 2D while the anatomy of the heart is 3D. Hence, the practitioner must combine multiple images in his mind to have an idea of the cardiac geometry, which makes it inefficient and person dependent

2. The 2D US image represents a thin plane at some arbitrary angle of the body, which makes it difficult to re-localize the image plane for follow-up studies. In addition, there is the risk that the 2D plane would be located obliquely to the heart which could lead to wrong geometrical estimates (i.e., foreshortening)

Hereto, volumetric (3D) cardiac ultrasound has gained clinical interest in the last decades, as it provides a more intuitive interpretation of the resulting images due to the 3D nature of the heart. Moreover, myocardial motion and deformation are truly three-dimensional, therefore, volumetric echocardiography allows to measure the functioning of the heart without relying on geometrical assumptions.
Typically, to image the whole heart, a 75°x75° volume is required, which would take about ten thousand focused transmits to scan without parallelization at full (2D) line density (~100 emissions in both azimuth and elevation directions). Using a pulse repetition frequency (PRF) of 5kHz, which is common for transthoracic cardiac imaging, and given the above-mentioned scan configuration, the achievable frame rate would thus be about 0.5 Hz. Obviously, this frame rate is too low to visualize a moving heart (beating around 60 times per minute) in real-time.

Two straightforward ways of decreasing transmit events is by limiting the field-of-view (i.e. narrowing the sector) or by reducing line density (i.e. increasing the spacing between adjacent firings), as both result in less transmit events per frame. However, none of these methods is desired as one might leave anatomical structures unscanned and the other would reduce image quality. To overcome this limitation, different methods that have been presented mainly for 2D imaging to increase frame rate, have also been implemented for 3D acquisitions. Current state-of-the-art commercial systems make use of a combination of several of those techniques for fast volumetric imaging, such as:

a) Retrospective ECG gating
In this approach, the pyramidal volume is divided into several small subsectors. Given that each subsector represents a reduced FOV it can be imaged at a high frame rate. Then, the resulting images are combined using retrospective ECG-gating to obtain the full volume [14]. A schematic of this approach is illustrated in Fig. 1.8. However, although this method preserves spatial resolution and field-of-view has been retrospective gating, it prolongs acquisition time and it is not applicable in heart rate variability and patients with atrial fibrillation. Furthermore, stitching artefacts might be introduced due to either probe or patient motion during the acquisition.

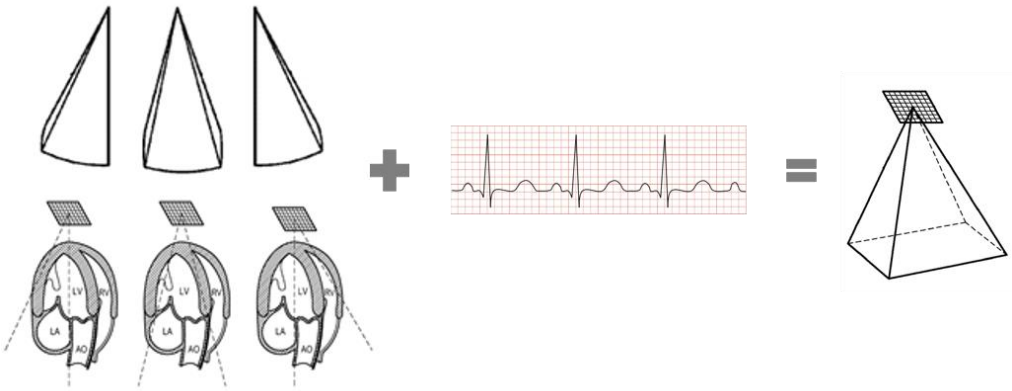

Fig. 1.8. Retrospective ECG-gating illustration. Several subsectors are scanned at high frame rates and then their resulting images are combined using ECG gating to generate the full FOV pyramidal volume. Modified from [15].

b) Multi-line acquisition (MLA)
Parallel receive beamforming is a common method to increase frame rate, and it is implemented on most currently available systems. MLA beamforming is performed by reconstructing multiple neighbouring lines from each transmit beam. To enable this, the transmit beam needs to be broaden in order to insonify a bigger area. The broader the beam the more MLA that can be reconstructed from it. However, a broader beam intrinsically results in reduced lateral resolution, which degrades image quality. Therefore, a compromise between the amount of MLA and the image quality has to be made. Broad beams can be generated by:

1) Transmitting a less-focused beam by reducing the transmit aperture (Fig. 1.9(b)). The smaller the aperture the broader the beam. However, the less energy being transmitted and therefore the poorer SNR and the less penetration.

2) Transmitting an unfocused beam by using the full aperture. This beams can be generated by transmitting with the full aperture at once (i.e., plane wave imaging - Fig. 1.9(c)), or by setting a virtual focal point behind the transducer's aperture (i.e., diverging wave imaging - Fig. 1.9(d)). However, by using broad beams the energy of the acoustic wave is spread over a larger area, significantly affecting

the SNR of the system and making harmonic imaging unpractical. Coherent spatial compounding has been proposed as a solution to increase image quality of such systems. In this technique, the same region is visualized from (slightly) different directions and the final image is the average of all acquisitions. This implies a greater amount of transmit events reducing the effective gain in frame rate.

An example of the different transmit beam widths is shown in Fig. 1.9. The number of MLA that can be reconstructed per MLT beam will be explained and investigated in more detail in chapter 3.

In addition, there is a misalignment of the transmit and receive directions intrinsic to MLA imaging. This misalignment is prone to generate degradation in image due to warping and skewing effects, most often referred to as block-artifacts [15]. In order to mitigate this effect, synthesizing a transmit beam in the direction corresponding to each receive line has been proposed.

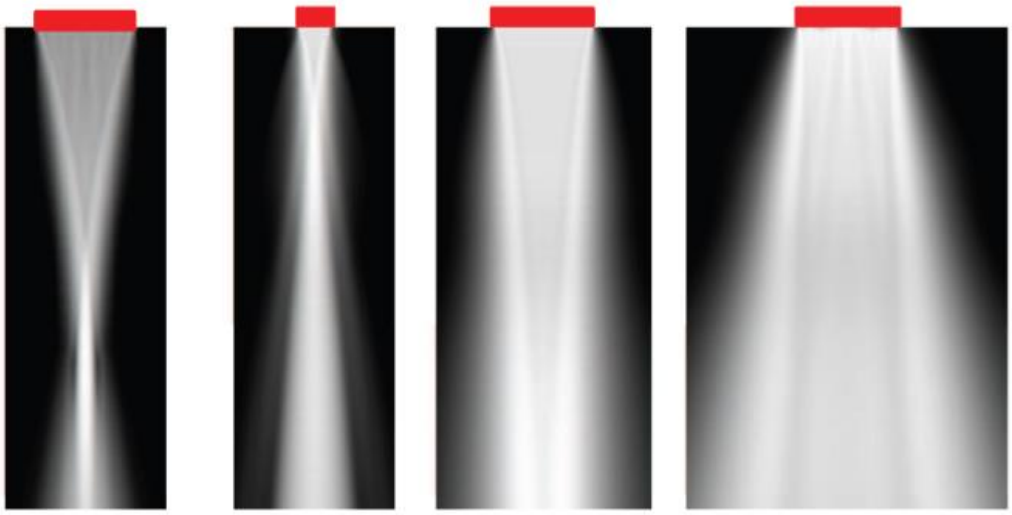

Fig. 1.9. Example of the different transmit beam widths: (a) focused beam; (b) less-focused beam by reducing transmit aperture; (c) plane wave by transmitting an unfocused beam; d) diverging wave by setting a virtual focal point behind the transducer. The red rectangles on top of the images represent the size of the transducer transmit aperture. Reproduced from with permission [12].

c) Diverging wave using sparse virtual array
More recently, Diverging Wave (DW) imaging using a sparse virtual array located behind the probe [16] (Fig. 1.10), has been proposed which allows to scan the volume at very high rates since the line density is only restricted by the reconstruction time. These virtual sources are used for compounding emissions, and can be tailored to adjust resolution, contrast, SNR, frame rate, and the FOV. Allowing the implementation of an optimal imaging sequence for a specific application.

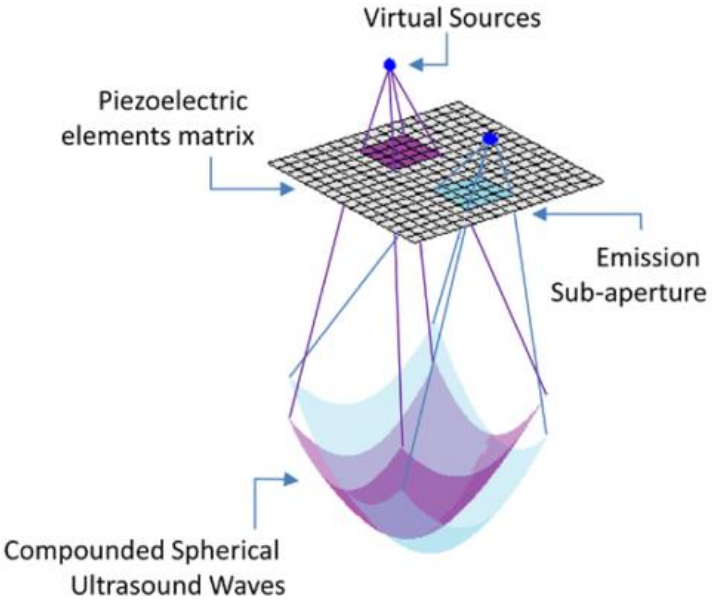

Fig 1.10. 3D ultrafast ultrasound imaging framework. Acquisitions are defined by a virtual array located behind the probe, which is then used to synthetically form an entire imaging volume. When virtual sources are located near the physical probe, the sub-aperture used is smaller and the curvature of the emitted waveform is increased, which results in the insonification of a large field-of-view at the cost of a lower propagated energy. Replicated from [16].

Although, it showed a good performance in several clinical application (such as 3D Shear-Wave Imaging, 3D Ultrafast Doppler Imaging, and, 3D ultrafast combined Tissue and Flow Doppler Imaging), the use of unfocused beams implies that the energy of the beam is spread over a wider area resulting in low pressures, which do not allow for harmonic imaging. Therefore, the overall signal-to-noise ratio drops having a negative impact on motion estimators (as given by the fundamental Cramer-Rao Lower Bound [17]).

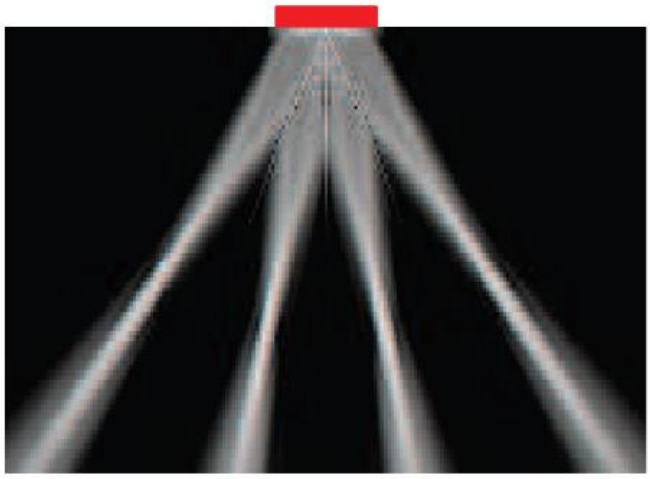

Fig. 1.11. Example of the pressure field of a multi-line transmit system transmitting 4 simultaneous focused beams. The red rectangle represents the transducer aperture. Reproduced from [12] with permission.

d) Multi-line transmit

As an alternative, multi-line transmit beamforming (MLT) has been proposed to increase temporal resolution without significantly compromising the spatial resolution and/or the SNR [18]. This is achieved by simultaneously transmitting multiple focused beams (as

shown in Fig. 1.11.), thereby the frame rate gain is equal to the number of parallel beams and it allows for harmonic imaging [19].

Transmitting into multiple directions simultaneously, requires the application of non-identical electric excitation pulses (EEP) to all elements in the phased array transducer. These pulses are defined as the sum of the EEP that would be applied on the individual elements when emitting the transmit beams separately. As an example, Fig. 1.12 shows the pulses that would be applied to individual elements of a transducer in order to transmit in two directions consecutively (Fig. 1.12(a-b)), and simultaneously (Fig. 1.12(c)). As this sum will result in the superposition of the EEP, to date, MLT implementations were done on systems having arbitrary waveform generators (AWG). However, given that most of the available systems have a tri-state pulser only, we have investigated how MLT sequences can be implemented in such systems. The results of this investigation are presented in Chapter 4.

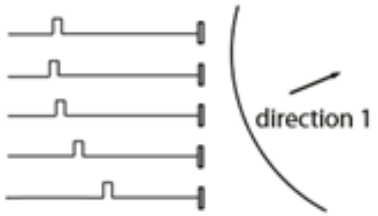

(a) Transmit direction 1

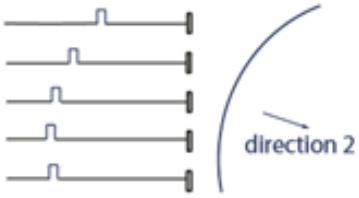

(b) Transmit direction 2

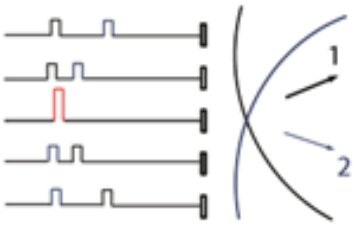

(c) Transmit direction 1 and 2

Fig. 1.12. Pulses to be applied on individual elements of a phased-array transducer to generate two conventional, focused single line: (a) and (b) consecutively, (c) simultaneously.

Cross-talk

Potential artifacts such as cross-talk might be introduced due to the interaction between the MLT beams. There are two types of cross-talk: 1) transmit cross-talk, when the side lobe energy of a beam is picked up by the main lobe of another beam; 2) receive cross-talk, when the main lobe energy of a beam is picked up by the side lobe of another receive beam. The 2 types of cross-talk can be seen when imaging the PSF with a 2MLT system in Fig. 1.13.

However, it has been recently demonstrated in 2D that both types of cross-talk can be significantly suppressed by using proper apodization [20][21]. As an example, a clear reduction in cross-talk can be observed in Fig. 1.14, for a 4MLT system when using transmit and receive Tukey apodization window (alpha = 0.5) when compared to no apodization. Furthermore, the in-vivo acquisition with the same systems are presented in Fig. 1.15, where very limited cross-talk can be observed. Also, transmitting into multiple directions simultaneously implies the acoustic superposition of the MLT beams in the near field, which raises safety concerns. However, it has also recently been demonstrated that by small modifications of the transmit beamforming, the safety parameters can be adjusted to remain within safety regulations [22].

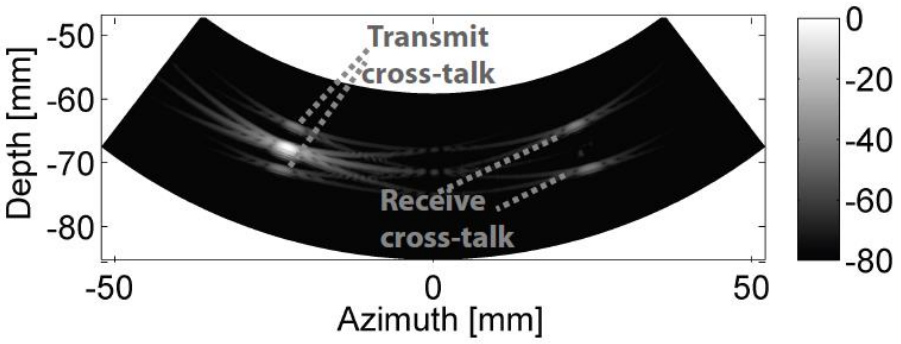

Fig. 1.13. Transmit and receive cross-talks appearing when imaging a point scatterer using a 2 MLT system. Reproduced from with permission [20].

In addition, in order to test the feasibility of MLT for volumetric imaging, a preliminary study was performed where the 2D findings were extrapolated to 3D. It was qualitatively shown that a 16MLT system could generate volumetric images with an acceptable image quality while speeding up the acquisition process by a factor of 16 [23].

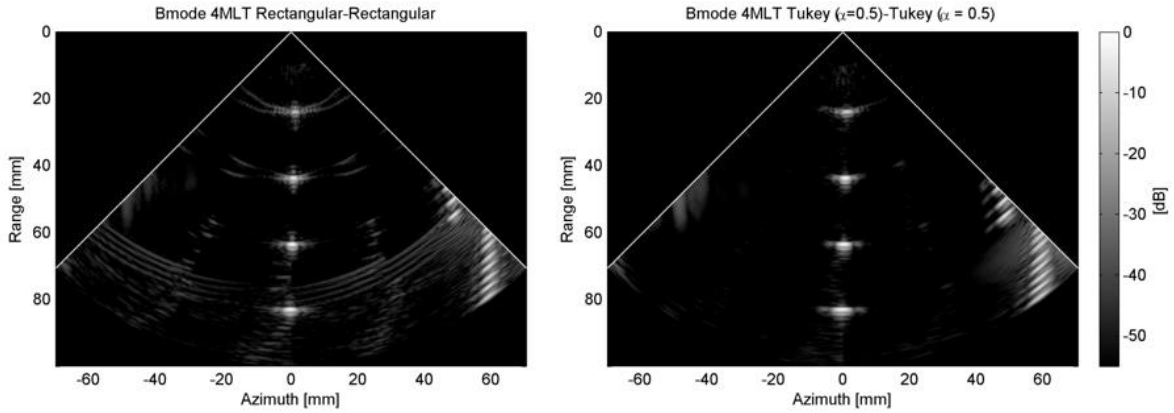

Fig. 1.14. Cross-talk reduction using transmit and receive Tuckey (alpha = 0.5) apodization. Reproduced from with permission [21].

Essentially, MLT preserves image quality [18] but it has a relatively limited speed-up in acquisition time. An alternative to further increase frame rate is to combine MLT scanning sequences with MLA acquisition. In this way, several image lines can be reconstructed per parallel transmit beam, i.e., transmit and receive parallelization. In fact, the transmit beams' width can be easily adapted depending on desired the number of MLA, however, as mentioned before, the broader the beam the more MLA that can be reconstructed but the lower the SNR of the system.

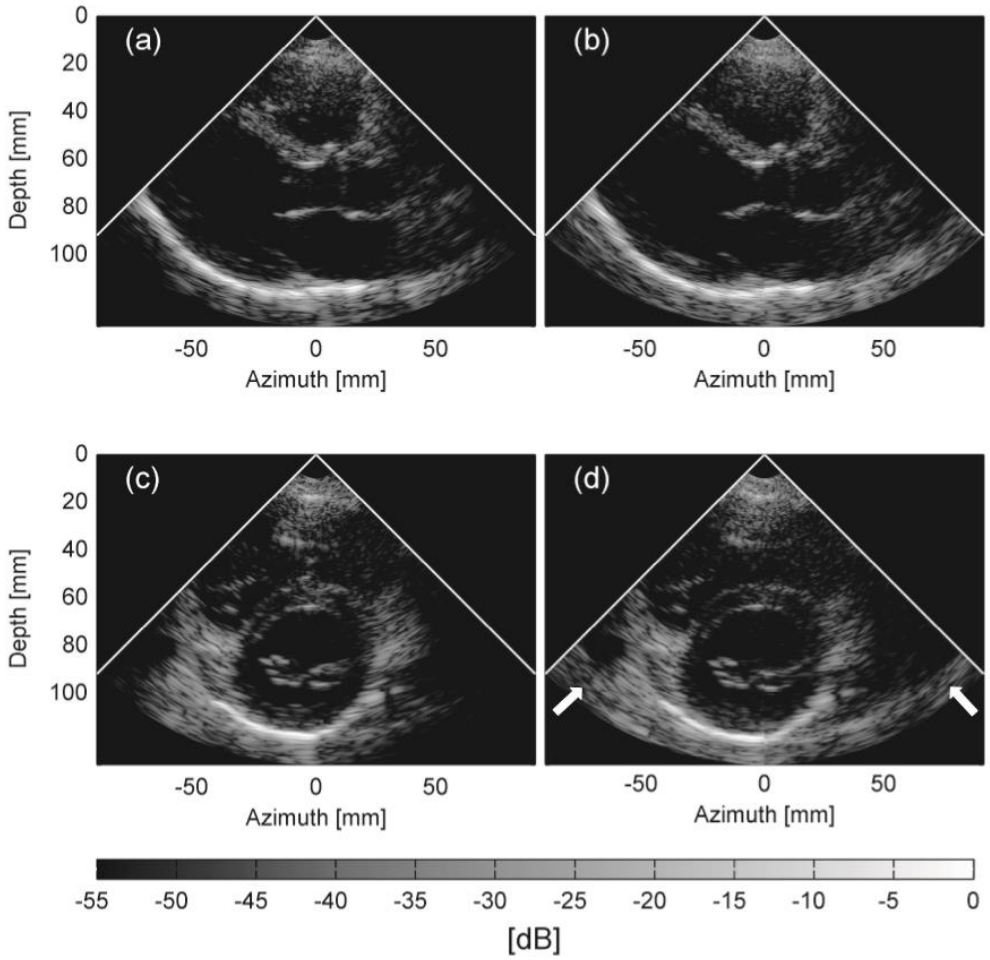

Fig. 15. Sample images acquired from the parasternal long axis view (upper panels) and short axis view (lower panels) using SLT/4MLT imaging setup with Tukey ($\alpha = 0.5$) apodization on transmit and receive. The images on the left were acquired using the SLT interleaved with the 4MLT. Reproduced from [21] with permission.

1.4 Objective and outline of the thesis

The aim of this Ph.D. project was to develop and validate new methods for (ultra)fast 3D functional imaging of the myocardium by investigating a combination of advanced beamforming techniques (i.e. MLT, MLA). The methods were developed and tested by computer simulation with subsequent refinements in an experimental setup.

To achieve this goal, first, a new analytic expression for fast calculation of the impulse response function (essential to simulate accurate ultrasound images) was proposed and is described in chapter 2. As a result, thanks to the improvement in computational time of the home-made ultrasound imaging simulator, new beamforming techniques for fast volumetric echocardiography could be studied. More specifically, a comparison of the performance of different MLT-MLA systems was investigated by computer simulations (chapter 3), and the results were corroborated by *in-vitro* experiments (chapter 4). However, despite the achieved improvements in temporal resolution, the frame rate was still not high enough to resolve all cardiac phases, therefore, a new scanning strategy was proposed which combines the limitation of the FOV to the anatomical relevant space only, and the use of parallelized scanning sequences. This approach is defined in chapter 5. Finally, in chapter 6, the most important conclusions of this work are summarized and some speculations are made for the future perspectives of this work.

2 A new analytic expression for fast calculation of the transient near and far field of a rectangular baffled piston

This work was published in: A. Ortega, L. Tong, and J. D'hooge, "A new analytic expression for fast calculation of the transient near and far field of a rectangular baffled piston.," *Ultrasonics*, vol. 54, no. 4, pp. 1071–7, Apr. 2014.

Abstract
Essential to (cardiac) 3D ultrasound are 2D matrix array transducer technology and the associated (two-stage) beamforming. Given the large number of degrees of freedom and the complexity of this problem, simulation tools play an important role. Hereto, the impulse response (IR) method is commonly used. Unfortunately, given the large element count of 2D array transducers, simulation times become significant jeopardizing the efficacy of the design process. The aim of this study was therefore to derive a new analytical expression to more efficiently calculate the IR in order to speed up the calculation process. To compare accuracy and computation time, the reference and the proposed method were implemented in MATLAB and contrasted. For all points of observation tested, the IR with both methods was identical. The mean calculation time however reduced in average by a factor of 3.93±0.03 times. The proposed IR method therefore speeds up the calculation time of the IR of an individual transducer element while remaining perfectly accurate. This new expression will be particularly relevant for 2D matrix transducer design where computation times remain currently a bottle neck in the design process.

2.1 Introduction

Essential to volumetric ultrasound are 2D phased array transducers that allow to steer and focus the ultrasound beam in both azimuth and elevation directions in both transmit and receive [24]. Moreover, in order to keep temporal resolution of the data sets acceptable while preserving image quality, parallel receive beamforming [25] as well as post-processing of the resulting images is required. As a fully sampled matrix array transducer has about 4000 independent elements while the front-end of the ultrasound system only has 256 channels, beamforming is typically done in two phases where part of the beamforming is done in the transducer itself while the pre-beam formed signals are combined in the front-end in order to generate the individual image lines (i.e., two-stage beamforming [26]). As a result, modern 3D ultrasound systems have a lot of degrees of freedom in the design process. Simulation tools thus play a critical role in the optimization and development of such systems.

The spatial impulse response function (IR), originally described by Tupholme and Stepanishen [27], [28], is a popular approach to simulate linear ultrasound fields and pulse-echo signals [29]. Assuming an isotropic, homogeneous and non-dissipative medium, the transient pressure field $p(\boldsymbol{r},t)$ of a planar transducer in an infinite rigid baffle at a point of observation r, can be written as the convolution of the first time derivative of the normal velocity of the transducer surface $v(t)$, with an IR function $h(r,t)$, which depends on the spatial position relative to the geometry of the piston:

$$p(\boldsymbol{r},t) = \rho \frac{\partial v(t)}{\partial t} * h(\boldsymbol{r},t), \tag{2.1}$$

where ρ is the density of the medium, and $h(r,t)$, is defined as

$$h(\boldsymbol{r},t) = \int_S \frac{\delta\left(t-\frac{R}{c}\right)}{2\pi R} dS, \tag{2.2}$$

here δ is the Kronecker delta function, S denotes the active area of the radiator, R is the distance from dS to the field point r, and c is the velocity of sound in the medium. This integral is essentially the quantitative formulation of the Huygens' principle in which the transducer surface can be seen as a collection of point sources. In this way, only the points on the transducer surface lying at a proper distance from the observation point at a given time point will contribute to the response. Therefore, the calculation of the integral in (2.2) can be reduced to solving a geometrical problem where the intersection of the transducer aperture with a growing sphere has to be found, Fig. 2.1. As such, analytical expressions can be derived for several transducer geometries [28], [30]–[32], for

several transducer velocity profiles [33], [34], for curved transducers [35] [36], and for rectangular double curved transducers[37] .

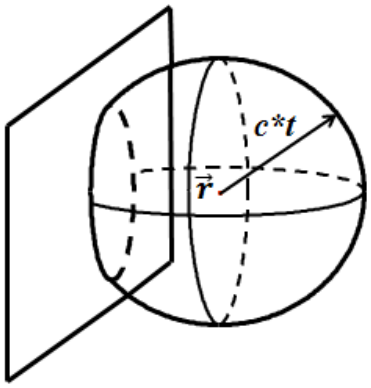

Fig. 2.1. Intersection of the transducer surface with a growing sphere with radius *c*t* (where c is the speed of sound in the medium and t is the time, '*' indicates multiplication), centered at the point of observation ($\vec{r}$)

The IR function can become very peaked (i.e. containing discontinuities) in particular in the far field of the transducer. As a result, in order to evaluate the IR function numerically, high sampling frequencies are required increasing calculation time and making data handling more cumbersome. However, as transducers used in medical ultrasound are band limited, the high frequency components of the IR function are irrelevant. This has formed the basis for approaches to avoid the use of high sampling frequencies proposed in [38] and [39]. Indeed, D'hooge et al. proposed a method to analytically smooth the IR function with a rectangular pulse (i.e. analytically low-pass filter the IR function). This implies that geometrically the area of intersection of a solid sphere centered at the point of observation and the transducer has to be found. On the other hand, Jensen and Svendsen suggested a far-field approximation in which the IR is assumed to be trapezoidal and only the times-of-flight from the transducer corners to the field point have to be calculated.

However, despite these solutions towards limiting calculation times, speed remains an issue when simulating 2D arrays. The underlying reason for this is not only the mere element count but also the relatively inefficient analytical expression of the IR of an individual (rectangular) element itself. This is particularly true when the projection of the point of observation in the transducer plane lies outside the transducer aperture.

Indeed, the solution for a rectangular transducer element is based on the superposition principle and was originally proposed by [30]. The classical formulation of the IR of a rectangular transducer (element) assumes that the point of observation is located exactly above the corner of the rectangular aperture (illustrated in Fig. 2.2(a)). In case of an arbitrary point of observation, a construction of four synthetic rectangles is made – as shown in Fig. 2.2(b) – such that the projection of the point of observation on the transducer plane lies at the corner of each of these four rectangles. In this way, the solution of each of the synthetic rectangles can be calculated and an effective IR is defined by superposition of these individual contributions.

However, if the point of observation falls outside the original aperture, the construction of four synthetic rectangles implies that the original aperture is enlarged and that some contributions that are accounted for originally subsequently need to be subtracted. When the projection of the point of observation in the transducer plane is relatively far from the active aperture area, the enlargement becomes very significant and substantial time is spent on calculating the contribution of rectangles that ultimately will be subtracted again afterwards, as shown in Fig. 2.3.

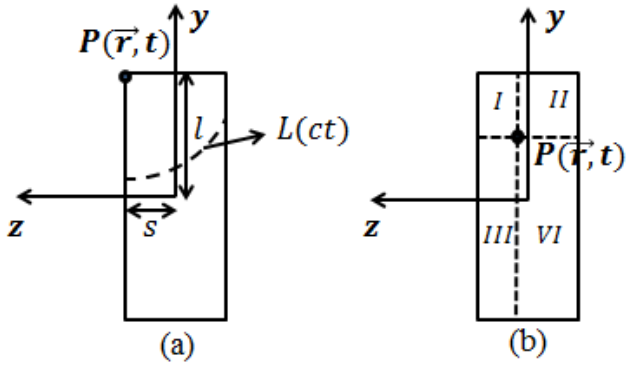

Fig. 2.2. General geometry of the projection of a point observation in front of a rectangular transducer, (a) when it lies on the corner of the transducer, and (b) when it is an arbitrary point and the four synthetic rectangles are made.

In the worst case (Fig. 2.3-(c)), two of the synthetic rectangles (which do not contain the transducer area) overlap implying that a third rectangle (with a size equal to the area of overlap) needs to be calculated to be added since the overlapped area was subtracted twice. This implies that the contribution of this area is effectively estimated three times, when at the end none of it is actually used to express the IR of the transducer surface. Obviously, this implies that redundant calculations are being made. This situation is particularly true when simulating 2D matrix arrays, as due to the small size of the single elements the point of observation is most likely to be in this latter situation.
Hereto, San Emeterio and Ullate [40] proposed a closed-form expression for the IR of a rectangular transducer avoiding inefficient calculations while keeping the accuracy in the responses. The proposed method directly calculates the solution based on the angles of intersection between the rectangular aperture and the growing sphere centered at the point of observation rather than using the superposition principle described above. The expressions proposed by these authors depend on the relative position of the mentioned point to the transducer surface.

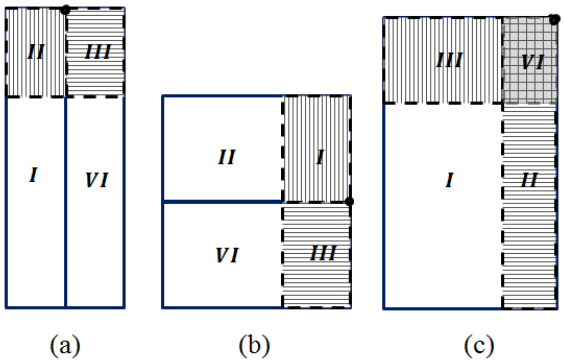

Fig. 2.3. Superposition method. Four synthetic rectangles required when the projection of the point of observation lies outside the transducer surface, (a) on top the aperture, (b) next to the aperture, and (c) in the fourth quadrant. The filled areas are the rectangles that are subtracted.

However, although this method improves the calculation time of the IR for a single element, it does not solve the numerical difficulties related to the discontinuities in the response and high sampling frequencies are therefore still required. Therefore, in this manuscript, an analytical expression is proposed which combines the more efficient calculation of the IR, described by [40], with the analytical low pass filter, described by [38].

2.2 Theory

Following the same principles and making the same assumptions as in [38] , $h(r,t)$ can be low pass filtered without losing accuracy and can be expressed as:

$$L^*(ct) \approx \frac{O\left(c\left(t+\frac{\Delta t}{2}\right)\right) - O\left(c\left(t-\frac{\Delta t}{2}\right)\right)}{\frac{c\Delta t}{sin\theta(ct)}}, \tag{2.3}$$

where $L^*(ct)$is the smoothed arc-length of the IR and *O(ct)* is the area of intersection of a solid sphere, of radius ct, with the transducer aperture, this intersection defines a cone with $\theta(ct)$ half top its angle; Δt is the width of the rectangular pulse with which the IR is smoothed. Then, as in [40], the area of intersection between the solid sphere and the transducer surface can be calculated based on the angle of intersection and the geometry of the intersected area.

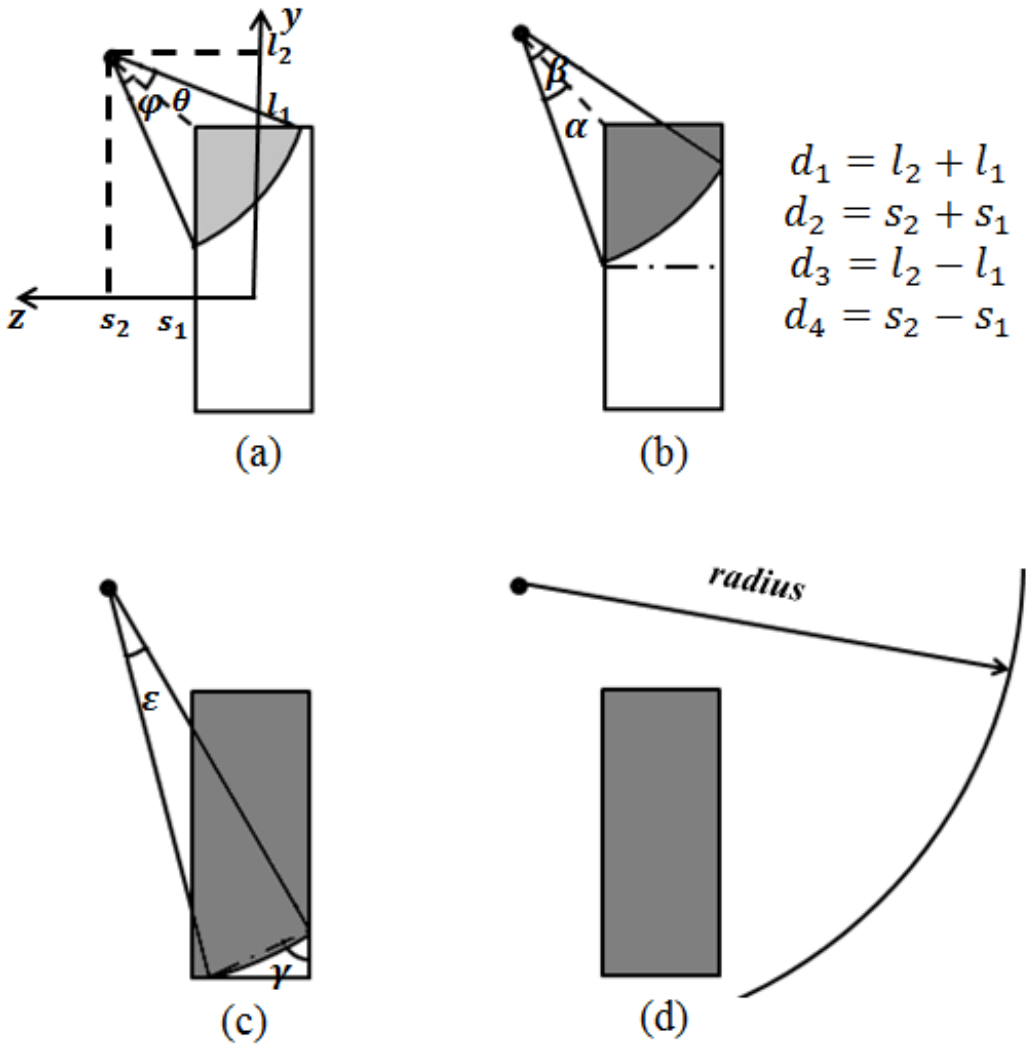

Fig. 2.4. Graphical description of the areas described in equation 3, in which the area of intersection of a circle (with radius $\sqrt{c^2t^2 - x^2}$) and a rectangle is found in four stages, (a) it is a triangular area where one of the sides of the triangle is the arc of the circle, (b) it is the area of a synthetic rectangle where one of the corners is the arc of the circle, (c) it is the area of the rectangle with sides l_1 and s_1, with the farthest corner (from the center of the circle) as the arc of the circle, and *d*) it is the area of the entire rectangle.

Using the notations introduced in Fig. 2.4, the proposed method defines the area of intersection of the solid sphere (with radius $\sqrt{c^2t^2-x^2}$) and the rectangular transducer surface (with $l_1 \geq s_1$), in four stages (for $l_2 \geq l_1$ and $s_2 \geq s_1$): 1) it is the circular sector minus two leftovers triangles (Fig. 2.4(a)); 2) it is the area of a synthetic rectangle, minus a triangle, plus a circular segment (Fig. 2.4(b)); 3) the same as the previous, but the area of the rectangle is the full transducer aperture (Fig. 2.4(c)); and 2.4) it is the area of the entire transducer (Fig. 2.4(d)). Mathematically, this is expressed as (using the notations as in Fig. 2.5):

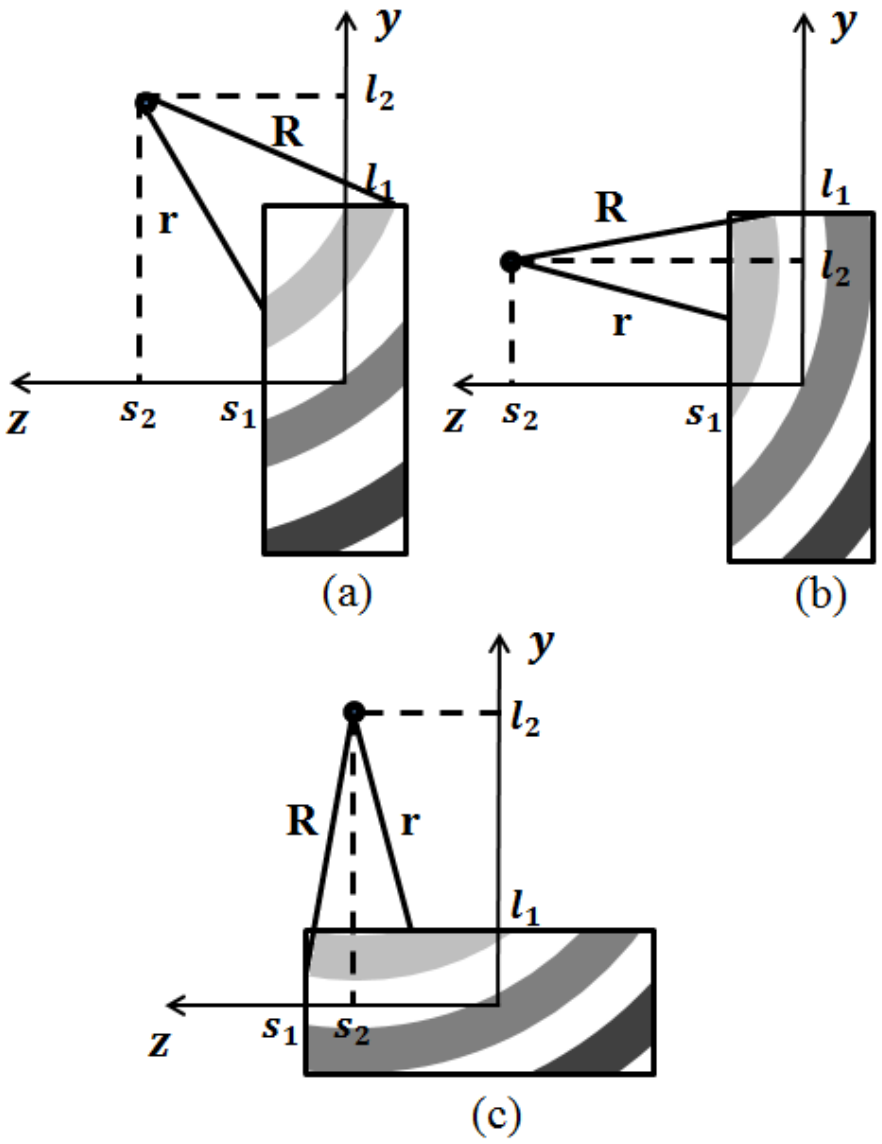

Fig. 2.5. Geometry for a field point in the far field of the rectangular aperture, used to find the area of intersection of the solid sphere with the transducer surface. Where $R = c(t+ \Delta t/2)$ is the external radius of the solid sphere and $r = c(t- \Delta t/2)$ is the internal. The three areas represent three different moments of the intersection. (a) $l_2 \geq l_1$ and $s_2 \geq s_1$, (b) $l_2 \leq l_1$ and $s_2 \geq s_1$, (c) $l_2 \geq l_1$ and $s_2 \leq s_1$

In case $l_2 \geq l_1$ and $s_2 \geq s_1$:

$$O(ct) = (c^2t^2 - x^2) \times \left\{ \begin{array}{c} \left[H_{ct}\left(\sqrt{x^2 + {d_3}^2 + {d_4}^2}\right) - H_{ct}\left(\sqrt{x^2 + {d_3}^2 + {d_2}^2}\right)\right] \\ \times \left[\begin{array}{c} \left(\frac{\theta+\varphi}{2}\right) radius^2 - \\ \left(\frac{1}{2}\right) radius\left(\sqrt{d_3^2 + d_4^2}\right)(sin\theta + sin\varphi) \end{array}\right] + \\ \left[H_{ct}\left(\sqrt{x^2 + {d_3}^2 + {d_2}^2}\right) - H_{ct}\left(\sqrt{x^2 + {d_1}^2 + {d_4}^2}\right)\right] \\ \times \left[\begin{array}{c} base \times height - \frac{\left(\sqrt{\left(2\sin\left(\frac{\beta}{2}\right) radius\right)^2 - height^2}\right) height}{2} + \\ \frac{1}{2}(\beta - sin\beta) radius^2 \end{array}\right] + \\ \left[H_{ct}\left(\sqrt{x^2 + {d_1}^2 + {d_4}^2}\right) - H_{ct}\left(\sqrt{x^2 + {d_1}^2 + {d_2}^2}\right)\right] \times \\ \left[(2l_1)(2s_1) - \frac{\sin(\gamma)\cos(\gamma) hypotenuse}{2} + \frac{1}{2}(\varepsilon - sin\varepsilon) radius^2\right] \\ + H_{ct}\left(\sqrt{x^2 + d_1^2 + d_2^2}\right) \times \left(\frac{4 l_1 s_1}{c^2 t^2 - x^2}\right) \end{array} \right\}, \quad (2.4)$$

where,

$$d_1 = l_1 + l_2 \quad (2.5)$$

$$d_2 = s_2 + s_1 \quad (2.6)$$

$$d_3 = l_2 - l_1 \quad (2.7)$$

$$d_4 = s_2 + s_1 \quad (2.8)$$

$$\theta = \text{acos}\left(\frac{d_4}{\sqrt{d_3 + d_4}}\right) + \text{acos}\left(\frac{d_3}{radius}\right) - \frac{\pi}{2}, \quad (2.9)$$

$$\varphi = \text{acos}\left(\frac{d_3}{\sqrt{d_3 + d_4}}\right) + \text{acos}\left(\frac{d_4}{radius}\right) - \frac{\pi}{2}, \quad (2.10)$$

$$\alpha = \begin{cases} acos\left(\frac{d_3}{\sqrt{d_3 + d_4}}\right) + acos\left(\frac{d_4}{radius}\right) - \frac{\pi}{2}, & \sqrt{x^2 + d_3^2 + d_2^2} \leq \sqrt{x^2 + d_1^2 + d_4^2} \\ acos\left(\frac{d_3}{radius}\right) + acos\left(\frac{d_4}{\sqrt{d_3 + d_4}}\right) - \frac{\pi}{2}, & \sqrt{x^2 + d_3^2 + d_2^2} \geq \sqrt{x^2 + d_1^2 + d_4^2} \end{cases}, \quad (2.11)$$

$$\beta = \begin{cases} \text{asin}\left(\frac{\text{d}_2}{\text{radius}}\right) + \text{acos}\left(\frac{\text{d}_4}{\text{radius}}\right) - \frac{\pi}{2}, & \sqrt{x^2 + d_3^2 + d_2^2} \leq \sqrt{x^2 + d_1^2 + d_4^2} \\ \text{asin}\left(\frac{d_1}{radius}\right) + \text{acos}\left(\frac{d_3}{radius}\right) - \frac{\pi}{2}, & \sqrt{x^2 + d_3^2 + d_2^2} \geq \sqrt{x^2 + d_1^2 + d_4^2} \end{cases}, \quad (2.12)$$

$$\varepsilon = \text{asin}\left(\frac{d_1}{radius}\right) + \text{asin}\left(\frac{d_2}{radius}\right) - \frac{\pi}{2}, \quad (2.13)$$

$$\gamma = \text{acos}\left(\frac{d_2}{radius}\right) + \frac{\varepsilon}{2}, \quad (2.14)$$

$$base = \sqrt{(d_3 + d_4) + radius^2 - 2\left(\sqrt{d_3 + d_4}\right) radius + \cos(\alpha)}, \quad (2.15)$$

$$height = 2 \times \min(l_1, s_1), \quad (2.16)$$

$$H_{ct}(m) = \begin{cases} 1, & ct \geq m \\ 0, & ct < m \end{cases}. \quad (2.17)$$

In case $l_2 \leq l_1$ and $s_2 \geq s_1$:

$$O(ct) = (c^2t^2 - x^2)\times$$
$$\left\{ \begin{array}{c} \left[H_{ct}\left(\sqrt{x^2 + {d_4}^2}\right) - H_{ct}\left(\sqrt{x^2 + {d_3}^2 + {d_4}^2}\right)\right] \\ \times\left[\frac{1}{2}(\theta - \sin(\theta))radius^2\right] \\ +\left[H_{ct}\left(\sqrt{x^2 + {d_3}^2 + {d_4}^2}\right) - H_{ct}\left(\sqrt{x^2 + {d_2}^2}\right)\right] \\ \times\left[\left(\frac{\frac{\theta}{2}+\alpha}{2}\right)radius^2 - \frac{\left(\left(\sqrt{radius^2 - {d^2}_4}+\tan(\alpha)d_4\right)d_4\right)}{2} + \frac{\left(\left(\sqrt{radius^2 - d_3^2}-\mathrm{d}_4\right)^2\tan(\alpha)\right)}{2}\right] \\ +\left[H_{ct}\left(\sqrt{x^2 + {d_2}^2}\right) - H_{ct}\left(\sqrt{x^2 + {d_1}^2 + {d_4}^2}\right)\right] \\ \times\left[\frac{\left(\sqrt{radius^2 - d_3^2}-d_4\right)^2\tan(\alpha)}{2} + \frac{\beta}{2}radius^2 - \frac{1}{2}\left(\frac{\theta}{2} - \sin\left(\frac{\theta}{2}\right)\right)radius^2 - \right. \\ \left. \frac{\left(d_3 - \left(\sqrt{radius^2 - d_3^2}-d_4\right)\tan(\alpha)+\left(\sqrt{radius^2 - d_4^2}\right)d_4\right)}{2}\right] \\ +\left[H_{ct}\left(\sqrt{x^2 + {d_1}^2 + {d_4}^2}\right) - H_{ct}\left(\sqrt{x^2 + {d_3}^2 + {d_2}^2}\right)\right] \\ \times[\left(\frac{\mu}{2}\right)radius^2 + \frac{\left(\sqrt{radius^2 - d_1^2}\right)d_1}{2} + \frac{\left(\sqrt{radius^2 - d_3^2}\right)d_3}{2} - \\ (2d_4l_1) - \frac{1}{2}(\varepsilon - \sin(\varepsilon))radius^2] \\ +\left[H_{ct}\left(\sqrt{x^2 + {d_3}^2 + {d_2}^2}\right) - H_{ct}\left(\sqrt{x^2 + {d_1}^2 + {d_2}^2}\right)\right] \\ \times\left[4s_1l_1 - \frac{\sin(\gamma)\cos(\gamma)\left(2\sin\left(\frac{\varphi}{2}\right)radius\right)^2}{2} + \frac{1}{2}(\varphi - \sin(\varphi))radius^2\right] \\ +H_{ct}\left(\sqrt{x^2 + {d_1}^2 + {d_2}^2}\right)\times\left(\frac{4s_1l_1}{c^2t^2 - x^2}\right) \end{array} \right\}, \quad (2.18)$$

where,

$$\theta = 2\,\mathrm{acos}\left(\frac{d_4}{\sqrt{c^2t^2 - x^2}}\right), \quad (2.19)$$

$$\alpha = \mathrm{asin}\left(\frac{d_3}{\sqrt{c^2t^2 - x^2}}\right), \quad (2.20)$$

$$\beta = \mathrm{asin}\left(\frac{d_3}{\sqrt{c^2t^2 - x^2}}\right) + \mathrm{acos}\left(\frac{d_4}{\sqrt{c^2t^2 - x^2}}\right), \quad (2.21)$$

$$\mu = \mathrm{asin}\left(\frac{d_1}{\sqrt{c^2t^2 - x^2}}\right) + \mathrm{asin}\left(\frac{d_3}{\sqrt{c^2t^2 - x^2}}\right), \quad (2.22)$$

$$\varepsilon = 2\,\mathrm{acos}\left(\frac{d_2}{\sqrt{c^2t^2 - x^2}}\right), \quad (2.23)$$

$$\varphi = \mathrm{asin}\left(\frac{d_2}{\sqrt{c^2t^2 - x^2}}\right) + \mathrm{asin}\left(\frac{d_1}{\sqrt{c^2t^2 - x^2}}\right) - \frac{\pi}{2}, \quad (2.24)$$

$$\gamma = \mathrm{acos}\left(\frac{d_2}{\sqrt{c^2t^2 - x^2}}\right) + \frac{\varepsilon}{2}. \quad (2.25)$$

In case $l_2 \geq l_1$ and $s_2 \leq s_1$:

$$O(ct) = (c^2t^2 - x^2)\times$$

$$\left\{ \begin{array}{c} \left[H_{ct}\left(\sqrt{x^2 + {d_3}^2}\right) - H_{ct}\left(\sqrt{x^2 + {d_3}^2 + {d_4}^2}\right)\right] \\ \times\left[\frac{1}{2}(\theta - \sin(\theta))radius^2\right] \\ + \left[H_{ct}\left(\sqrt{x^2 + {d_3}^2 + {d_4}^2}\right) - H_{ct}\left(\sqrt{x^2 + {d_1}^2}\right)\right] \\ \times\left[\left(\frac{\frac{\theta}{2}+\alpha}{2}\right)radius^2 - \frac{\left(\left(\sqrt{radius^2 - d_3^2} + \tan(\alpha)d_3\right)d_3\right)}{2} + \frac{\left(\left(\sqrt{radius^2 - d_4^2} - d_3\right)^2\tan(\alpha)\right)}{2}\right] \\ + \left[H_{ct}\left(\sqrt{x^2 + {d_1}^2}\right) - H_{ct}\left(\sqrt{x^2 + {d_3}^2 + {d_2}^2}\right)\right] \\ \times\left[\begin{array}{c}\frac{\left(\sqrt{radius^2 - d_4^2} - d_3\right)^2\tan(\alpha)}{2} + \frac{\beta}{2}radius^2 - \frac{1}{2}\left(\frac{\theta}{2} - \sin\left(\frac{\theta}{2}\right)\right)radius^2 - \\ \frac{\left(d_4 - \left(\sqrt{radius^2 - d_4^2} - d_3\right)\tan(\alpha) + \left(\sqrt{radius^2 - d_3^2}\right)d_3\right)}{2}\end{array}\right] \\ + \left[H_{ct}\left(\sqrt{x^2 + {d_3}^2 + d_2^2}\right) - H_{ct}\left(\sqrt{x^2 + {d_1}^2 + {d_4}^2}\right)\right] \\ \times\left[\begin{array}{c}\left(\frac{\mu}{2}\right)radius^2 + \frac{\left(\sqrt{radius^2 - d_2^2}\right)d_2}{2} + \frac{\left(\sqrt{radius^2 - d_4^2}\right)d_4}{2} - (2d_3s_1) - \\ \frac{1}{2}(\varepsilon - \sin(\varepsilon))radius^2\end{array}\right] \\ + \left[H_{ct}\left(\sqrt{x^2 + {d_1}^2 + {d_4}^2}\right) - H_{ct}\left(\sqrt{x^2 + {d_1}^2 + {d_2}^2}\right)\right] \\ \times\left[4s_1l_1 - \frac{\sin(\gamma)\cos(\gamma)\left(2\sin\left(\frac{\varphi}{2}\right)radius\right)^2}{2} + \frac{1}{2}(\varphi - \sin(\varphi))radius^2\right] \\ + H_{ct}\left(\sqrt{x^2 + {d_1}^2 + {d_2}^2}\right)\times\left(\frac{4s_1l_1}{c^2t^2 - x^2}\right) \end{array} \right\}, \quad (2.26)$$

where,

$$\theta = 2\,\mathrm{acos}\left(\frac{d_3}{\sqrt{c^2t^2 - x^2}}\right), \quad (2.27)$$

$$\alpha = \mathrm{asin}\left(\frac{d_4}{\sqrt{c^2t^2 - x^2}}\right), \quad (2.28)$$

$$\beta = \mathrm{asin}\left(\frac{d_4}{\sqrt{c^2t^2 - x^2}}\right) + \mathrm{acos}\left(\frac{d_3}{\sqrt{c^2t^2 - x^2}}\right), \quad (2.29)$$

$$\mu = \mathrm{asin}\left(\frac{d_2}{\sqrt{c^2t^2 - x^2}}\right) + \mathrm{asin}\left(\frac{d_4}{\sqrt{c^2t^2 - x^2}}\right), \quad (2.30)$$

$$\varepsilon = 2\,\mathrm{acos}\left(\frac{d_1}{\sqrt{c^2t^2 - x^2}}\right), \quad (2.31)$$

$$\varphi = \mathrm{asin}\left(\frac{d_1}{\sqrt{c^2t^2 - x^2}}\right) + \mathrm{asin}\left(\frac{d_2}{\sqrt{c^2t^2 - x^2}}\right) - \frac{\pi}{2}, \quad (2.32)$$

$$\gamma = \mathrm{acos}\left(\frac{d_1}{\sqrt{c^2t^2 - x^2}}\right) + \frac{\varepsilon}{2}. \quad (2.33)$$

Note: the position dependent equations in case $l_2 \geq l_1$ and $s_2 \leq s_1$, and in case $l_2 \leq l_1$ and $s_2 \geq s_1$ have been omitted for the sake of brevity but these expressions are very analogous and can easily be derived. In case $l_2 \leq l_1$ and $s_2 \leq s_1$, the original expressions proposed in D'hooge et al. using the superposition principle, do not contain redundant calculations and were therefore re-used to complete the calculations of the IR.

Remark that the same constraint on how much the IR function can be smoothed while keeping accuracy, as detailed in [38], has to be taken into account, where the maximal amount of smoothing is limited by the highest-frequency component of the excitation pulse as:

$$f_{Emax} < \frac{1}{\Delta t}. \tag{2.34}$$

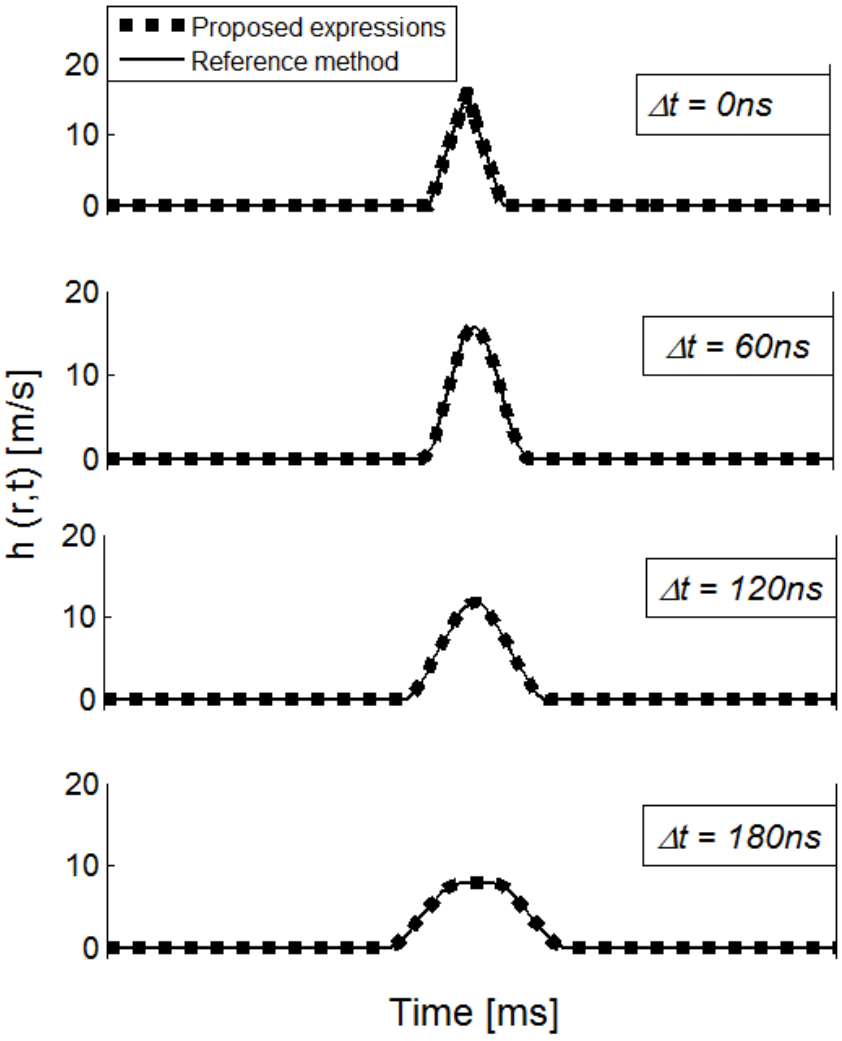

Fig. 2.6. The impulse response function of a rectangular transducer with $l_1 = s_1$, smoothed with rectangular pulses of different width Δt, f_S =100MHz. x/ s_1 = 20, y/ l_1 = 30, and z/ s_1 = 30.

2.3 Simulations

In order to compare accuracy and speed, the smoothed expressions presented by D'hooge et al. (reference method) and the proposed equations were implemented in MATLAB R2010b (MathWorks Inc., Natick, MA). The IR function, of a rectangular single element transducer

(9.28x9.28mm^2) at a depth of 10cm, was calculated 1) smoothed with rectangular pulses of different widths (Δt) sampled at 100MHz at a single spatial position (y/l1 = 30, and z/s1 = 30), and 2) at different spatial positions smoothed with a rectangular pulse of 120ns (Δt) and sampled at 50MHz.

Also, for the same parameters used in simulation 2), the IR function was calculated 1000 times at different spatial positions along the diagonal of the rectangular single element transducer. The resulting IRs were compared and the time required for their calculation was recorded.

2.4 Results

Figure 2.6 shows the IR function smoothed with rectangular pulses of different widths while Fig. 2.7 illustrates the IR function for a rectangular transducer smoothed with rectangular pulse of 120ns width (Δt) at different spatial positions. Both figures show a perfect match between the IR's calculated with either method at all smoothing levels and spatial locations.

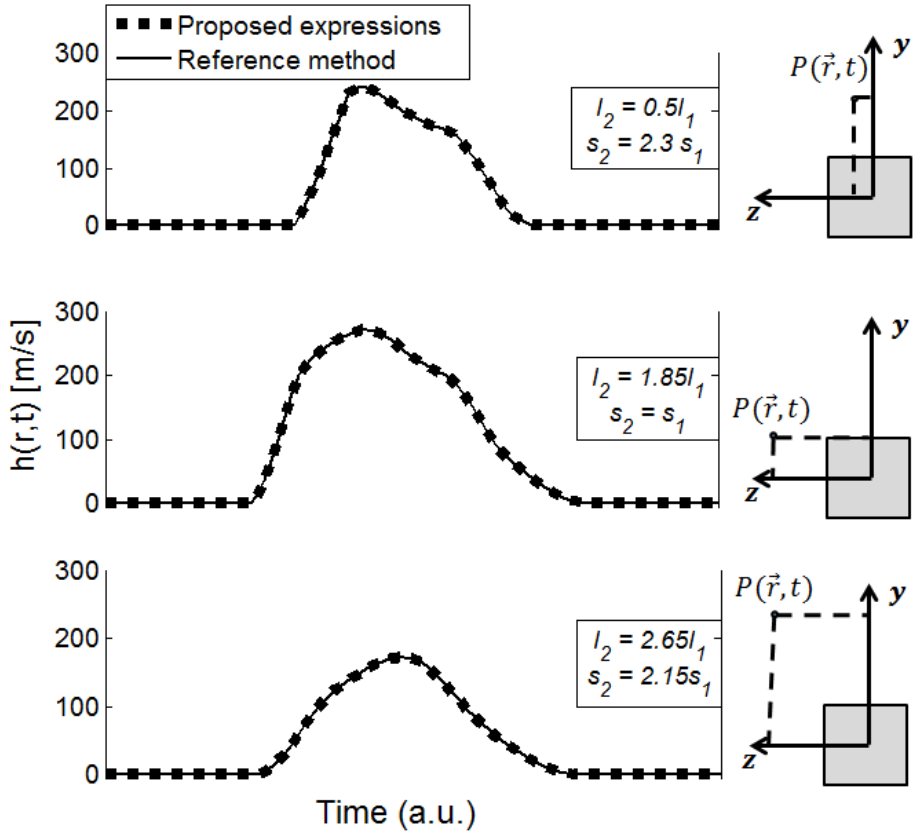

Fig. 2.7. The impulse response function of rectangular transducer with s_1/l_1=1, at different spatial positions with the reference method (dashed) and the proposed expressions (solid).

The average CPU time for calculation of the IR of a single element transducer and at different points of observation moving away along its diagonal is presented in Fig. 2.8. The mean calculation time reduced from an average of 2.32s per spatial position for the classical expression to 0.59s for the proposed expression resulting in a total speed up of 3.93±0.03 times.

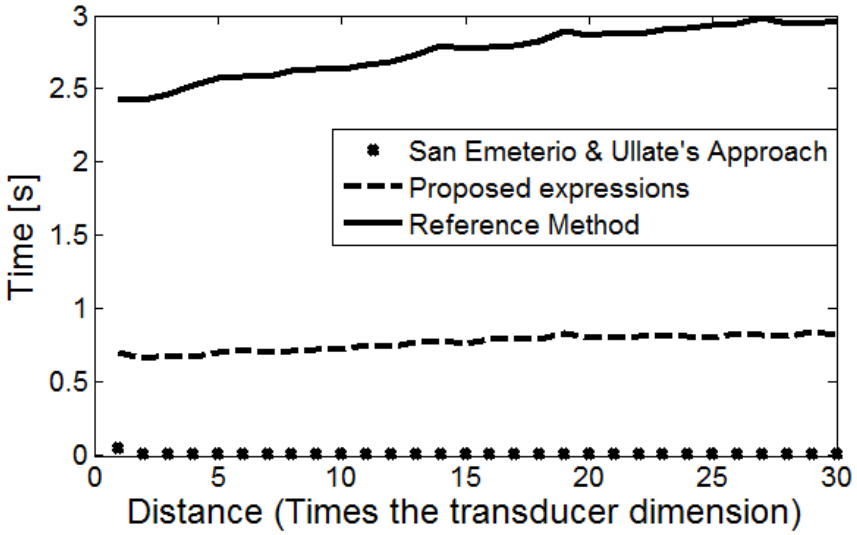

Fig. 2.8. Average time per spatial position of the point of observation (moving away from the transducer in its diagonal, from 2 to 30 times the transducer dimensions) expended to calculate the impulse response of a single element transducer (9.28x9.28mm^2) - dashed reference method, solid proposed expressions.

2.5 Discussion

A method to compute near and far field transient pressure fields of rectangular transducers, for a point of observation outside the transducer aperture using low sampling frequencies has been presented. The method is based on the IR calculation approach presented by San Emeterio and Ullate, where the superposition method is avoided, and the analytical low pass filter proposed by D'hooge. Expressions to smooth the IR function with a rectangular pulse were derived.

Simulations to validate the accuracy and quantify the total speed up were made. For all points of observation, the IRs calculated with the classical and the proposed expressions were identical while the average speed up for all points of (around) 4 times was obtained. As expected, the new expressions are intrinsically faster than the reference method; this is especially notable when the point of observation goes far from transducer, which is when the reference method becomes significantly inefficient since the area of the synthetic rectangles outside the transducer aperture are considerably big, as can be noticed in Fig. 2.8.

Current 2D matrix array transducers have 32x32 elements (for a total of 1024 elements) or more. Linear extrapolation of the above-mentioned calculation times results in about 40 minutes for calculating the IR using the original formulation while with the new expression this reduces to about 10 minutes. Typically, a sound field (i.e. multiple points of observation) is required increasing the total computation time further and making the gain in absolute calculation times quite significant. In addition, if such arrays were simulated at high frequencies as required for the classical IR method, beamforming using a delay and sum approach would become a bottle neck due to the vast amount of data.
Finally, it should be noted that the proposed expressions were implemented in MATLAB and that implementation in a compiled computer language (e.g. C++) or on a GPU would further speed up the simulations times.

2.6 Conclusion

This new expression will be particularly relevant for 2D matrix transducer design where computation times remain currently a bottle neck in the design process.

3 A comparison of the performance of different multi-line transmit setups for fast volumetric cardiac ultrasound

Part of this work was published in: A. Ortega, J. Provost, L. Tong, P. Santos, B. Heyde, M. Pernot, and J. D'hooge, "A comparison of the performance of different multi-line transmit setups for fast volumetric cardiac ultrasound," *IEEE Trans. Ultrason. Ferroelectr. Freq. Control*, vol. 63, no. 12, pp. 1–1, 2016.

Abstract
It was previously demonstrated in 2D echocardiography that a proper multi-line transmit (MLT) implementation can be used to increase frame rate while preserving image quality. Initial findings for extending MLT to 3D showed that it might address the low spatiotemporal resolution of current volumetric ultrasound systems. However, to date, it remains unclear how much transmit/receive parallelization would be possible using a 3D MLT system. Therefore, the aim of this study was to contrast different MLT setups for 3D imaging by computer simulation in order to determine an optimal trade-off between the amount of parallelization of a MLT system and the corresponding signal-to-noise ratio of the resulting images. Hereto, the image quality of several MLT setups was estimated by quantifying their cross-talk energy level. The results showed that for the tested setups 4MLT broad beams and 9MLT narrow beams with Tukey (α=0.5) apodization in transmit and receive, give the highest frame rate gain while maintaining an acceptable inter-beam interference level. Moreover, although 16MLT narrow beams with Tukey/Tukey (α=0.5) apodization did show more pronounced inter-beam interference, its gain in frame rate might outweigh its predicted loss in image quality.

3.1 Introduction

Echocardiography is the modality of choice for physicians to visualize the heart as it offers several advantages over other imaging techniques. Furthermore, volumetric (3D) cardiac ultrasound has gained clinical interest due to the multi-dimensional nature of the heart, which makes it more intuitive for practitioners to interpret the resulting images. Typically, to image the whole heart a 75°x75° volume is required, which would take about ten thousand focused transmits to scan without parallelization at full (2D) line density (~100 emissions in both azimuth and elevation directions). Using a pulse repetition frequency (PRF) of 5kHz, which is common for transthoracic cardiac imaging, and given the above-mentioned scan configuration, the achievable frame rate would thus be about 0.5Hz. Obviously, this frame rate is too low to visualize a moving heart (beating around 60 times per minute) in real-time.

To overcome this limitation, different methods that have been presented mainly for 2D imaging to increase frame rate, have also been implemented for 3D acquisitions. Current state-of-the-art commercial systems make use of a combination of several of those techniques for fast volumetric imaging, such as limiting the field of view [41], decreasing the line density [42], using retrospective ECG gating [14], and/or applying parallel receive beamforming (i.e. multi-line acquisition, MLA) [25]. In this way, a frame rate of approximately 20-25Hz can be achieved at low/moderate line density for real-time/ECG-gated 3D recordings. Unfortunately, the gain in frame rate using these techniques typically comes at the expense of both spatial resolution and signal-to-noise ratio (SNR). Moreover, the achieved frame rate can only describe cardiac kinematics in a very rough manner as some of the cardiac phases (in particular the iso-volumetric phases) are known to be associated with very fast motion and deformation of the cardiac muscle [42].

As an alternative, multi-line transmit beamforming (MLT) has been proposed to increase temporal resolution without significantly compromising the spatial resolution and/or the SNR [18]. This is achieved by simultaneously transmitting multiple focused beams, thereby allowing for harmonic imaging [19]. Although potential artifacts such as cross-talk might be introduced due to the interaction between the MLT beams, we have recently demonstrated in 2D that they can be suppressed by using proper apodization [20][21]. Also, transmitting into multiple directions simultaneously implies the acoustic superposition of the MLT beams in the near field, which raises safety concerns. However, we recently demonstrated that by small modifications of the transmit beamforming the safety parameters can be adjusted to remain within safety regulations [43]. In addition, in order to test the feasibility of MLT for volumetric imaging, a preliminary study was

performed where the 2D findings were extrapolated to 3D. It was qualitatively shown that a 16MLT system could generate volumetric images with an acceptable image quality while speeding up the acquisition process by a factor of 16 [23].

Despite the fact that MLT can easily be combined with MLA to increase the gain in frame rate, to date, a direct comparison of different MLT beam setups customized for a different amount of MLA for fast 3D cardiac ultrasound imaging has not been performed. Hence, the aims of this study was to perform systematic computer simulations to determine the optimal trade-off between the amount of transmit and receive parallelization of a system and its cross-talk energy level, i.e. its effect on the image quality.

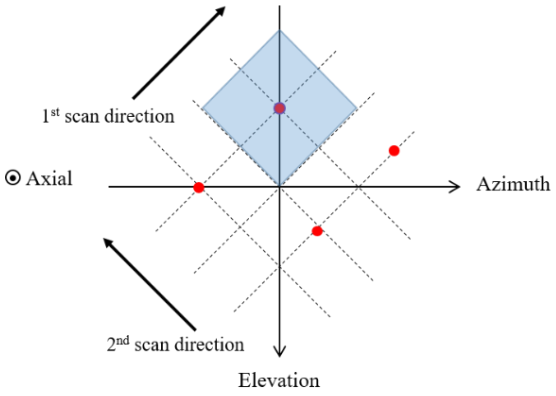

(a) 4MLT

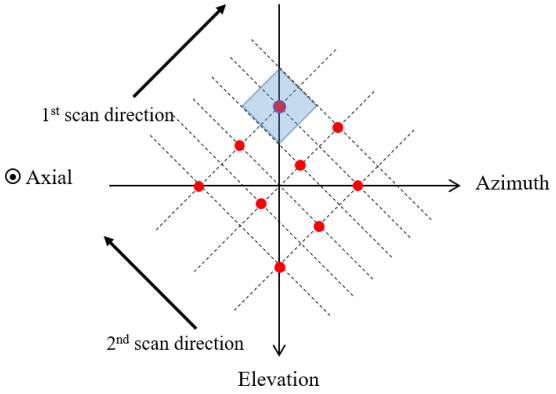

(b) 9MLT

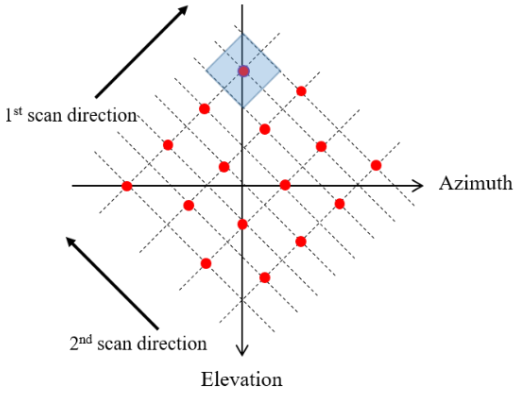

(c) 4MLT

Fig. 3.1. Top view of different staggered transmits patterns with (a) 4MLT, (b) 9MLT, (c) 16MLT beams. The red dots represent the transmit directions of the MLT beams at the center of each sub-volume, the shaded areas in each pattern exemplify the sub-volumes that a given MLT beam would cover during the volumetric scan.

3.2 Methods

3.2.1 Simulation setup

A 2D square phased array transducer (10x10mm^2, 32x32 elements) transmitting a Gaussian pulse with a central frequency of 2.5MHz and 50% bandwidth was simulated using a GPU-based implementation of the spatial impulse response method (Simpulse) [44]. The transmit beams were focused at 60mm while dynamic focusing was used during receive.

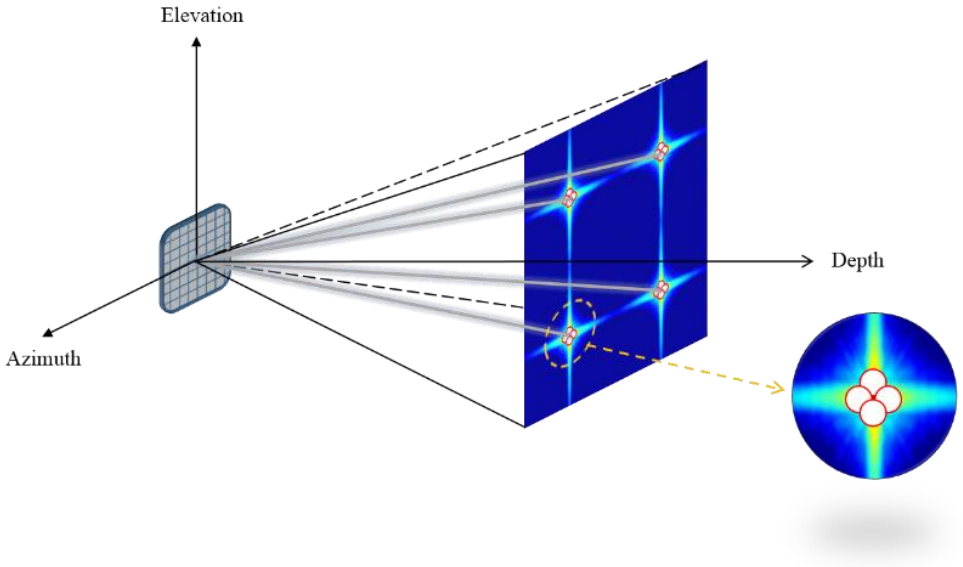

(a) Beams in a conventional spherical grid

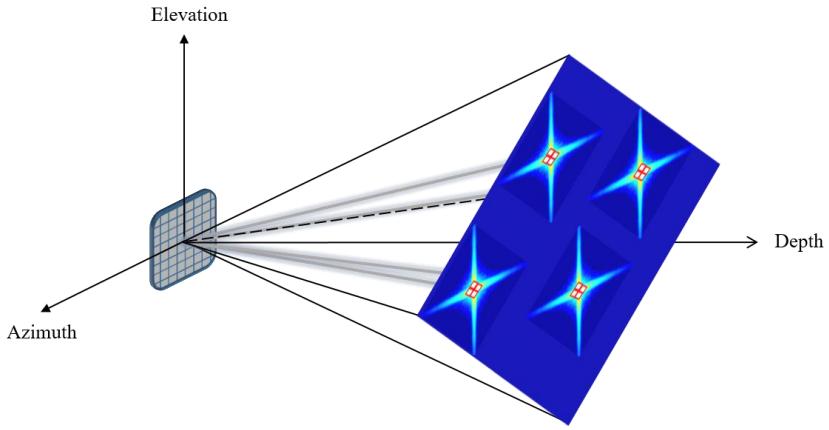

(b) Beams rotated along the diagonal and staggered

Fig. 3.2. Schematic of a 4MLT-NarrowBeams system in a plane parallel to the transducer surface (C-plane) where the parallel beams are located: (a) in a conventional spherical grid symmetric to the main directions of the transducer, and (b) 45^0 rotated respect to the transducer and staggered between azimuthal neighboring. The red circles around each beam profile represent the receive directions of each of the 4MLA beams, as can be seen in the zoomed image.

In our previous 2D findings [20], Tukey apodization (α=0.5), when applied in both transmit and receive, showed a significant suppression of cross-talk artifacts. However, the use of apodization broadens the acoustic beam which could lead to adverse effects. Therefore, the effect of such apodization in the 3D setting was also studied by quantifying the cross-talk level of the system with and without Tukey apodization.

3.2.2 MLT implementations

A 75°x75° pyramidal volume was divided into equally sized sub-volumes, where the number of sub-volumes was equal to the number of MLT beams (e.g. for a 4MLT system, the volume was divided into 4 sub-volumes). Each sub-volume represents the effective scanning area that each transmit beam would cover during a volumetric scan, exemplified as shaded areas in Fig. 3.1.

To further increase the temporal resolution, the beam width of the tested setups was customized based on the desired amount of receive parallelization (MLA) from each transmit beam. Hereto, equation 10 of [15] expresses the number of MLA beams (N_{MLA}) that need to be reconstructed from a single-line transmit beam (SLT) in order to satisfy the Nyquist sampling requirements given the specified oversampling factor, in 2D, as:

$$N_{MLA} = \frac{p^{tx}}{p^{txrx}}\left(1 + \frac{a^{rx}}{a^{tx}}\right), \tag{3.1}$$

where a^{tx} and a^{rx} are the transmit and receive aperture size respectively, and p^{tx} and p^{txrx} are the transmit and two-way oversampling factors respectively, which are the amount of overlap between the beams to avoid image artifacts due to inter-beam spacing. Assuming equal aperture size as well as oversampling factors in transmit and receive, to fully sample the field of view while limiting the number of transmissions, four parallel receive lines (or more if a smaller inter-beam spacing is used) symmetrically placed around each transmit beam must therefore be reconstructed. This implies that in 3D at least four parallel receive lines (two in azimuth and two in elevation) have to be simultaneously reconstructed from each narrow transmit beam (i.e. 4MLA). On the other hand, based on equation (3.1), to reconstruct at least four MLA's in each direction from a SLT beam (i.e. 16MLA), while using the same transmit and two-way oversampling factors, the original transmit aperture should be reduced to one ninth (i.e. by a third in each dimension), leading to a broadened transmit beam. Hence, in the present work, two beam widths were studied, narrow-beam (i.e. transmitted with the full aperture) and broad-beam (i.e. transmitted with a third of the aperture). The tested setups were: 4MLT-NarrowBeams, 4MLT-BroadBeams, 9MLT-NarrowBeams, 9MLT-BroadBeams, 16MLT-NarrowBeams and 16MLT-BroadBeams, resulting in an expected increase in frame rate by a factor of 16, 64, 36, 144, 64, and 256, respectively. Each setup was tested with and without Tukey ($\alpha = 0.5$) apodization. As an example, Fig. 3.2(a) shows a schematic of a 4MLT-NarrowBeams system in a plane parallel to the transducer surface.

Furthermore, according to the Fraunhofer approximation, the pressure field in the focal plane of a transducer can be approximated as the Fourier transform of the pressure distribution on the aperture. Therefore, the cross-section of the 2D beam profile of a rectangular aperture has the shape of a sinc-function in both azimuth and elevation direction. Thus, the pressure field on a 2D plane parallel to the transducer (C-plane) will have a cross-shape, similar to the ones shown in Fig. 3.2 implying that the side lobes of a rectangular transducer occur mostly in its main directions. As cross-talk occurs as the result of the interference between the main lobe of a MLT beam and the side lobes of (an)other MLT beam(s), earlier studies have proven that it can be reduced by positioning the transmit beams along the diagonal of the aperture [45]. Additionally, we have previously demonstrated that further cross-talk reduction can be obtained by spatially separating the beams in neighboring planes by means of staggering the MLT transmit directions [23]. Therefore, in order to suppress cross-talk as much as possible, in the present implementations, the simultaneous transmit beams were rotated 45° to be along the diagonal of the transducer and staggered between neighboring planes, as illustrated in Fig. 3.3(b). This beam configuration is also displayed in Fig. 3.2(b).

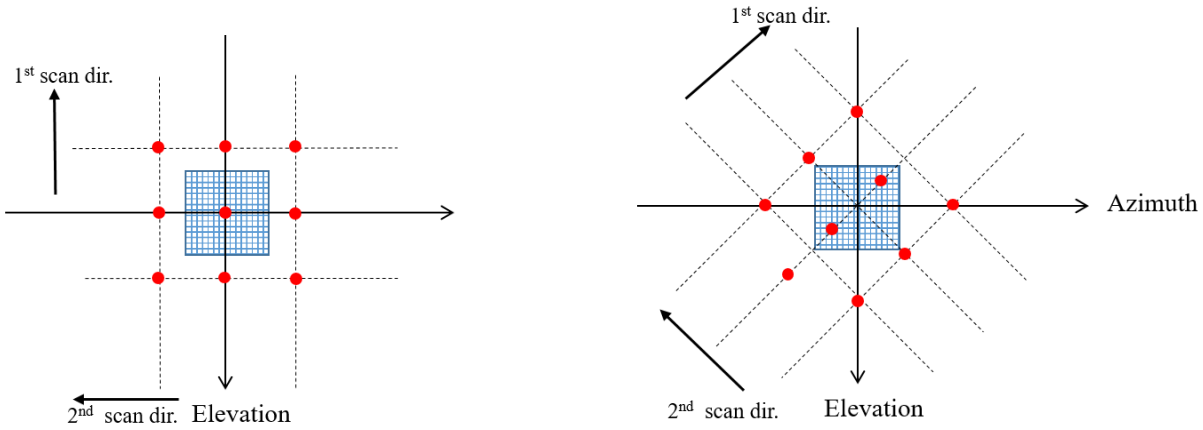

(a) Conventional spherical grid (b) Rotated along the diagonal and staggered

Fig . 3.3. Top view of the steering transmits directions for a 9MLT system with respect to the rectangular aperture (central blue square), (a) conventional spherical grid symmetric to the main directions of the transducer, (b) 45^0 rotated respect to the transducer and staggered between neighboring planes.

3.2.3 Cross-talk quantification

To quantify the inter-beam perturbation of the tested systems, two-way beam profiles of a beam transmitted into one of the MLT directions (θ_i) and subsequently receiving along each of the MLT beam directions (including the same transmit direction - $\theta_{1\dots i\dots j}$), were simulated on a C-plane at 65mm (around half way of the common image line length for cardiac applications). The sum of the energy (i.e. the squared peak pressure amplitudes) while transmitting and receiving in the same MLT direction was defined as the SLT energy (i.e. the ideal situation), whereas the sum of the energy that deviates from the transmit beam towards the other remaining MLT directions, i.e. when transmitting in a given MLT direction but receiving in one of the other remaining MLT directions, was considered cross-talk. This procedure was repeated for every MLT beam in the setup. Then, the final cross-talk energy level (E_{xtalk}), was quantified in decibels. Mathematically, this can be expressed as:

$$E_{xtalk} = 10 * log10\left(\frac{\sum_{i=1}^{\#mlt}\sum_{j=1,j\neq i}^{\#mlt} E^{\theta ij}}{\sum_{i=1}^{\#mlt} E^{\theta ii}}\right), \tag{3.2}$$

where: i, is a given MLT direction being assessed; j, is a MLT directions different from the direction being tested (i); $\#mlt$, is the total number of MLT beams in the system; $E^{\theta ij}$, is the energy in the C-plane when transmitting in a given MLT direction i and receiving in one of the other direction (j) (i.e. cross-talk); and $E^{\theta ii}$, is the energy in the C-plane, when transmitting in a given MLT direction i and receiving in the same direction i (i.e. SLT energy).

Based on a retrospective analysis of our previous work on 2D MLT, a cross-talk energy level of -30dB was defined as a cut-off to obtain acceptable B-mode SNR. Indeed, this cross-talk level was originally found by computer simulation [20] and later showed to produce good image quality in experimental setups and *in-vivo* despite the different acoustic properties of the distinct cardiac structures [21].

The present *in-silico* study was divided into the following parts. First, in order to evaluate the cross-talk energy level of all the different systems, a single transmit event was used. Namely, the directions of the MLT beams corresponding to the center of each of their sub-volumes were simulated (cf. Fig. 3.1). Then, to test the performance throughout the entire volume, the best configurations for each of the tested MLT setups was also evaluated at two other depths, i.e. 35mm and 95mm. Moreover, the MLT configurations that gave the highest frame rate gain while keeping an acceptable cross-talk

level were evaluated at four other steering directions in each sub-volume in order to further assess its performance, as illustrated with dots of different colors in Fig. 3.4, for a 16MLT system. Finally, other authors have proposed to position the 4MLT beams in the volume along a single diagonal instead of a rhombus [45]. To contrast the proposed MLT configurations against this one, additional simulations were performed using this single diagonal configuration using 4MLT-NarrowBeams with Tukey (α=0.5) apodization.

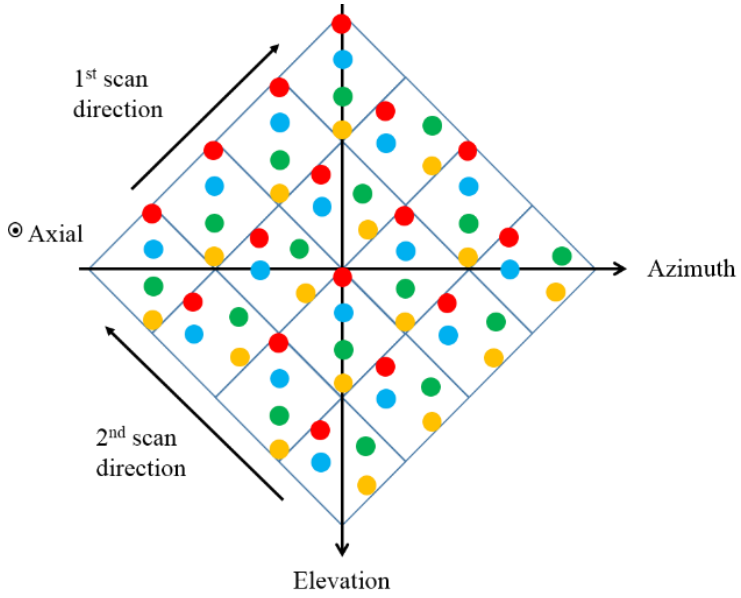

Fig. 3.4. Graphical representation of a 16MLT system of the four steering directions in each sub-volume used to assess the relationship between the steering angles and the cross-talk energy level of the system. The different colours represent the different transmit events.

3.3 Results

As an example of the two-way beam profiles used to calculate the cross-talk level of a 4MLT system, Fig. 3.5 shows the two-way beam profiles in a C-plane, at 65mm, of the MLT beam transmitting in one direction and receiving in each of the MLT directions a) for narrow-beams without apodization, b) for narrow-beams with apodization, c) for broad-beams without apodization and d) for broad-beams with apodization.

The cross-talk energy levels of all the tested setups are given in Fig. 3.6. Of the broad-beams systems, only the 4MLT without apodization reached the pre-defined threshold of -30dB and it could be observed that apodization had minimal, or even adverse, impact to reduce inter-beam perturbations for these configurations. On the other hand, for narrow-beam transmits, the 4MLT and 9MLT configuration reached the -30dB level while apodization could further suppress cross-talk. Although the 16MLT system in this configuration did not reach the pre-defined threshold, it did reach a -28.8dB cross-talk level. Finally, the configuration using 4MLT-NarrowBeams with apodization along a single diagonal did not reach the pre-defined threshold and performed worse than the other MLT configurations using a similar transmit configuration.

As narrow-beams with transmit and receive apodization gave the best performance for all MLT configurations, the cross-talk levels of these systems together with 4MLT-BroadBeams were also studied at 35mm and 95mm (Fig. 3.7). The 4MLT-BroadBeams and 9MLT-NarrowBeams systems showed relatively stable cross-talk levels over the whole depth range tested, while the cross-talk level of the 4MLT and 16MLT-NarrowBeams configurations deteriorated at larger depth.

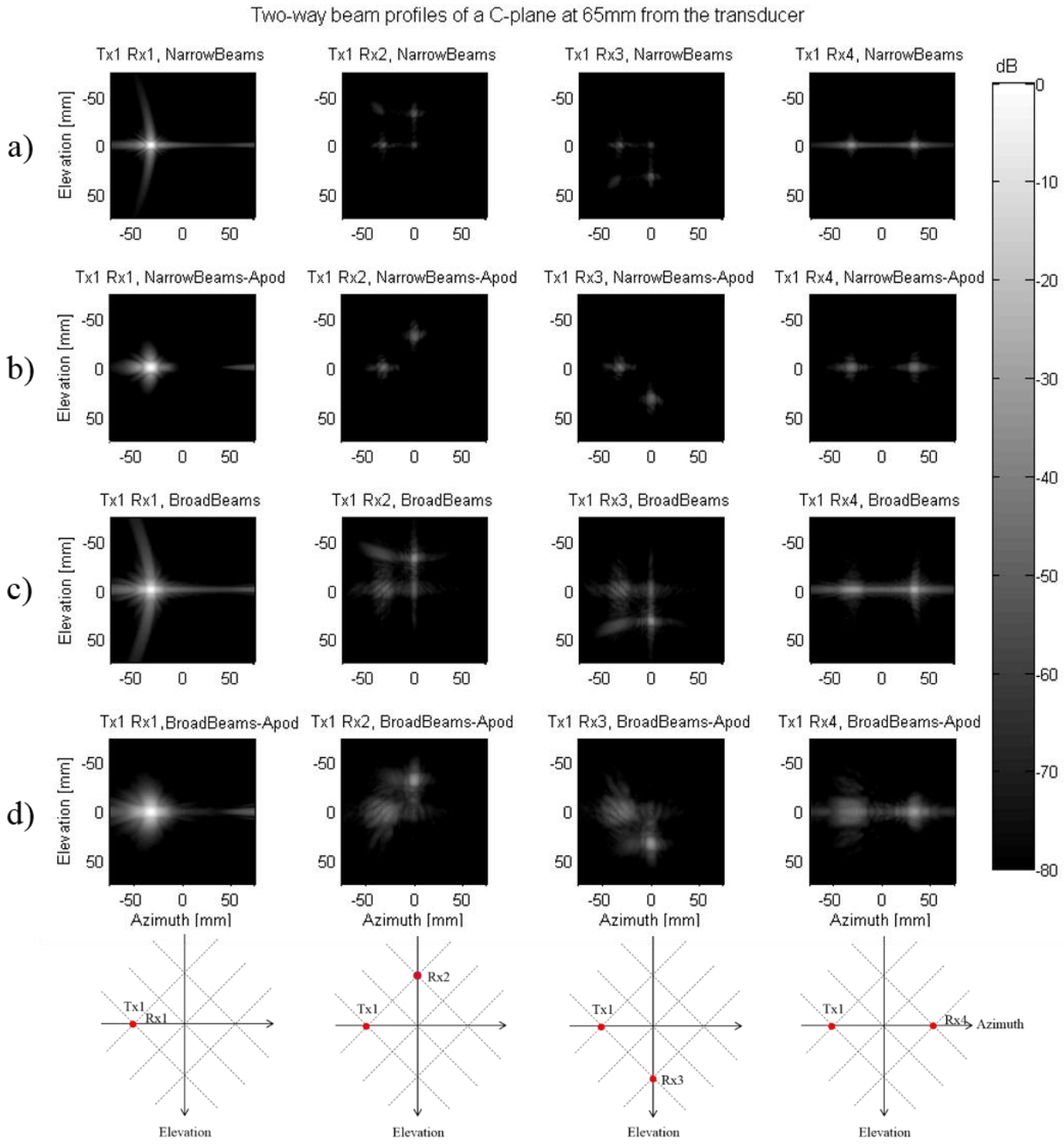

Fig. 3.5. The two-way beam profiles of a 4MLT system on a C-plane, at 65mm, when transmitting at the first direction (i.e.θ_i) and receiving in all other MLT directions (i.e.$\theta_1,..\theta_i,..\theta_j$). The effect of transmit and receive Tukey apodization (α = 0.5) was studied in two of the four configurations. (a) 4MLT-NarrowBeams without apodization, (b) 4MLT-NarrowBeams with apodization, (c) 4MLT-BroadBeams without apodization and (d) 4MLT-BroadBeams with apodization. A representation of the transmit and receive beams positions can be found at the bottom of each column. The first column can be seen as the single line transmit signal, and the remaining columns as noise (i.e. cross-talk).

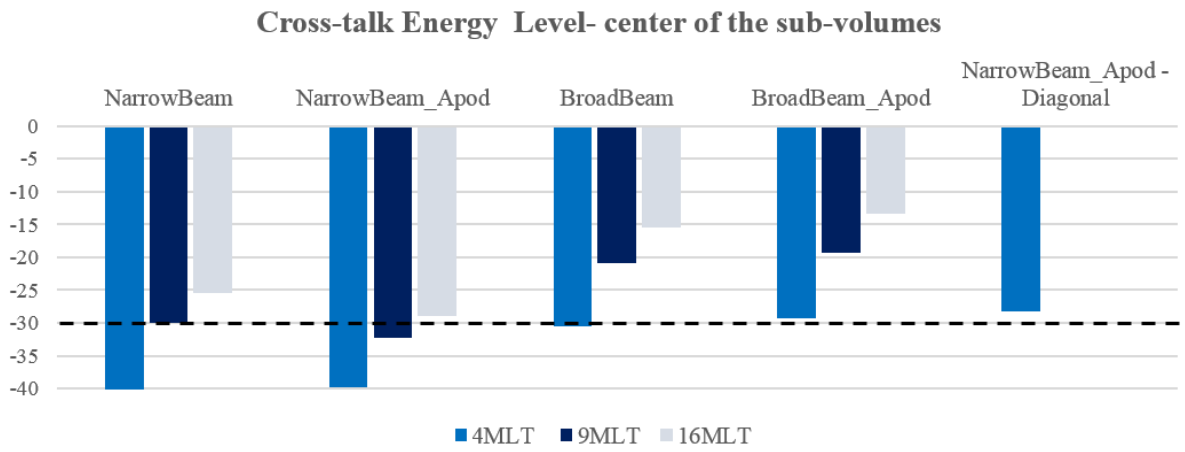

Fig. 3.6. Cross-talk energy level of the different tested setups: 4MLT-NarrowBeams, 4MLT-BroadBeams, 9MLT-NarrowBeams, 9MLT-BroadBeams, 16MLT-NarrowBeams, 16MLT-BroadBeams, all with and without Tukey (α= 0.5) apodization, and 4MLT-NarrowBeams with apodization positioned along a single diagonal. The cross-talk cut-off was defined as -30dB for an acceptable B-mode image quality.

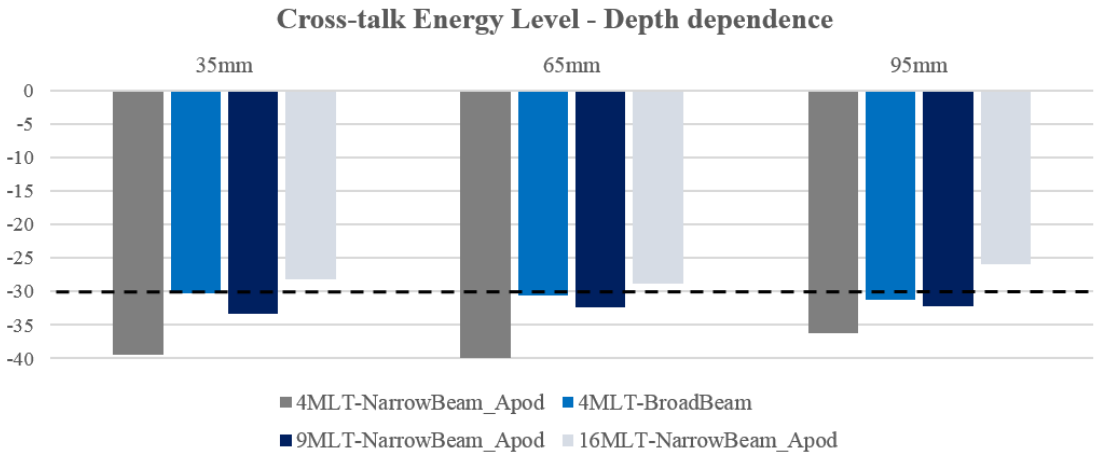

Fig. 3.7. Cross-talk energy level of the systems with the lowest inter-beam interference at the centre of the sub-volumes (4MLT-NarrowBeams, 4MLT-BroadBeams, 9MLT-NarrowBeams with Tukey/Tukey apodization and 16MLT-NarrowBeams with Tukey/Tukey apodization.) tested at two more depths (i.e. 35mm and 95mm) to evaluate their depth dependence.

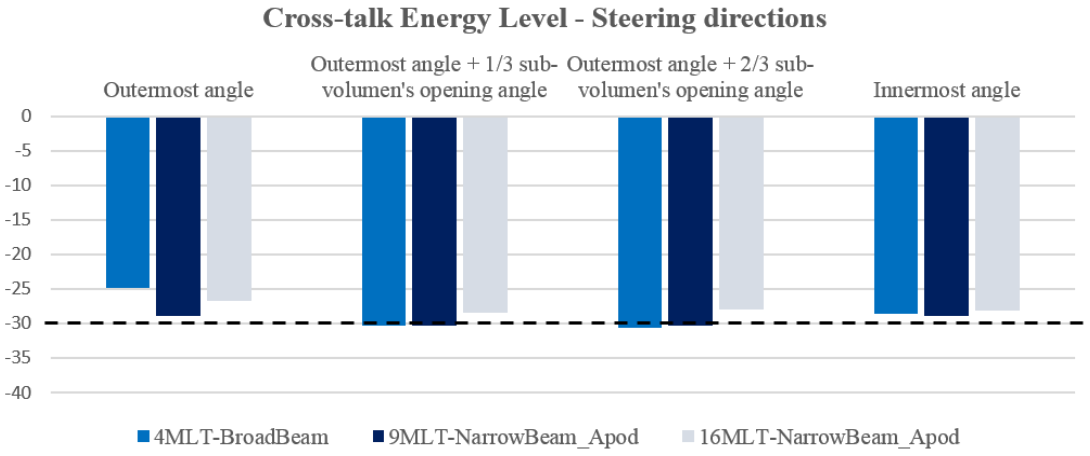

Fig. 3.8. Cross-talk energy level of the 4MLT broad beams, and 9MLT and 16MLT narrow beams with apodization steered in four different directions inside each sub-volume to evaluate the inner and outer scenarios. The directions are represented different colours in Fig. 4.

Based on the above findings, the systems that gave the highest frame rate with an acceptable cross-talk level were also tested for their steering properties, i.e. 4MLT-BroadBeams and 9MLT-

NarrowBeams with Tukey apodization. Moreover, even though the 16MLT-NarrowBeams with Tukey apodization configuration did not reach the predefined cross-talk levels nor performed well in depth, it was taken along in this further analysis given that its gain in frame rate might ultimately compensate for its loss in image quality. The results presented in Fig. 3.8 demonstrate that for the 4MLT-BroadBeams, 9MLT-NarrowBeams and 16MLT-NarrowBeams systems the cross-talk remained relatively stable within the volume while steering with the exception of the outer most steering angle that resulted in higher inter-beam interference, particularly for the 4MLT and 16MLT setup.

3.4 Discussion

In this study, the cross-talk energy level of different MLT systems was quantitatively investigated by computer simulation. Overall, this study showed that the 4MLT-BroadBeams and 9MLT-NarrowBeams with transmit/receive apodization has limited cross-talk although our -30dB threshold was not strictly met while steering inside the sub-volumes. Nevertheless, it could thus be expected that these MLT setups can generate good quality volumetric images at a 64-fold and 36-fold frame rate respectively, compared to conventional single line transmit/receive scanning. As such, given the system configuration specified in section (3.1) and using equation (1.13), the 4MLT configuration could generate a volumetric cardiac ultrasound image at full 2D line density at 32Hz while the 9MLT at about 20Hz. Further improvements in temporal resolution can be achieved by reducing line density and/or interpolating the received scanline data.

The 16MLT-NarrowBeams apodized configuration did not reach the required -30dB threshold and showed to have more depth-dependent cross-talk levels. The latter is likely the result of the small inter-beam spacing in combination with a relatively small transducer aperture. Similarly, the relatively small aperture makes steering towards the edges of the 75x75 degree volume difficult especially in the far-field, resulting in higher cross-talk levels. Nevertheless, the overall cross-talk levels approximated the -30dB threshold. Given the significant gain in frame rate for this configuration, the expected drop in image quality with respect to the 9MLT system might therefore be clinically acceptable as this configuration would result in an overall acquisition parallelization of 64 and thus a frame rate of 32Hz at full 2D line density.

Although 4MLT-BroadBeams and 16MLT-NarrowBeams have the same gain in frame rate, the former showed less cross-talk artifacts in all the tested setups despite the use of less-focused beams. In addition, transmitting less parallel beams would decrease the constraints on the system's hardware and safety concerns. On the other hand, the associated broad beams might result in lower beam intensities and thus limit their capability to generate harmonics. Given that it is not trivial to model these effects in simulations, experimental validation will have to demonstrate which of these two alternatives performs better. Of note is that the transducer aperture studied in this paper was relatively small (~1cm^2) as fully wiring and controlling a bigger aperture remains impractical. Of course, reducing the aperture of such a relatively small probe in order to generate broad beams would likely reduce the transmitted energy unacceptably with significant impact on the image quality and penetration. Nevertheless, given that larger apertures may become available in the future, this configuration was studied from the theoretical point of view and for completeness of the study. However, as image quality on the available array would likely be low, the 4MLT-BroadBeams configuration was not considered for experimental validation. Nevertheless, according to our simulations, both imaging schemes showed the capability of keeping the cross-talk levels acceptable.

Please note that a 3D opening angle of 75x75 degrees is relatively large for a 1cmx1cm 2D phased array. As such, potential solutions to the steering issue discussed above are: 1) to reduce the opening angle of the volume with the implication of reducing the inter-beam spacing between the MLT

beams and thereby increasing cross-talk levels, or 2) to keep the opening angle and the inter-beam spacing, but to modify the scan sequence in such a way that the corners of the volume remain unsampled (cf. Fig. 3.9). The latter solution would imply that for a 16MLT system only 14MLT beams would effectively be required to scan the non-pyramidal volume as illustrated in Fig. 3.9.

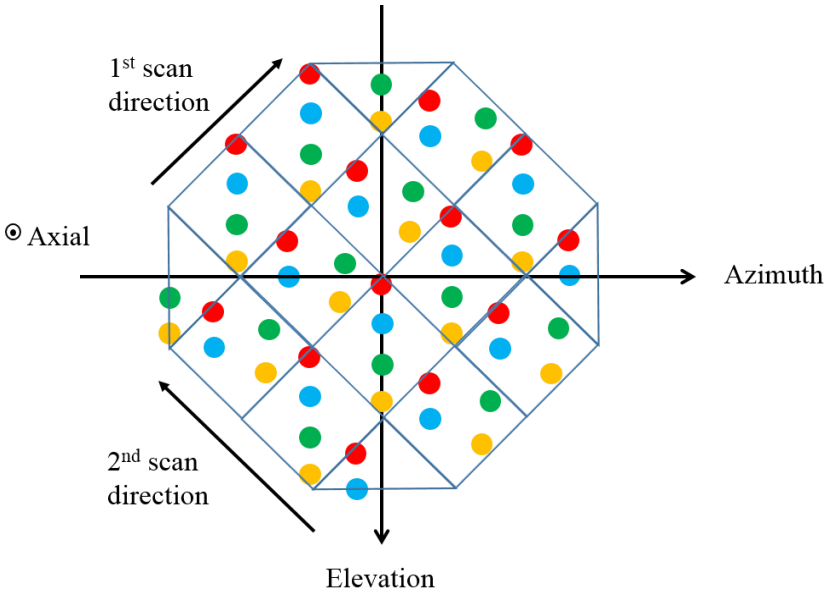

Fig. 3.9. Possible solution to avoid scanning the corners of the volume while preserving the opening angle and the inter-beam spacing. In the figure, the representation of the four steering directions proposed in Fig. 4 with the presented solution. It can be noticed that such scanning sequence would imply that for the given 16MLT system, where the volume is sub-divided into 16 sub-volumes, only 14MLT beams would be required, i.e. the same beam could cover the halfs sub-volumes in azimuth direction, likewise in elevation direction.

Overall, the previously proposed single-diagonal configuration did not reach our predefined -30dB threshold value. The major reason for this is that this configuration leads to a small inter-beam spacing of 18.75° (compared to e.g. 37.5° for the 4MLT rhombus configuration). Furthermore, it is worthwhile mentioning that the cross-talk levels reported in [45] are better than the values presented here. However, these values cannot be directly compared to the ones in the present manuscript. First, the definition of cross-talk in [45] was different. In addition, the aperture size and the number of crystals in [45] were significantly larger (20.5x16.4 mm^2, 120x96 crystals) which allowed for better focusing throughout the volume. Finally, the opening angle (90°x90°) used in [45] was also larger compared to ours (75°x75°).

It should be noted that cross-talk depends on the exact system configuration [20]. Therefore, the results presented here are only valid for the tested system setup (including the transducer specifications and imposed apodization) and should not be directly generalized. The probe characteristics used in this study are typical for fully wired (experimental) 2D phased-array for 3D cardiac imaging [16].

Moreover, in this simulation study, only artifacts resulting from transmit beamforming were considered. Therefore, the drawbacks of MLA implementations due to the misalignment of the received beams with respect to the transmitted beam [15] were not investigated explicitly, although these effects were intrinsically included in the experimental analysis. Furthermore, when using apodization in transmit, the effective emitted energy is reduced and the beam width is broadened, which intrinsically affects both the spatial resolution and the SNR of the system. This explains why using apodization for the broad-beams systems, resulted in little improvement (or even deterioration) of the quantified energy levels. In order to avoid this, it was recently suggested that the second-harmonic signal could be used to reduce inter-beam perturbations [19].

3.5 Conclusion

For the tested system configuration, the 4MLT-BroadBeams and the 9MLT-NarrowBeams with transmit/receive apodization (Tukey $\alpha = 0.5$) showed acceptable cross-talk levels while achieving a 64-fold and 36-fold frame rate respectively if combined with 16MLA and 4MLA respectively. Although the tested 16MLT-NarrowBeams configuration with the same apodization did not reach the predefined cross-talk limits, its gain in frame rate might outweigh its loss in image quality.

4 Multi-line transmit imaging for volumetric cardiac ultrasound imaging: experimental validation

Part of this work was published in: A. Ortega, J. Provost, L. Tong, P. Santos, B. Heyde, M. Pernot, and J. D'hooge, "A comparison of the performance of different multi-line transmit setups for fast volumetric cardiac ultrasound," *IEEE Trans. Ultrason. Ferroelectr. Freq. Control*, vol. 63, no. 12, pp. 1–1, 2016.

Abstract
Multi-line transmit (MLT) beamforming has shown promising results for 2D ultrasound imaging in order to increase frame rate while keeping a good image quality both *in-silico* and *in-vivo*. Furthermore, these findings were extrapolated to 3D in an extensive *in-silico* study, where several parallelized systems showed to potentially be able to generate volumetric images while speeding up the acquisition process. However, experimental proof of the viability of the proposed approach is currently lacking. Moreover, implementing a 3D MLT sequence on a physical scanner brings along challenges as it requires non-identical electric excitation pulses (EEPs) to be applied to all elements in the matrix array. These pulses are defined as the sum of the EEPs that would be applied on a given element when transmitting each transmit beam separately. This summing process can result in the superposition of the EEPs therefore requiring arbitrary wave form generators or at least multi-level electrical pulsers. However, most of the currently available systems make use of bi- or tri-state pulsers making the implementation of MLT not straightforward. This problem is particularly relevant for 3D imaging as the superposition of EEPs can become significant (e.g. up to 16 for a 16MLT imaging sequence). The aim of this study was therefore two-fold: 1) to corroborate the *in-silico* findings experimentally, and 2) to find a practical solution to transmit MLT beams using tri-state pulsers. As such, MLT images where generated synthetically from single-line transmit sequences, and the 9MLT and 16MLT focused beams systems were tested experimentally. For both systems, 4 receive lines were reconstructed from each transmit beam. The contrast-to-noise ratio of these imaging strategies was quantified and compared to the image quality obtained with line-by-line scanning. Despite some expected loss in image quality, the resulting images of the parallelized systems were very competitive to the benchmark, while speeding-up the acquisition process by a factor of 36 and 64 respectively. On the other hand, clipping the EEPs showed to better preserve the transmit pattern despite its energy lost.

4.1 Introduction

Multi-line transmit beamforming (MLT) has been demonstrated to be able to increase temporal resolution without significantly compromising the spatial resolution and/or the SNR of the system in 2D echocardiography [21][20]. This is achieved by simultaneously transmitting multiple focused beams (Fig. 4.1(b)), instead of the conventional line-by-line acquisition, also called single-line transmit (SLT), (Fig. 4.1(a)). Thereby, the frame rate is increased by a factor equal to the number of MLT beams.

(a) (b)

Fig. 4.1. Scanning sequence for a (a) SLT, and a (b) 4MLT system. Reproduced with permission from [12]

In order to extend the 2D findings to 3D, an extensive *in-silico* study [46] was performed to estimate the maximum amount of transmit and receive parallelization of a system while preserving an adequate image quality. The results showed that for the tested setups 4MLT broad beams and 9MLT narrow beams with Tukey (α=0.5) apodization in transmit and receive, give the highest frame rate gain while maintaining an acceptable inter-beam interference level. Moreover, although 16MLT narrow beams with Tukey/Tukey (α=0.5) apodization did show more pronounced inter-beam interference, its gain in frame rate might outweigh its predicted loss in image quality.

Therefore, an experimental validation of these findings including a quantification of the systems' performance is required.

Nevertheless, transmitting into several directions simultaneously requires the application of non-identical electric excitation pulses (EEPs) to all elements in the phased array transducer. These pulses are defined as the sum of the EEPs that would be applied on the individual elements when emitting the transmit beams separately. As an example, Fig. 4.2 shows the pulses that would be applied to individual elements of a transducer in order to transmit in two directions consecutively (Fig. 4.2(a-b)), and simultaneously (Fig. 4.2(c)). As this sum will result in the superposition of the EEPs, to date, MLT implementations were done on systems having arbitrary waveform generators (AWG). This is particularly relevant for 3D imaging as the superposition of EEPs can become significant (e.g. up to 16 for a 16MLT imaging sequence). However, as most of the available scanners are equipped with a tri-state pulse generator, the implementation of an MLT sequence on such scanner is not straightforward.

Therefore, the aim of this study were 1) to perform an *in-vitro* validation of the *in-silico* findings, and 2) to find a practical solution to transmit MLT beams using tri-state pulsers.

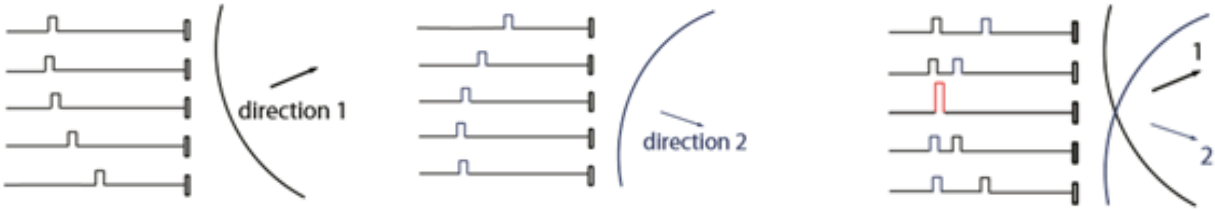

(a) Transmit direction 1 (b) Transmit direction 2 (c) Sum of transmit direction 1 and 2

Fig. 4.2. Pulses to be applied on individual elements of a phased-array transducer to generate two conventional, focused single line: (a) and (b) consecutively; (c) simultaneously. Reproduced with permission from [12].

4.2 Methods

4.2.1 3D MLT validation

To corroborate the *in-silico* findings while avoiding the complexity of implementing the superposed EEP, the MLT beams can be created synthetically by combining the respective channel data off-line, as previously described for 2D MLT imaging [47]. For instance, to generate a 4MLT system synthetically, the channel data of 4 SLT on the corresponding directions for a given transmit event are summed prior to image reconstruction. Volumetric data sets were acquired using an open, flexible, 1024-channel ultrasound imaging platform [16]. This ultrasound scanner is equipped with a 2D phased array with similar configurations as the one used in Chapter 3. Please note that - in contrast to the results presented in Chapter 3 - no transmit apodization was applied when acquiring the SLT channel data. The reason for this is the fact that duty cycle modulation to allow for apodization using tri-state pulsers had not been implemented before on the experimental system at hand. The implementation of the transmit apodization is part of ongoing work.

Two of the MLT setups studied in Chapter 3 were experimentally tested: 1) the one that showed the overall best performance (i.e., 9MLT-NarrowBeams), and 2) the one that – after preselecting the better configurations – gave the overall worst performance (i.e., 16MLT-NarrowBeams). The two extremes, out of the better configurations, were taken to get an impression of the range in image

quality encountered for systems expected to have limited cross-talk. Furthermore, SLT/single-line acquisition (SLA) imaging was also performed as a benchmark.

A general-purpose ultrasound phantom (054GS, CIRS, VA) and a static heart-mimicking phantom (067, CIRS, VA) were imaged at the same voltage with the three different systems. The contrast-to-noise ratio (CNR) of the systems was calculated as:

$$CNR = \frac{\mu_{dB\_bck} - \mu_{dB\_cyst}}{\sqrt{\sigma^2_{dB\_bck} + \sigma^2_{dB\_cyst}}}, \tag{4.1}$$

where, μ_{dB_bck} and μ_{dB_cyst} are the mean gray levels in the background and cystic regions respectively, and $\sigma^2_{dB\_bck}$ and $\sigma^2_{dB\_cyst}$ are their respective standard deviations. For the heart-mimicking phantom, the CNR was quantified at two different positions: 1) between the tissue and the cavity, and 2) between the tissue and the housing liquid (acrylonitrile butadiene styrene -ABS-).

4.2.2 MLT scan sequence implementation on a system using tri-state pulsers

In US imaging, the emitted acoustic pulse is mathematically the convolution between the EEPs applied to the individual elements and the transfer function of the transducer (i.e. its impulse response). Thus, one way to evade the superimposed EEPs related to MLT sequences, and still emit simultaneous beams into different directions, could be to approximate the desired acoustic pulse, and deconvolve it with the known impulse response function. However, deconvolution algorithms are not trivial and can have several solutions, therefore, affecting the reproducibility of MLT implementations. Moreover, another way to avoid the superimposed EEP is by modifying the EEP to be within the tri-state pulser range. Therefore, two approaches were tested in order to adapt the superimposed EEPs into trinary sequences:

1) EEP width modulation, the EEP is ‘superimposed’ in time instead of in amplitude using bipolar pulses, i.e. an EEP that overlaps n times in amplitude can be approximated by elongating the pulse n times in time. In this way, the emitted amount of energy is closer to the one required for an ideal MLT system. However, long pulses cause spectral zero crossings that may fall in the bandwidth of the probe and thereby affect the spectral properties of the transmitted acoustic pulse. Therefore, such elongation is restricted by the maximum width of the ideal pulses. Additionally, the whole pulse train has to be scaled with respect to the maximum enlargement in order to preserve the waveform as much as possible.

2) Clipping, where any amplitude outside the voltage level is neglected. This method, preserves the waveform shape but attenuates its amplitude, implying that less energy is effectively transmitted on given elements for given transmit events than the MLT system strictly requires.

A 32x35 matrix array centered at 3MHz with a 50% bandwidth at -3dB and a 0.3 mm pitch, was used to simulate the acoustic fields of a 4, 9 and 16MLT systems using the ideal, clipped and width modulated EEPs. To quantify which of the above-mentioned methods is closer to the ideal MLT implementation, the sum of the squared differences (SSD) between the ideal and clipped pulses was computed, as well as the SSD between the ideal and the width approximated pulses, on a C-plane at the focal depth (i.e. 40mm).

4.3 Results

As for the experimental validation, the phantoms were scanned using SLT/SLA sequence and the 9MLT-NarrowBeams and 16MLT-NarrowBeams were synthetically generated from the acquired channel-data. In both parallelized systems, four receive lines (i.e., multi-line acquisition – MLA) were reconstructed per MLT beam. The resulting images are shown in Fig. 4.3 and 4.4. The CNR of the generic phantom with the benchmark system (i.e., SLT/SLA) was 3.50, while for the 9MLT-4MLA and 16MLT-4MLA systems it was both 2.96. For the heart-mimicking phantom, the CNRs between the tissue and the cavity were 3.17, 2.59 and 2.60 respectively, while the CNR between the tissue and the bottom of the phantom was 3.17, 2.37 and 2.14 respectively. All CNR values are reported in table 4.I.

Table 4.I. Detailed values for the CNR quantification of each phantom with the three imaging strategies.

Phantom	**Scan Sequence**	μ_{env_bck}	σ_{env_bck}	μ_{env_cyst}	σ_{env_cyst}	CNR
General Purpose (Background/Cyst)	SLT-SLA	40,02	3,62	22,12	3,61	3,50
	9MLT-4MLA	38,21	4,21	20,65	4,19	2,96
	16MLT-4MLA	35,56	4,13	18,24	4,13	2,96
Heart-Mimicking (Muscle/Cavity)	SLT-SLA	13,01	4,11	0,01	0,12	3,17
	9MLT-4MLA	11,75	4,51	0,05	0,34	2,59
	16MLT-4MLA	11,91	4,45	0,21	0,71	2,60
Heart-Mimicking (Muscle /Housing liquid)	SLT-SLA	13,01	4,11	0,00	0,01	3,17
	9MLT-4MLA	11,75	4,51	0,67	1,28	2,37
	16MLT-4MLA	11,91	4,45	1,50	1,96	2,14

On the other hand, Fig. 4.5 shows an example of the EEPs approximated approaches. It presents the EEP and their respective acoustic fields of a 4MLT system simulated with the ideal, approximated and clipped. It can be visually noted that the pressure generated with the clipped EEP resembles the ideal MLT case better. Furthermore, the SSD corroborated this qualitative observation, where for the 3 MLT systems the mean SSD for the width modulated EEPs was bigger by one order of magnitude compared to the clipped EEPs (2.59e-20dB vs 4.28e-21dB respectively).

4.4 Discussion

The MLT imaging was generated synthetically by summing the channel data of the corresponding SLT events prior to beamforming. Although this should not impact image quality in simulations, in practice, thermal and/or electronic noise will cumulate as 10*log10(N_MLT), where N_MLT is the number of MLT beams in the system. As such, it can be anticipated that the SNR of the synthetically generated MLT images in this study was lower than what would have been obtained with a true MLT transmission (i.e. 9.5dB, and 12dB for the 9MLT and 16MLT respectively). This may explain the lower SNR of the MLT images at larger depths in Fig. 4.3. On the other hand, in order to transmit a true MLT sequence, the electric excitation pulses of each MLT beam are summed resulting in a superposition of the pulses, particularly for the central elements of the transducer. As such, the transmit amplitude of the individual MLT beams needs to be decreased for the superimposed excitation to be within the voltage range that can be generated by the transmit system. Given that in synthetic MLT this ‘down scaling’ was not required, the SNR of the synthetic MLT images may be positively biased. It is difficult to predict theoretically which of the above-mentioned effects would prevail but determining this experimentally is part of on-going work.

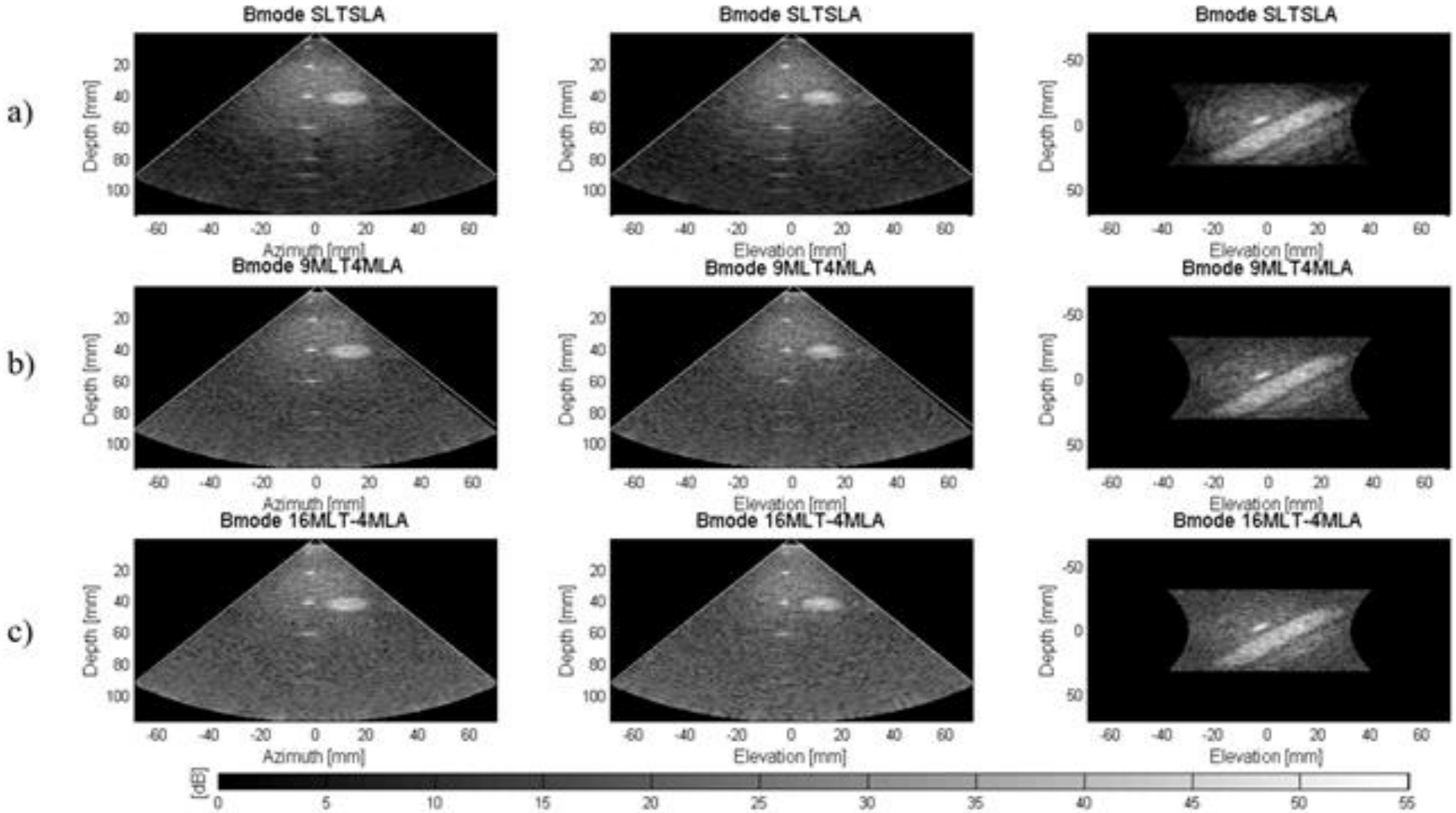

Fig. 4.3 Images of the general-purpose phantom CIRS (054GS) acquired with (a) SLT-SLA, (b) 9MLT-4MLA and (c) 16MLT-4MLA, all with Tukey (α=0.5) apodization on receive. Columns represent from left to right the azimuth plane, elevation plane and C-plane respectively.

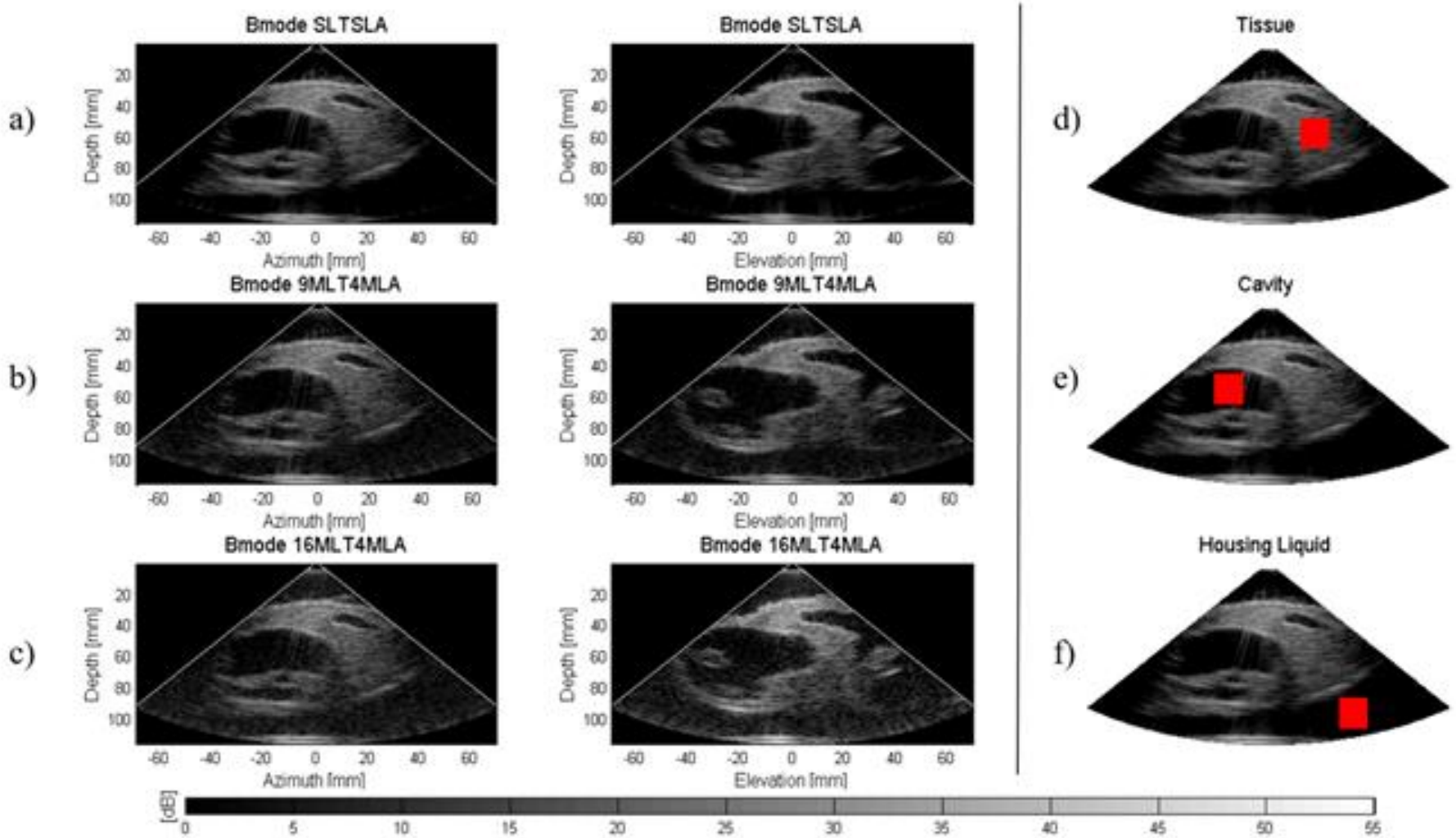

Fig. 4.4. Images of the heart-mimicking phantom CIRS (064), acquired with (a) SLT-SLA, (b) 9MLT-4MLA and (c) 16MLT-4MLA, all with Tukey (α=0.5) apodization on receive. From left to right the figures are the azimuth and elevation planes respectively. The last column demonstrates the regions of interest used to quantify the CNR, (d) tissue, (e) cavity and (f) housing liquid at the bottom of the phantom.

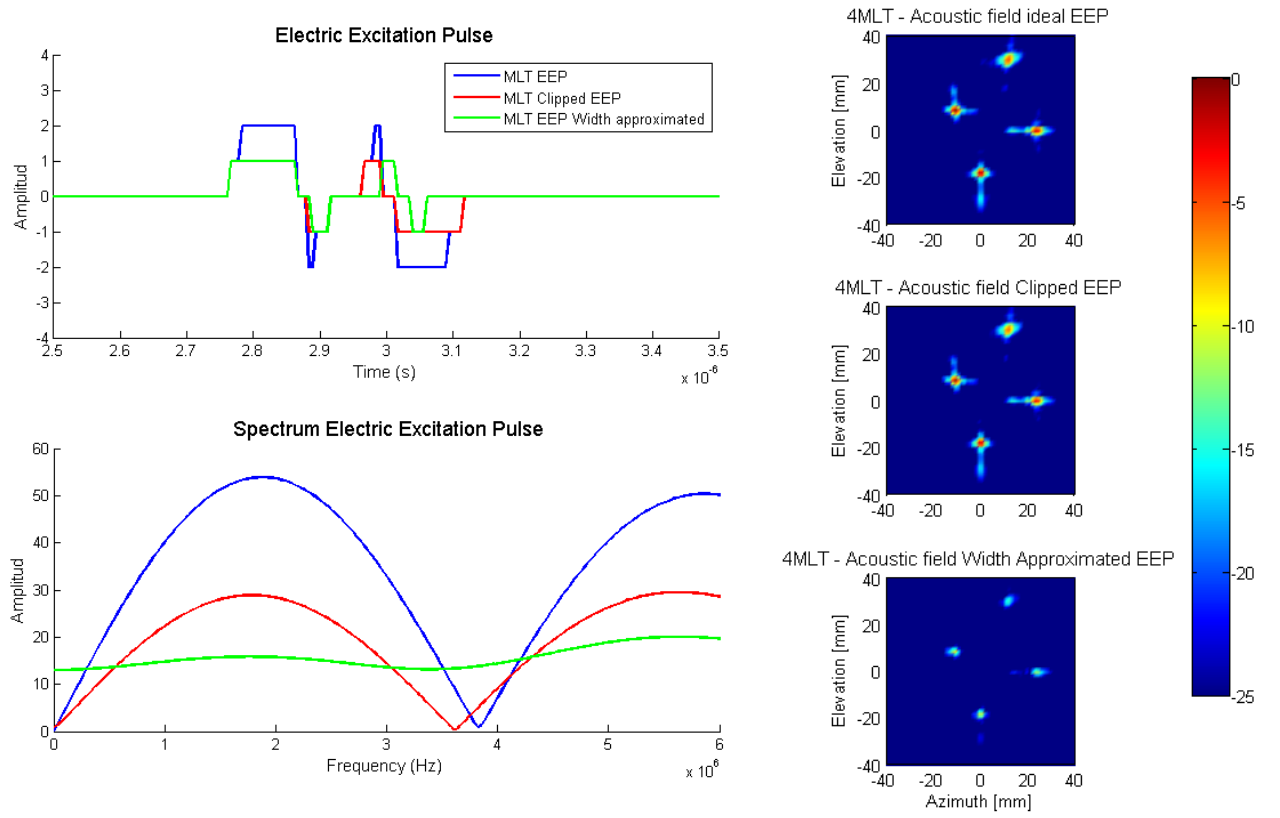

(a) (b)

Fig. 4.5. (a) Example of the different electric excitation pulses (EEP) applied on a central element for a 4MLT system at a given transmit event. Above, in the time domain, below, in the frequency domain. The ideal super imposed MLT-EEP, MLT-EEP-Clipped and MLT-EEP-Approximated are represented in blue, red and green, respectively; (b) Pressure field of a 4MLT system on a plane parallel to the transducer surface, generated using (from top to down) the ideal, clipped and approximated EPP.

Even though our -30dB cross-talk threshold was determined empirically based on our prior 2D work, experimental validation of configurations that were considered adequate based on this criterion demonstrated that they can indeed provide adequate recordings of acceptable image quality with only a slight loss in CNR but without obvious cross-talk artefacts. Of course, the estimated metric to express cross-talk levels does not take the exact spatial distribution of the cross talk into account. As such, experimental validation in a realistic clinical setting remains critically important. Nevertheless, the proposed metric and threshold can give a first indication whether a given imaging setup is likely to perform well.

Although the CNR values were very similar between the three imaging strategies, qualitative evaluation of the images demonstrated some differences. This apparent discrepancy was due to the nature of equation 4.1, where despite the magnitude difference between the components, the ratio remained similar. For a better understanding of the CNR results, the values for each component of equation 4.1 are presented in table 4.I.

On the other hand, the -30dB cross-talk energy level cut-off was directly extrapolated from the 2D findings and remains to be proven in volumetric *in-vivo* acquisitions, although the preliminary *in-vitro* results suggest that it is a valid measurement. Nevertheless, this study shows the feasibility of MLT for 3D volumetric scanning.

Given that this preliminary *in-vitro* validation has proven the capability of 3D MLT systems to generate adequate image quality volumes, an in-vivo validation of these systems is required in order to evaluate its capability to record dynamic conditions. For this, a solution to implement the super imposed EEPs related to the MLT sequences using tri-state pulser was investigated. As a result,

from the EEPs approximated approaches, it was found that the clipped EEPs resembles better the ideal MLT sequence, despite the drop of the transmit energy which might reduce the capability of the acoustic wave to propagate in depth and might decrease the acoustic pressure. Hence, the implementation of clipped MLT sequences for *in-vivo* acquisitions remains the topic of future work.

4.5 Conclusion

The 9MLT-4MLA and 16MLT-4MLA systems showed an acceptable performance during a preliminary *in-vitro* acquisition for volumetric imaging despite an expected drop in image quality. To further demonstrate the feasibility of this setup, an *in-vivo* validation using clipped EEPs of these results is required and remains the topic of future work.

5 Anatomical beamforming for volumetric cardiac motion estimation at a high temporal resolution

Part of this work was published in: A. Ortega, J. Pedrosa, B. Heyde, L. Tong, and J. D'hooge, "An automatic method for determining the anatomical relevant space for fast volumetric," *IEEE Ultrason. Symp*. Proc., pp. 0–3, 2015.

The complete study has been accepted for publication in: A. Ortega, J. Pedrosa, B. Heyde, L. Tong, and J. D'hooge, "Anatomical beamforming for volumetric cardiac motion estimation at a high temporal resolution," *Applied Sciences, Revision submitted for publication.*

Abstract
Fast volumetric cardiac imaging requires reducing the number of transmit events within a single volume. One way of achieving this is by limiting the field-of-view (FOV) of the recording to the myocardium when investigating cardiac mechanics. Although fully automatic solutions towards myocardial segmentation exist, translating that information in a fast ultrasound scan sequence is not trivial. In particular, multi-line transmit (MLT) scan sequences were investigated given their proven capability to increase frame rate (FR) while preserving image quality. The aim of this study was therefore to develop a methodology to automatically identify the anatomically relevant conically-shaped FOV, and to translate this to the best associated MLT sequence to scan this FOV. This approach was tested on 27 datasets leading to a conical scan with a mean opening angle of 19.7±8.5° while the mean 'thickness' of the cone was 19±3.4°. To subsequently scan this conical volume, several MLT setups were tested. The method of choice was the 10MLT sequence as it resulted in the highest frame rate gain while maintaining an acceptable cross-talk level. When combining this MLT scan sequence with at least 4 parallel receive beams, a total frame rate gain with a factor of approximately 80 could be obtained. As such, anatomical scan sequences can increase frame rate significantly while maintaining information of the relevant structures for functional myocardial imaging.

5.1 Introduction

Over the last decades, volumetric cardiac ultrasound imaging has gained momentum as the modality of choice to assess cardiac morphology and visualize global heart motion [8]. Recently, 3D cardiac ultrasound has also been used to quantitatively assess regional cardiac dynamics and several commercial products for 3D speckle tracking are now readily available [48]. One of the challenges for 3D motion estimation remains the relatively low image quality of the volumetric ultrasound data set. Particularly, its relatively low spatiotemporal resolution is of concern. Indeed, state-of-the-art commercial systems make use of a combination of several techniques in order to improve frame rate while maintaining image quality, such as limiting the field-of-view (FOV) [41], decreasing the line density [42], using ECG gating [14], and/or applying parallel receive beamforming (i.e. multi-line acquisition, MLA) [25]. This typically results in a frame rate of up to ~30Hz when scanning with a moderate line density, when using a representative wide angle field-of-view and when gating is performed over 4-6 cardiac cycles. The latter technique not only lengthens the acquisition but can also induce artefacts due to arrhythmias, breathing, motion or incorrect gating.

Recently, two other solutions have been proposed to increase the temporal resolution of the 3D systems. On the one hand, Diverging Wave Imaging has been introduced which uses a sparse virtual array located behind the probe [16]. This allows volumetric imaging at very high rates since the line density is only restricted by the reconstruction time. However, the use of unfocused beams implies that the energy of the beam is spread over a wider area resulting in low pressures which do not allow for harmonic imaging. In addition, the overall signal-to-noise ratio drops having a negative impact on motion estimators (as illustrated by the Cramer-Rao Lower Bound [17]).

On the other hand, multi-line transmit beamforming (MLT) has been proposed to increase temporal resolution by simultaneously transmitting multiple focused beams allowing harmonic imaging [19]. While its frame rate gain is more limited than that of diverging wave imaging [16] and although potential artifacts such as cross-talk might be introduced due to the interaction between neighboring MLT beams, it preserves image quality [21] and is an attractive imaging approach. Indeed, it has recently been demonstrated that cross-talk artifacts can be suppressed by using proper apodization [20], by avoiding the main directions of the transducer [45], by frequency-coding the different MLT beams [49] [50], and/or by physically separating the beams in space [23]. Furthermore, MLT can easily be combined with MLA to further increase the temporal resolution. More precisely, the width

of the transmit beams can be customized based on the desired amount of receive parallelization for each transmit beam. Based on equation 10 of [15], at least 4MLA (two in azimuth and two in elevation) can be reconstructed per focused beam in 3D for a typical cardiac 2D matrix array transducer. In order to allow a higher number of MLA, broader beams can be transmitted by reducing the transmit aperture. It should also be noted that safety issues due to the acoustic superposition of the MLT beams in the near field is of little concern. Indeed, we recently demonstrated that by small modifications of the transmit beamforming (i.e. introducing small delays or phase shifts between different MLT beams), the near field pressure can be adjusted to remain within safety regulations [43]. Finally, in order to test the feasibility of MLT for volumetric imaging a qualitative [23] and a quantitative [46] study were recently performed where the 2D findings were extrapolated to 3D. It was shown, by in-silico and in-vitro experiments, that a 16MLT-4MLA with transmit and receive apodization (Tukey α=0.5) generates volumetric images within a single heartbeat with an appropriate image quality for functional myocardial imaging [46].

Despite these fast imaging solutions, it is important to note that the typical volumetric ultrasound recording remains pyramidal, implying that a significant portion of the reconstructed image lines are not relevant to analyze 3D myocardial dynamics. Therefore, a straightforward way to reduce the number of transmit events is by limiting the FOV to the anatomically relevant space only, i.e. to a conically shaped volume, which captures the myocardium throughout the cardiac cycle. This reduced FOV can then be combined with the aforementioned parallelized scan sequences in order to further increase frame rate.

Although fully automatic solutions towards myocardial segmentation exist, translating that information in a fast ultrasound scan sequence is not trivial. The aim of this study was therefore to (1) develop a methodology to automatically define the characteristics of the conically shaped FOV given a segmented myocardial volume and (2) to set up an appropriat5.2e MLT scan sequence to scan the associated FOV as fast as possible.

5.3 Methods

5.3.1 Anatomical Relevant Space

The relevant FOV for functional myocardial imaging can be defined from a 3D dataset as follows:

Automatic real-time segmentation of myocardial boundaries
A fully automatic real-time segmentation of the left ventricular myocardium in a volumetric ultrasound recording was performed using the B-spline Explicit Active Surfaces (BEAS) framework [51][52]. More specifically, BEAS uses two explicit functions, one to represent the endocardial surface and another to represent the myocardial thickness. This allows to fully characterize the endo- and epicardial surfaces. These surfaces can then be used to define a binary mask identifying voxels belonging to the myocardium only. Fig.5.1(a) shows an example of such mask in 3 orthogonal slices through the middle of the ultrasound volume for a patient with suspicion of cardiac ischemia.

Coverage function
Using these binary images, a '*coverage function*' was defined as follows. First, based on the ray tracing principle, the path of a given scanline within the volumetric image volume can be traced. The pixels belonging to that scanline are compared with the binary mask in order to compute the percentage of pixels of the given scanline belonging to the myocardium. Finally, this procedure is repeated for all scan lines in the original pyramidal volume leading to a 'coverage function' as

illustrated in Fig. 5.1(b). As expected, the lines crossing the ventricular walls have the highest percentage of coverage while the ones crossing the apex have the lowest (i.e. Fig. 5.1(b)).

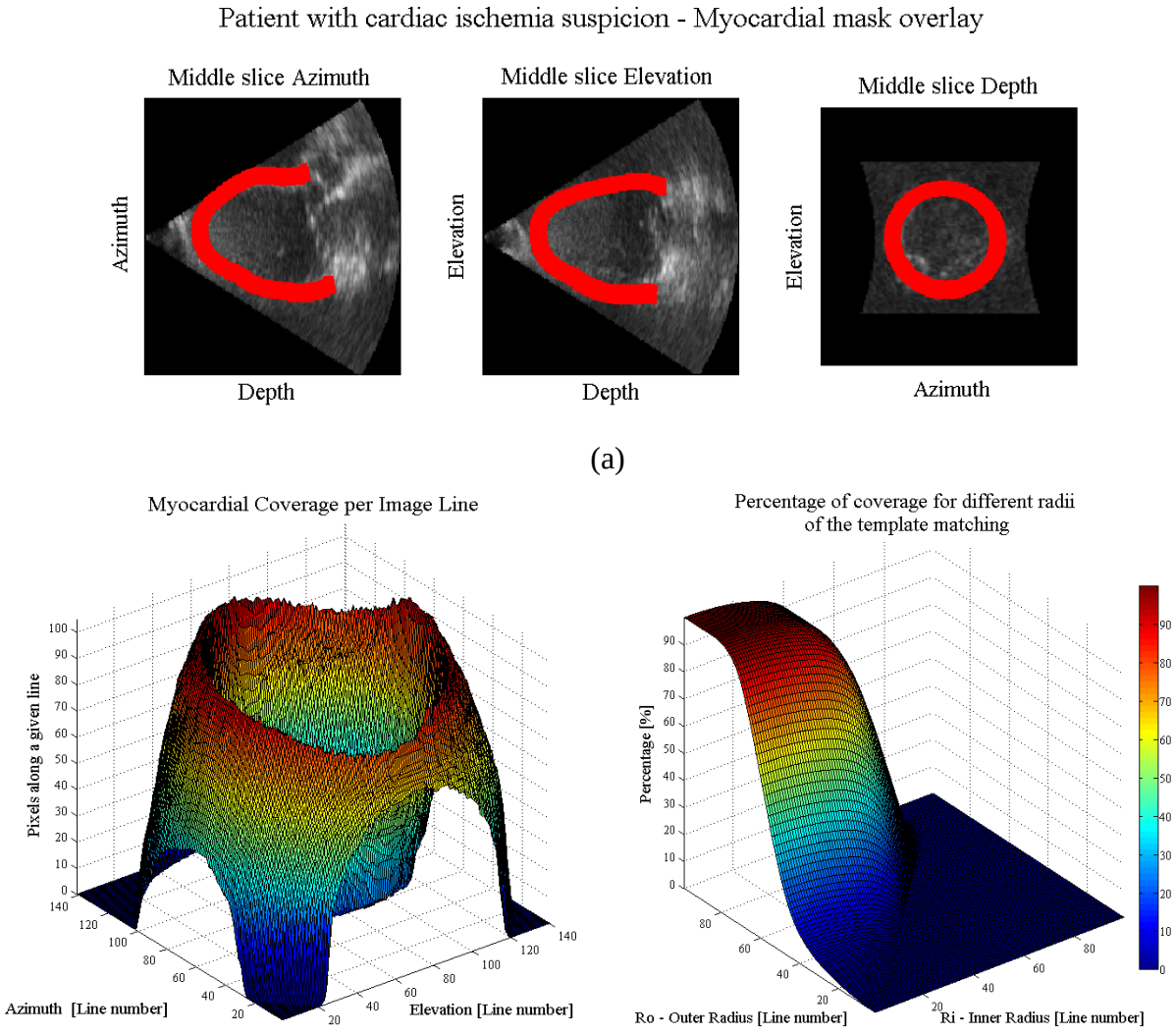

Fig. 5.1. Example of the workflow to determine the anatomical relevant space for a patient with cardiac ischemia suspicion: (a) Myocardial segmentation shown as a mask overlaid in three orthogonal slices through the middle of the ultrasound volume(from left to right: azimuth, elevation and depth); (b) Computed coverage function expressing the percentage of pixels along each image line that belong to the myocardium; (c) Percentage of myocardial coverage as a function of the inner radius (Ri) and the outer radius (Ro) of the ring-shaped template matching.

Ring-shaped template matching

To find a spatially continuous FOV that covers a given percentage of the total amount of myocardium (i.e. defined as 'T'), a ring-shaped template matching was used. This shape was chosen as an approximation of the left ventricular geometry when looking down from the apex, i.e. when the transducer is placed in an apical position. In 3D, this FOV therefore defines a cone. We express the amount of myocardial coverage T as a function of the inner radius of the ring template (R_i) and its thickness (ΔR), as illustrated in Fig. 5.2. As shown in Fig. 5.1(c), the smaller the inner radius and the bigger the outer radius the higher the total myocardial coverage. In order to effectively gain frame rate, a compromise has to be made between the amount of myocardial coverage, i.e. T, and the extent of the FOV. From all R_i and ΔR combinations that provide T myocardial coverage, the one with minimal ΔR was chosen as this would keep the volume to be scanned minimal. In this way, it is ensured that the desired T coverage is obtained using the least amount of lines possible (i.e. at the highest frame rate). In turn, these radii are used to determine the parameters (opening angle and thickness) for a conical scan, as represented in Fig. 5.3.

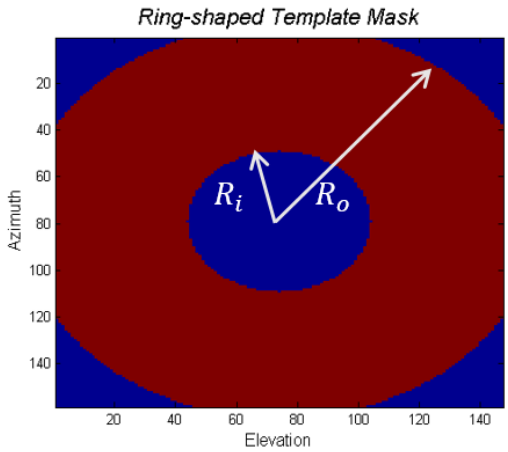

Fig. 5.2. Scheme of a ring-shaped template matching used to find the continuous region of the coverage function with a '*T*' percentage of the myocardium.

5.3.2 Parallelized Scan Sequence

In order to find the best scan sequence for a given FOV, the cross-talk energy level of several MLT setups can be quantified by computer simulation. In particular, a 2D square phased array transducer (10x10mm^2, 32x32 elements, 312.5µm pitch) transmitting a Gaussian pulse with a central frequency of 2.5MHz and 50% bandwidth was simulated using a GPU-based implementation of the spatial impulse response method (Simpulse) [44]. The transmit beams were focused at a depth of 60mm while dynamic focusing was used during receive. Tukey apodization (α=0.5) was applied in both transmit and receive to suppress cross-talk artifacts. The cross-talk energy level of the MLT systems can be determined using the process described in [46]. As such, simulations of the two-way beam profiles were performed on a plane parallel to the transducer surface (i.e. C-plane) at a depth of 65mm (i.e. around halfway the common imaging depth for cardiac applications). This depth was chosen based on our previous in-silico findings [46] while using the exact same system configuration. It was shown that the best performing system at this depth was also the system of choice at other depths and steering angles. In this study, we therefore focused on evaluating the systems' performance at this depth only.

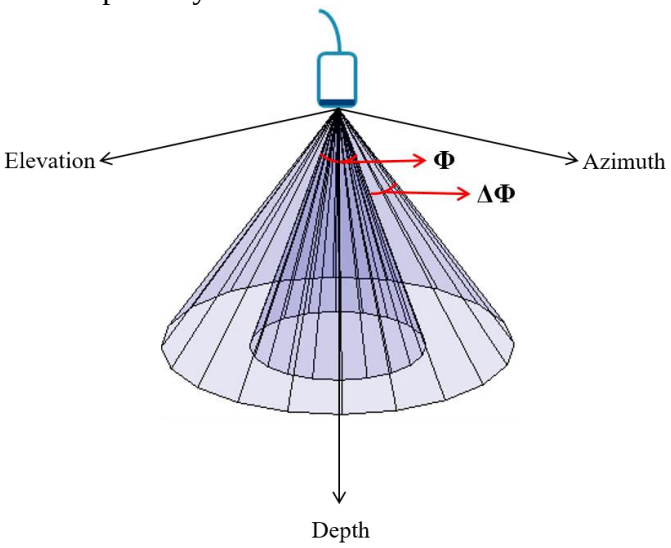

Fig. 5.3. Graphical representation of a conical scan for anatomical imaging, where Φ and ΔΦ represent the opening angle and thickness of the cone respectively.

To quantify how the energy of a beam spreads in the volume and potentially interferes with other MLT beams, the same procedure as in [46] was followed. In short, a beam was transmitted into one of the MLT directions (θ_i) and subsequently received along each of the MLT beam directions (including the same transmit direction - $\theta_{1\ldots i\ldots j}$). Next, the sum of the energy while transmitting and

receiving in the same MLT direction was considered as SLT energy (i.e. the ideal situation), whereas cross-talk was computed as the sum of the energy that deviates from the transmit beam towards the other remaining MLT directions, i.e. when transmitting in a given MLT direction but receiving in one of the other remaining MLT directions. This procedure was repeated for every MLT beam in the setup. The final cross-talk energy level (E_{xtalk}) was quantified in decibels. Mathematically, this can be expressed as:

$$E_{xtalk} = 10 * log10\left(\frac{\sum_{i=1}^{\#mlt}\sum_{j=1,j\neq i}^{\#mlt} E^{\theta ij}}{\sum_{i=1}^{\#mlt} E^{\theta ii}}\right), \tag{5.1}$$

where: i, is a given MLT direction being assessed; j, is a MLT direction different from the direction being tested (i); $\#mlt$, is the total number of MLT beams in the system; $E^{\theta ij}$, is the energy in the C-plane when transmitting in a given MLT direction i and receiving in one of the other direction (j) (i.e. cross-talk); and $E^{\theta ii}$, is the energy in the C-plane when transmitting in a given MLT direction i while receiving in the same direction i (i.e. SLT energy).

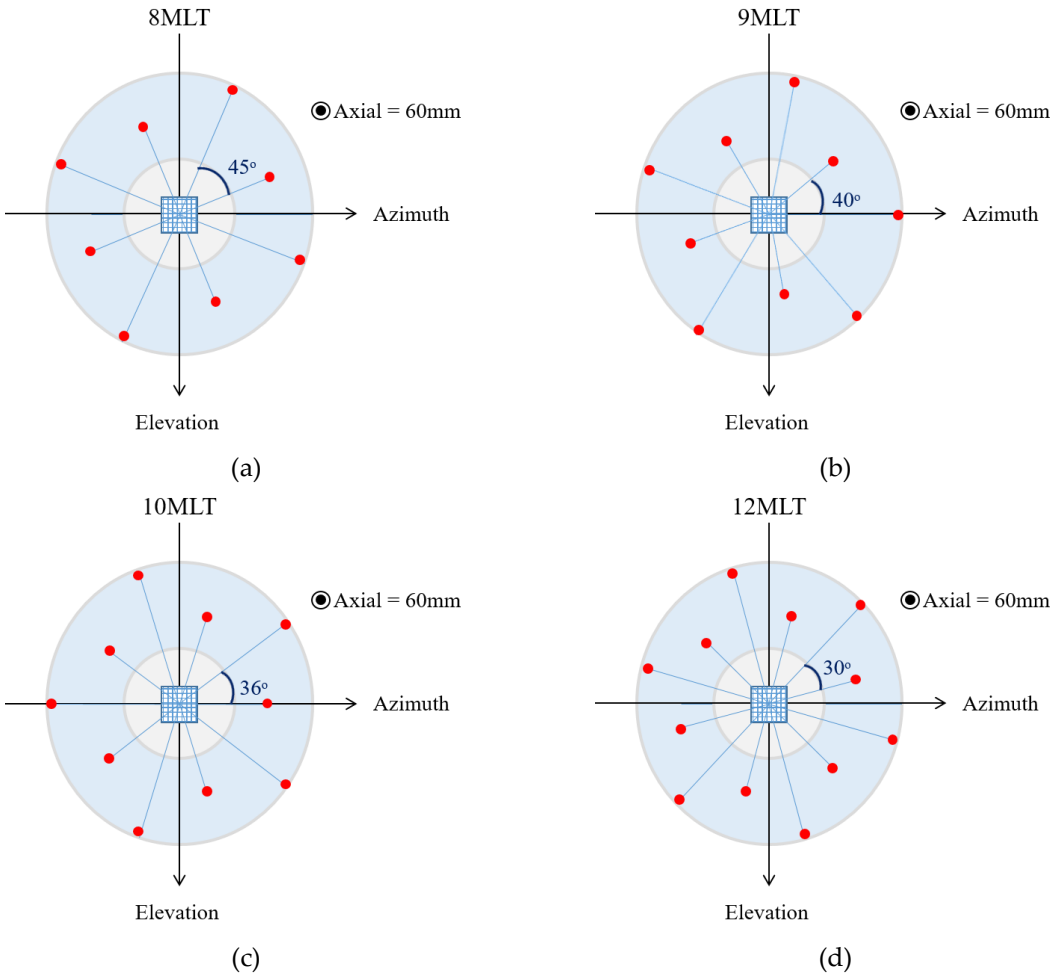

Fig. 5.4. View of the tested MLT systems looked from a C-plane at 60mm with respect to the rectangular aperture (central blue square). The MLT beams are spread out in an equiangular manner in the circumferential direction of the cone while steered in the -radial direction. In this way, the beams are as far apart as possible and therefore the inter-beam interference is reduced.

5.4 Experiments

To test this approach, 27 volumetric ultrasound datasets were randomly selected from the DOPPLER-CIP database (a large multi-center clinical FP7-funded study), which targeted patients suspected of (chronic) ischemia [13]. The mean opening angle for the volumetric scans in azimuth and elevation was 53.5°, resulting in approximately 7282 scanlines. The data was acquired using a GE E9 scanner (GE Vingmed, Horten, Norway) equipped with a 4V transducer. A coverage threshold *T* of 85% was chosen.

After finding the anatomical relevant space, MLT beams were equally spread circumferentially around the cone, and were staggered in the radial direction between neighboring beams to increase the inter-beam spacing and therefore to reduce cross-talk [23]. In particular, four systems were investigated: 8MLT, 9MLT, 10MLT and 12MLT as illustrated in Fig. 5.4. The cross-talk energy level of the systems was quantified using equation (5.1), and a threshold of -30dB was defined to give acceptable B-mode SNR. Although this pre-defined cut-off was arbitrarily chosen from a retrospective analysis of our 2D *in-silico* and *in-vivo* findings, 3D *in-vitro* experiments have nevertheless corroborated that this is a suitable measurement, even maybe a bit too restrictive, to ensure an adequate image quality [46].

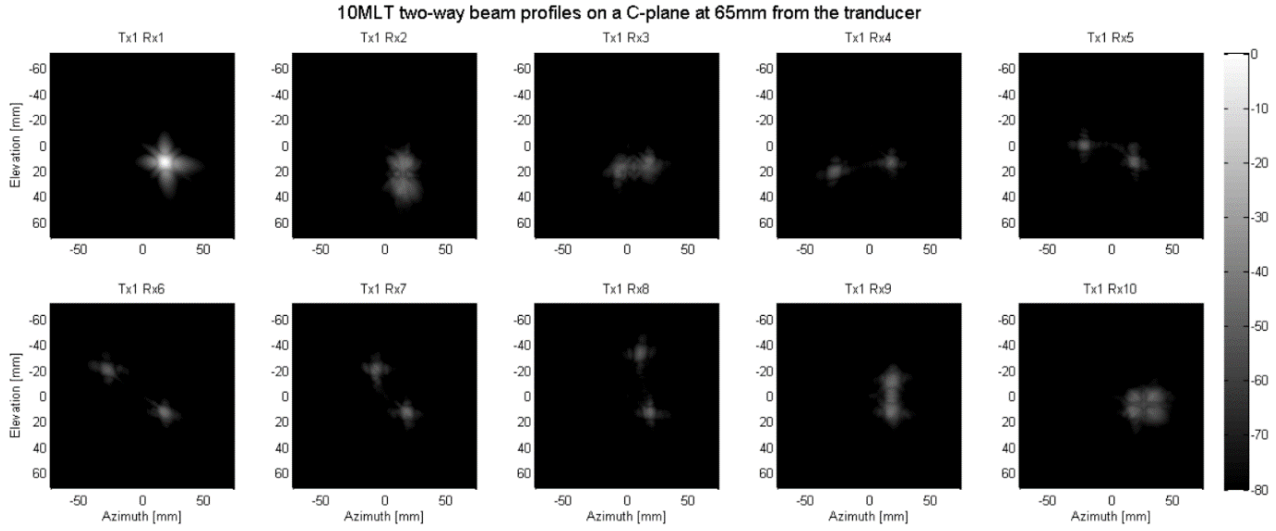

Fig. 5.5. Two-way beam profiles of a 10MLT system on a C-plane at 65mm, when transmitting at one direction (i.e. θ_i) and receiving in all other MLT directions (i.e.θ_1,..θ_i,..θ_j). Tukey apodization ($\alpha = 0.5$) was used in transmit and receive. The first subplot can be seen as the single line transmit signal, and the remaining ones as noise (i.e. cross-talk).

5.5 Results

For all datasets tested, the mean opening angle (Φ) for the conical scan was 19.7±8.5° while the mean 'thickness' of the cone ($d\Phi$) was 19±3.4°. Therefore, a reduction of 49% in the number of transmit events was achieved, approximately doubling the frame rate.

Given this estimated 'mean' conical FOV, the cross-talk energy level of all the MLT setups was calculated. Fig. 5.5 shows an example of the two-way beam profiles in a C-plane used to calculate the inter-beam interference of a 10MLT system, where a beam was transmitted in one direction and received in each of the MLT directions. The cross-talk energy levels of the tested systems are presented in Fig. 5.6. As can be noted, the 8MLT and 9MLT systems reached the pre-defined

threshold of -30dB, while the 10MLT was only half a dB above. The 12MLT system on the other hand was about 4dB above the cut-off.

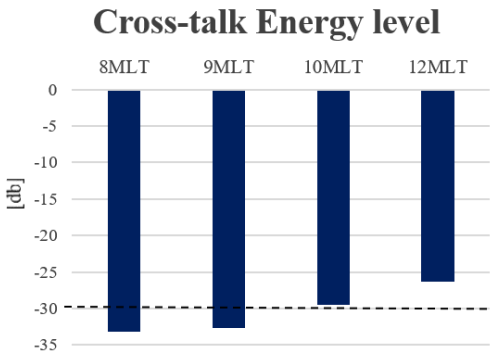

Fig. 5.6. Cross-talk energy level of the different tested setups for the estimated 'mean' conical FOV. The tested systems were: 8MLT, 9MLT, 10MLT, and 12MLT, all with transmit/receive Tukey apodization (α= 0.5). The cross-talk cut-off was defined as -30dB for an acceptable B-mode image quality.

5.6 Discussion

In this study, a methodology to find the anatomical relevant space for functional myocardial imaging has been described. This method was used to compute the parameters for a conical scan and to find an optimal MLT scan sequence to further speed up the acquisition process. In particular, an average opening angle of 19.7° and a mean thickness of 19° for the conical scan were found. Clearly, these values depend on the threshold '*T*' defining the amount of myocardial coverage that should be retained. This value was arbitrary set to 85% in this study but could be modified as required. Nevertheless, this arbitrary threshold allowed to provide initial insight in the characteristics of the conical FOV to be encountered in a clinical setting. It should be mentioned that the ring-shape template matching used to determine the opening angles of the conical volume might not be ideal given the left ventricular geometry. As such, an elliptic template might be more adequate but as this also complicates the MLT setup, this extension remains to be investigated in future work and was considered outside the scope of this initial feasibility study on anatomical volumetric imaging.

Given the characteristics of the typical conical volumes to be encountered in a clinical setting, the 8MLT, 9MLT and 10MLT system seemed to be able to generate high frame rate images while preserving an appropriate image quality as these implementations reached our predefined threshold of -30dB cross-talk. Even though this threshold was at first chosen from retrospectively analyzing our MLT findings in 2D [21], our recent 3D *in-vitro* experiments corroborated that this threshold is indeed a reliable proxy for good image quality [46]. In fact, very recently Ramalli et. al. [54] demonstrated both *in-vitro* an *in-vivo* that a 12MLT system can generate 2D images of clinically diagnostic value while this system had inter-beam cross-talk levels well above our pre-defined -30dB threshold [20]. As such, our -30dB threshold was likely conservative implying that also the 12MLT system tested in the context of anatomical imaging remains an attractive option that should be evaluated experimentally.

Overall, the combination of MLT and the definition of an anatomic FOV would thus imply a gain in frame rate up to 24 (considering 12MLT an option). As it has previously been proposed that at least 4MLA (2 in azimuth and 2 in elevation) can be reconstructed per focused beam for a typical 2D cardiac matrix array transducer [15], this implies that the proposed sequences could effectively gain a factor up to 96 in frame rate at full line density. Similarly, if an MLT-4MLA sequence is implemented an actual frame rate gain factor of 64, 72 and 80 could be obtained when using 8, 9 and

10 MLT beams respectively. Finally, in order to further improve the temporal resolution of the data set, line density and/or interpolating the received scanline data could be considered.

Nevertheless, depending on the desired application, frame rates in the order of hundreds or even thousands of Hertz could be achieved if a sparse anatomical scan sequence is implemented. For example, assuming an 18-segment left ventricular (LV) model, only 6 segments are defined around the circumference of the left ventricle (as illustrated in Fig. 5.7). As such, as little as 6 beams would be required to scan the left ventricle with a clinically relevant spatial sampling. Thus, using MLT beamforming, a single transmit event could evaluate all LV segments defined this way at a volume rate of 5kHz. However, 6 beams around the left ventricular myocardium may be too few to correctly resolve cardiac kinematics. As a consequence, a trade-off between the frame rate and the spatial sampling of the volume has to be made. For instance, if the12MLT-4MLA sequence is applied to scan the FOV, 48 image lines could be reconstructed per transmit event. If 5 transmit events are then performed, 240 samples around the circumference could be acquired at a frame rate of 1kHz. Depending on the application the transmit events could be performed radially or circumferentially, while properly staggering the scanning sequence should ensure that the inter-beam distance remains constant. Although such sequence would result in inhomogeneous spatial sampling (i.e. transmit beam are further apart than MLA beams), the MLA beams could be used to assess local kinematics (e.g. 3D motion) while the MLT beams allows sampling different segments of the LV simultaneously.

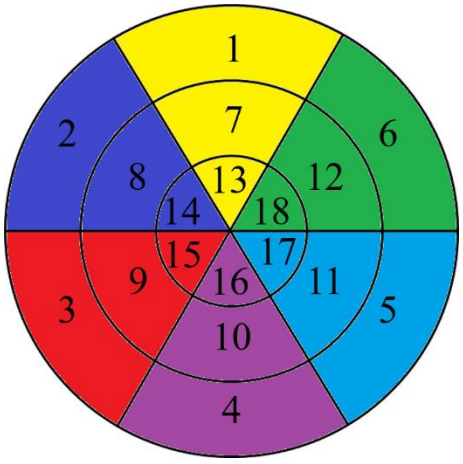

Fig. 5.7. Illustration of the subdivision of the18 segment cardiac model into 6 sectors (each of them represented with a different color), for a sparse scanning sequence to achieve ultra-high frame rates.

In order to translate the proposed scan sequence to the clinical setting, several approaches could be envisioned. For example, one could consider a fixed conical volume based on a statistical analysis of what is likely to be encountered in a clinical setting, and define an optimal MLT sequence for this volume as described in the present study. However, given the large variability of ventricular size and shape, a fairly large FOV would be required implying that only a relatively moderate increase in frame rate would be achieved.

A better alternative would be to ask the user to first identify the FOV in the pyramidal volume acquired using conventional imaging. This FOV could then be used to set up the fast MLT imaging sequence. Nevertheless, this manually delineated FOV adapted to the patients' anatomy would still remain relatively large to ensure the myocardium to remain inside during the full cardiac cycle. Evidently, as there is a time lag between finding the FOV and defining the imaging scan sequence, the latter would not have to be done in real-time (but sufficiently fast) and different MLT setups could prospectively be linked to characteristic dimensions of the conical volume in a look-up-table (LUT).

Finally, a third - and preferred alternative - would be to use a dynamic FOV definition based on a fully automatic 3D ultrasound myocardial segmentation. These technologies are already available, e.g. ([55],[56]). This would lead to an optimal, narrow FOV, and thus an optimal frame rate gain. Given the simplicity of defining the proposed coverage function (whose calculation can be parallelized in a straightforward manner), and given the possibility of real-time template matching [57], the anatomical FOV could be dynamically defined. Then, the best fitting parallelized scan sequence can be looked-up in a LUT which could – similar to the LUT used in the manual FOV definition - prospectively be defined for a set of predefined dynamics FOVs. Of note in this context is that MLT beamforming has recently been demonstrated to be possible in real-time [54] and does not require off-line image reconstruction.

Thus, the ideal work flow for anatomical cardiac imaging could be envisioned as:

i) A pyramidal volume is acquired at a conventional frame rate (i.e. ~30 Hz).
ii) Using any existing automatic real-time segmentation framework (e.g. BEAS [55] or real-time contour tracking library – RCTL [56]), the left-ventricular myocardium is detected.
iii) The coverage function and the ring-shaped template matching are applied to define an anatomical conically shaped FOV.
iv) Based on (iii), a fast scanning sequence is automatically selected using a LUT giving the best combination of transmit and receive parallelization (i.e. MLT-MLA) to scan the detected region-of-interest.
v) The anatomical relevant space is scanned at high spatiotemporal resolution for subsequent motion analysis.

5.7 Conclusions

Anatomical scanning in combination with MLT-MLA beamforming techniques can increase frame rate significantly while keeping information of the relevant structures for functional myocardial imaging. When limiting the FOV to a cone, a frame rate gain factor of about 2 could be achieved. Furthermore, when combined with parallel transmit/receive beamforming and transmit/receive apodization (Tukey - $\alpha = 0.5$), frame rate could be further increased with a 64-fold, 72-fold or 80-fold factor in case of a 8MLT-4MLA, 9MLT-4MLA or 10MLT-4MLA configuration respectively, while showing acceptable cross-talk levels. Although the tested 12MLT-4MLA configuration, with the same apodization, did not reach the predefined cross-talk limit, its 96-fold frame rate gain might outweigh its loss in image quality. It therefore remains a possible implementation to be investigated in future in-vivo and/or in-vitro experiments.

6 General conclusions and future perspectives

Given the ever-growing incidence of cardiovascular diseases (which are already the number one cause of death globally), there is a great necessity to develop tools that allow the early detection, management and follow-up of these pathologies non-invasively. Hereto, ultrasound imaging is the modality of choice as it offers several advantages over other imaging techniques. Although 2D US imaging is a well-stablished imaging modality for routine cardiac diagnosis, 3D US imaging provides several benefits when assessing cardiac function. This explains the increasing clinical interest in volumetric US. Among these benefits are the more intuitive interpretation of the resulting images due to the 3D nature of the heart, and – more importantly – the possibility to avoid making geometric assumptions on the shape of the cardiac chamber when estimating its volume. However, despite efforts, 3D US systems still suffer from relatively poor spatio-temporal resolution despite acquiring image information over multiple heart beats using ECG gating. Image resolution as well as contrast is therefore lower than what is available in 2D echocardiography. In addition, due to the relative low volume rates, not all cardiac events are resolved since some of them last for only a few (tens of) milliseconds. Furthermore, this lower spatiotemporal resolution affects the performance of advanced image processing algorithms to determine motion and deformation of the heart since they rely strongly on the image quality of the volumetric datasets [58]. Therefore, to improve the evaluation of cardiac function, higher spatiotemporal resolution is required while preserving overall image quality, i.e. contrast.

Increasing frame rate implies a reduction of the number of transmit events within a single volume. To achieve this, several methods have been proposed, and are summarized in table 6.I.

In addition, very recently, a hybrid solution to increase frame rate and preserve image quality has been proposed, i.e, Multi-Plane- Transmit Beamforming [59]. This method exploits the benefits of the high temporal resolution of the DW and the preserved spatial resolution of the MLT. Hereto, multiple planar (i.e., 2-D) diverging waves are simultaneously transmitted in order to scan the 3-D volume. The approach was shown to be feasible and its performance was demonstrated competitive to state-of- the-art methodologies (i.e. 3D DW and 3D MLT). However, further improvements through *in-vitro* and *in-vivo* experiments need to be carry out.

The main contribution of this thesis has therefore been the development of advanced parallelized beamforming techniques that allow an adequate trade-off between the frame rate and image quality of an imaging system.

6.1 Main contributions

The major contributions and strengths of this work can be summarized as follows:

Deduction of a new analytical expression for fast calculation of the impulse response function (IR), which speeds up the calculation time by almost 4 times, while remaining perfectly accurate. The IR is a commonly used approach to simulate linear ultrasound fields and pulse-echo signals, which are essential for the development of 3D US systems. The

speed up was achieved by a geometric efficient expression combined with an analytic low-pass filter to avoid the use of high sampling frequencies. This new expression is particularly relevant for 2D matrix transducer design where computational times remain currently a bottle neck in the design process, jeopardizing the progress of 3D US imaging systems.

Evaluation of different transmit and receive parallelization systems for fast volumetric cardiac imaging. For the first time, the trade-off between the amount of transmit and receive parallelization and the image quality (measured as the amount of cross-talk artifacts of the system) for 3D US imaging was quantified. The effect of apodization was also studied. This was investigated by an extensive computer simulation. The cross-talk energy level of the systems was quantified at different depths and at different steering directions in order to evaluate their performance in the entire volume. As a result, it was found that 4MLT-16MLA without apodization, and 9MLT-4MLA and 16MLT-4MLA with apodization, are able to produce acceptable image quality volumes, while increasing frame rate by a factor of 64, 36 and 64, respectively resulting in volume rates adequate for strain analysis without requiring stitching several sub-volumes, taken over multiple heart beats.

A preliminary *in-vitro* validation of the 3D MLT sequences was performed in order to corroborate the *in-silico* findings. Due to the complexity of the electric excitation pulses (EEPs) for MLT implementations, the parallelized volumes were generated synthetically by combining the respective channel data off-line from a line-by-line acquisition. Thus, from the *in-silico* findings the best and the 'worst' systems were investigated (i.e., 9MLT-4MLA and a 16MLT-4MLA). It was shown that both systems, despite the expected drop in image quality, are able to produce volumetric images with limited cross-talk artifacts while preserving a contrast-to-noise ratio comparable to that of a SLT-SLA system. However, although this validation proves the capability of 3D MLT systems to generate adequate image quality volumes, an *in-vivo* study is still required. Therefore, an investigation of the ideal hardware implementation of MLT sequences was performed. From the electric excitation pulses modifications studied, it was found that clipping the superimposed EEPs resembles better the transmit pattern of a real MLT implementation. Hence, the implementation of clipped MLT sequences for *in-vivo* acquisitions remains the topic of future work.

Defining a protocol to automatically find the anatomical relevant space for functional myocardial imaging, and its best associated parallelized scanning sequence. The combination of these two approaches led to an anatomical scanning sequence with frame rates in the order of several hundreds of Hz as required to study all cardiac phases. A validation study was performed and the mean values for an anatomical scan where computed. It was found that a 10MLT-4MLA system would be the best suited scan sequence with a total frame rate gain factor of 80. Nevertheless, the 12MLT-4MLA system could be also considered since it provides a higher frame rate gain factor (of 96) despite of its more pronounced cross-talk energy level. To confirm these findings experimentally, a real-time implementation of a 3D automatic segmentation frame work should be implemented on the system, and the transmit of MLT sequences should be allowed.

Table 6.I Proposed methods to reduce the number of transmit events within a single volume

Method	Characteristics	Pro's	Contra's	Harmonic imaging	Artifacts
Reducing the FOV	Limits the Region of interest.	Preserves image quality.	Might leave anatomical structures un-sampled.	Yes	
Reducing line density	The less number of lines the higher the frame rate.	Preserves FOV.	The lower the line density, the lower the lateral resolution.	Yes	Might introduce artifacts due to aliasing
ECG- gating	The volume is divided in smaller independent sub-volumes, which can be scanned at high frame rates. The final image is the combination of the sub-volume images acquired over 4 to 6 heart cycles.	Preserves FOV and line density.	-Prolongs acquisition times. -It is not applicable in patients with atrial fibrillation or other forms of arrhythmias.	Yes	Stitching artifacts due to either probe or patient motion
MLA	Several receive lines are reconstructed from a single transmit beam. Typically, broad beams are used to insonify a wider area to allow a higher number of MLA beams.	Preserves FOV and line density, and is easily implemented in clinical scanners. Allows for very high frame rate.	Misalignment of the transmit and receive beams. Reduces SNR.	Yes	Block-like artifacts due to misalignment of the transmit and receive beams. Compounding might introduce Motion artifacts. However, algorithms to correct for this have been proposed.
MLA – Less-focused beams	The beams are broadened by reducing the transmit aperture.		Reduces the energy transmitted and limits penetration.	Depends on how much the transmit aperture is reduced.	
MLA – Unfocused beams	The beams are broadened by either plane wave (transmitting with the full aperture at once), or diverging waves (placing a virtual focal point behind the transducer). Allows for a massive amount of MLA beams.		The energy of the beam is spread over a wider area. Requires spatial coherent compounding to increase image quality, reducing its effective gain in frame rate.	No	

Method	Characteristics	Pro's	Contra's	Harmonic imaging	Artifacts
MLT	Several beams are transmitted simultaneously into different directions of the volume. The gain in frame rate factor is equal to the number of MLT beams.	Due to the emission of focused beams, the spatial resolution is mainly preserved.	Limited gain in frame rate.	Yes	Cross-talk artifacts due to the interaction of the parallel beams.
DW using sparse virtual array*	Several virtual sources are placed behind the transducer and fired sequentially. The resolution, contrast, SNR, frame rate, and the FOV can be easily adjusted based on the desired application.	Allows for very high frame rate but it is limited by the number of virtual sources (compounding).	Overall low SNR, having a negative impact on motion estimators.	No	Motion artifacts might be introduced.

*DW using sparse virtual array differs from MLA using Diverging Wave in that the earlier does compounding by means of sub-aperture imaging to increase spatial resolution. This implies that a bigger number of transmissions should be performed to preserve SNR. Therefore, MLA using diverging wave while transmitting with the full array might be better at increasing temporal resolution, at the expenses of image quality.

6.2 Final discussion and conclusion

Due to mainly hardware limitations, *in-vitro* and *in-vivo* experiments of a true MLT implementation could not be studied and therefore the capability of MLT-MLA systems to precisely record the motion of the heart could not be corroborated. Furthermore, although synthetic MLT seems to reflect the behavior of parallelized systems appropriately, there are some effects such as the electrical and/or thermal noise, and the implication of the use of tri-state pulsers that cannot easily be predicted or simulated.

Moreover, the protocol to find the relevant anatomical space for functional myocardial imaging might leave the apex un-sampled, implying that a typical bull's-eye representation cannot be reconstructed and that physicians have to learn to interpret the resulting image. Most likely, this is not a problem given the required training. In any case, the purpose of this approach is principally to provide a solid base for image processing algorithms to determine the functioning of the heart rather than providing images for visual reading.

To translate the proposed imaging methodologies to the clinical setting, two very important aspects should be considered:

1) Implementation of MLT sequences using second-harmonic imaging

   Echocardiography typically requires the use of second-harmonic imaging since it provides a significant image enhancement (especially in technically difficult patients). Harmonic waves are generated and built up in depth due to non-linear propagation of sound in tissue. It requires high transmit amplitude pressures as the ones emitted with narrow beams. Therefore, given that MLT imaging is mostly implemented using focused beams, these two techniques can easily be combined. In fact, it has already been shown that harmonic imaging can be used to reduce cross-talk artifacts in MLT systems [19].

   Within the time frame of this project we were unable to study the combination of these two techniques, nevertheless we could envision it as:

   i) Lengthening the electric excitation pulses. In this way, only the low-frequency of the bandwidth of the transducer is used in transmission
   ii) Filtering the acquired channel data around the second-harmonic frequency band instead of the transmitted band to obtain the scattered signal
   iii) Proceeding with conventional image reconstruction for MLT sequences

2) MLT scan sequences adapted to clinical 2D matrix array transducers

   As mentioned in Chapter 2, 2D array transducers are essential for volumetric imaging. However, matrix array transducers have between 2000 and 4000 individual elements which makes wiring costly and impractical. Several methods have been proposed to limit cabling between the US probe and the back-end of the console. Among these methods is *sub-aperture beamforming* (SAP) which is most commonly implemented in clinical scanners. SAP divides the transducer aperture in subsets of elements that are beamformed inside the probe and the resulting signal is transferred through a single wire. In this way, the number of wires required to connect the transducer and the back-end of the console are reduced to the number of 'sub-apertures'. Therefore, beamforming is typically done in two phases where

part of the beamforming is done in the transducer itself while the pre-beam formed signals are combined in the front-end in order to generate the individual image lines (i.e., two-stage beamforming [26]). Recently, it has been shown that severe imaging artifacts are introduced while using this technique for DWI [46]. This is due to delay errors which cause grating-lobes and reduced penetration. Thus, due to the complexity of MLT sequences, an adaptation for clinical transducers using SAP must be implemented, which represents a challenge that needs to be investigated.

Some of the potential clinical applications of fast 3D US cardiac imaging are in the fields of:

- Motion/Deformation imaging: Quantification and analysis of myocardial motion is of critical importance to assess cardiac function. Currently, myocardial motion/deformation can be quantified to some extent. However, enhanced acquisitions of the short-lived mechanical events may offer new information on pathophysiological mechanisms.

- Mechanical activation imaging: Mechanical activation of the myocardium is accompanied by brief (local) myocardial motion/deformation. The mechanical activation wave could be representative for the preceding electrical depolarization sequence, with obvious applications in electrophysiology.

- Viscoelastic properties of the myocardium *(shear waves propagation):* Propagation of shear waves through the myocardium gives information about its mechanical properties. For example, (local) stiffness or viscosity can be obtained.

- Doppler imaging: Can be used to simultaneously evaluate the velocities of the blood and the myocardium. Therefore, to study the blood-wall interaction.

As a conclusion, the beamforming techniques presented in this Ph.D. thesis might provide an important step forward in functional imaging of the cardiac muscle.

6.3 Future perspectives

The beamforming strategies here presented still have a long way to go before becoming available in clinical systems, therefore *in-vivo* validation of the methods presented should be carried out. But first, we have to make sure that the MLT sequences meet the safety regulations, which might imply that further modifications have to be introduced. Translation of these methods into commercial systems remains challenging, since this would not only require changing imaging methodology but also redesigning hardware.

Bibliography

[1] G. J. Tortora and B. H. Derrickson, “The cardiovascular system: The heart,” 12th ed., Wiley, Ed. 2009, pp. 547–570.

[2] K. Marieb and E. Hoehn, “The cardiovascular system: the heart,” in *Anatomy & physiology*, 3rd ed., P. I. Edition, Ed. 2008, pp. 595–624.

[3] A. Guyton and J. Hall, *Textbook of medical physiology*. Elsevier Saunders, 2006.

[4] P. Iaizzo, *Handbook of cardiac anatomy, physiology, and devices*. 2005.

[5] World Health Organization, “Chapter 1: Burden : mortality , morbidity and risk factors,” *Global Status Report on non-communicable diseases 2010*. pp. 9–31, 2011.

[6] T. Lobstein, L. a Baur, and R. Uauy, “Obesity in children and young people: A crisis in public health.,” *Obes. Rev.*, vol. 5 Suppl 1, pp. 4–104, 2004.

[7] WHO, “Childhood obesity,” *Int. J. Obes.*, vol. 23, no. s5, pp. 1–53, 2012.

[8] R. M. Lang, L. P. Badano, V. Mor-Avi, J. Afilalo, A. Armstrong, L. Ernande, F. A. Flachskampf, E. Foster, S. A. Goldstein, T. Kuznetsova, P. Lancellotti, D. Muraru, M. H. Picard, E. R. Rietzschel, L. Rudski, K. T. Spencer, W. Tsang, and J. U. Voigt, “Recommendations for cardiac chamber quantification by echocardiography in adults: An update from the American society of echocardiography and the European association of cardiovascular imaging,” *Eur. Heart J. Cardiovasc. Imaging*, vol. 16, no. 3, pp. 233–271, 2015.

[9] T. L. Szabo, *Diagnostic ultrasound imaging: inside out*, vol. 53, no. 9. 2004.

[10] P. Suetens, *Fundamentals of medical imaging*, 2nd ed. Cambridge, UK: Cambridge University Press, 2009.

[11] T. G. Leighton, *The Acoustic Bubble*. UK: Academic Press, 1994.

[12] L. Tong, *Novel beam forming methods for fast cardiac imaging using ultrasound*. 2013.

[13] J. N. Wright, “Image Formation in Diagnostic Utrasound,” *Short Course*, 1997.

[14] M. Pernot, K. Fujikura, S. D. Fung-Kee-Fung, and E. E. Konofagou, “ECG-gated, mechanical and electromechanical wave imaging of cardiovascular tissues in vivo.,” *Ultrasound Med. Biol.*, vol. 33, no. 7, pp. 1075–85, Jul. 2007.

[15] T. Hergum, T. Bjastad, K. Kristoffersen, and H. Torp, “Parallel Beamforming Using Synthetic Transmit Beams,” *IEEE Trans. Ultrason. Ferroelectr. Freq. Control*, vol. 54, no. 2, pp. 271–280, 2007.

[16] J. Provost, C. Papadacci, J. E. Arango, M. Imbault, M. Fink, J.-L. Gennisson, M. Tanter, and M. Pernot, “3D ultrafast ultrasound imaging in vivo.,” *Phys. Med. Biol.*, vol. 59, no. 19, pp. L1–L13, Oct. 2014.

[17] W. F. Walker and T. G. E., “A fundamental limit on the performance of correlation based phase correction and flow estimation techniques,” in *IEEE Ultrasonics Symposium Proceedings*, 2004.

[18] T. Shirasaka, “Ultrasonic Imaging Aparatus,” 4,815,043, 1989.

[19] F. Prieur, B. Dénarié, A. Austeng, and H. Torp, “Multi-Line Transmission in Medical Imaging Using the Second-Harmonic Signal,” *IEEE Trans. Ultrason. Ferroelectr. Freq. Control*, vol. 60, no. 12, pp. 2682–2692, 2013.

[20] L. Tong, H. Gao, and J. D’hooge, “Multi-transmit beam forming for fast cardiac imaging-a simulation study,” *Ultrason. Ferroelectr. Freq. Control. IEEE Trans.*, vol. 60, no. 8, pp. 1719–1731, 2013.

[21] L. Tong, A. Ramalli, R. Jasaityte, P. Tortoli, and J. D’hooge, “Multi-transmit beam forming for fast cardiac imaging--experimental validation and in vivo application.,” *IEEE Trans. Med. Imag.*, vol. 33, no. 6, pp. 1205–19, Jun. 2014.

[22] P. Santos, L. Tong, A. Ortega, L. Løvstakken, E. Samset, and J. D’hooge, “Safety of Multi-Line Transmit Beam Forming for Fast Cardiac Imaging – A Simulation Study,” *IEEE Ultrason. Symp. Proc.*, 2014.

[23] L. Tong, A. Ortega, H. Gao, and J. D’hooge, “Fast three-dimensional ultrasound cardiac imaging using multi-transmit beam forming: A simulation study,” *IEEE Ultrason. Symp. Proc.*, pp. 1456–1459, Jul. 2013.

[24] S. W. Smith, H. G. Pavy, and O. T. Von Ramm, “High-speed Ultrasound Volumetric Imaging System- Part I: Transducer Design and Beam Steering,” *IEEE Trans. ultrasound, Ferroelectr. Freq. Control*, vol. 38, pp. 100–108, 1991.

[25] D. P. Shattuck, M. D. Weinshenker, S. W. Smith, and O. T. von Ramm, “Explososcan: a parallel processing technique for high speed ultrasound imaging with linear phased arrays.,” *J. Acoust. Soc. Am.*, vol. 75, no. 4, pp. 1273–82, Apr. 1984.

[26] B. J. Savord, “Beamforming methods and apparatus for three-dimensional ultrasound imaging using two-dimensional transducer array,” 6,013,032, 2000.

[27] G. E. Tupholme, “Generation of acoustic pulses by baffled plane pistons,” *Mathematika*, vol. 16, no. 2, pp. 209–224, Feb. 1969.

[28] P. R. Stepanishen, “Transient Radiation from Pistons in an Infinite Planar Baffle,” *J. Acoust. Soc. Am.*, vol. 49,

no. February, pp. 1629–1638, 1970.
[29] G. R. Harris, “Review of transient field theory for a baffled planar piston,” *J. Acoust. Soc. Am.*, vol. 70, no. May 2013, pp. 10–20, 1981.
[30] J. C. Lockwood and J. G. Willette, “High-speed method for computing the exact solution for the pressure variations in the nearfield of a baffled piston,” *J. Acoust. Soc. Am.*, vol. 53, no. May 2013, pp. 735–741, 1972.
[31] J. A. Jensen, “Ultrasound fields from triangular apertures,” *J. Acoust. Soc. Am.*, vol. 100, no. 4, pp. 2049–2056, 1996.
[32] G. Scarano, N. Denisenko, M. Matteucci, and M. Pappalardo, “A new approach to the derivation of the impulse response of a rectangular piston,” *J. Acoust. Soc. Am.*, vol. 78, no. May 2013, pp. 1109–1113, 1985.
[33] W. A. Verhoef, M. J. T. M. Cloostermans, and J. M. Thijssen, “The impulse response of a focused source with an arbitrary axisymmetric surface velocity distribution,” *J. Acoust. Soc. Am.*, vol. 75, no. June, pp. 1716–1721, 1984.
[34] R. Salamon and B. Delannoy, “Acoustic diffraction analysis by the impulse response method: A line impulse response approach,” *J. Acoust. Soc. Am.*, vol. 76, no. May 2013, pp. 280–290, 1984.
[35] M. Arditi, F. S. Foster, and J. W. Hunt, “Transient fields of concave annular arrays,” *Ultrason. Imaging*, vol. 61, pp. 37–61, 1981.
[36] A. Penttinen and M. Luukkala, “The impulse response and pressure nearfield of a curved ultrasonic radiator,” *J. Phys. D. Appl. Phys.*, vol. 9, pp. 1547–1557, 1976.
[37] D. B. Bæk, J. A. Jensen, and M. Willatzen, “Spatial impulse response of a rectangular double curved transducer.,” *J. Acoust. Soc. Am.*, vol. 131, no. 4, pp. 2730–41, Apr. 2012.
[38] J. D’hooge, J. Nuyts, B. Bijnens, B. De Man, P. Suetens, and J. Thoen, “The calculation of the transient near and far field of a baffled piston using low sampling frequencies,” *J. Acoust. Soc. Am.*, vol. 102, no. 1, pp. 78–86, 1997.
[39] J. A. Jensen and N. B. Svendsen, “Calculation of Pressure Fields from Arbitrarily Shaped, Apodized, and Excited Ultrasound Transducers,” *IEEE Trans. ultrasound, Ferroelectr. Freq. Control*, vol. 39, no. 2, pp. 262–267, 1992.
[40] J. L. S. Emeterio and L. G. Ullate, “Diffraction impulse response of rectangular transducers,” *J. Acoust. Soc. Am.*, vol. 92, no. August, pp. 651–662, 1992.
[41] J. D’hooge, E. Konofagou, F. Jamal, A. Heimdal, L. Barrios, B. Bijnens, J. Thoen, F. Van de Werf, G. R. Sutherland, and P. Suetens, “Two-dimensional ultrasonic strain rate measurement of the human heart in vivo,” *Ultrason. Ferroelectr. Freq. Control. IEEE Trans.*, vol. 49, no. 2, pp. 281–286, 2002.
[42] H. Kanai and Y. Koiwa, “Myocardial rapid velocity distribution,” *Ultrasound Med. Biol.*, vol. 27, no. 4, pp. 481–498, 2001.
[43] P. Santos, L. Tong, A. Ortega, L. Løvstakken, E. Samset, and J. D’hooge, “Acoustic Output of Multi-Line Transmit Beamforming for Fast Cardiac Imaging :,” *Ultrason. Ferroelectr. Freq. Control. IEEE Trans.*, vol. 62, no. 7, pp. 1320–1330, 2015.
[44] T. Bruyneel, A. Ortega, L. Tong, and J. D’hooge, “A GPU-based implementation of the spatial impulse response method for fast calculation of linear sound fields and pulse-echo responses of array transducers,” *IEEE Ultrason. Symp. Proc.*, pp. 367–369, Jul. 2013.
[45] B. Denarie, T. Bjastad, and H. Torp, “Multi-line transmission in 3-D with reduced crosstalk artifacts: A proof of concept study,” *IEEE Trans. Ultrason. Ferroelectr. Freq. Control*, vol. 60, no. 8, pp. 1708–1718, 2013.
[46] A. Ortega, J. Provost, L. Tong, P. Santos, B. Heyde, M. Pernot, and J. D’hooge, “A comparison of the performance of different multi-line transmit setups for fast volumetric cardiac ultrasound,” *IEEE Trans. Ultrason. Ferroelectr. Freq. Control*, vol. 63, no. 12, pp. 1–1, 2016.
[47] A. Rabinovich, Z. Friedman, and A. Feuer, “Multi-line acquisition with minimum variance beamforming in medical ultrasound imaging,” *IEEE Trans. Ultrason. Ferroelectr. Freq. Control*, vol. 60, no. 12, pp. 2521–2531, 2013.
[48] R. Jasaityte, B. Heyde, and J. D’Hooge, “Current state of three-dimensional myocardial strain estimation using echocardiography,” *J. Am. Soc. Echocardiogr.*, vol. 26, no. 1, pp. 15–28, 2013.
[49] L. Demi, M. D. Verweij, and K. W. Van Dongen, “Parallel transmit beamforming using orthogonal frequency division multiplexing applied to harmonic imaging--a feasibility study,” *Ultrason. Ferroelectr. Freq. Control. IEEE Trans.*, vol. 59, no. 11, pp. 2439–2447, 2012.
[50] L. Demi, A. Ramalli, G. Giannini, and M. Mischi, “In Vitro and in Vivo tissue harmonic images obtained with parallel transmit beamforming by means of orthogonal frequency division multiplexing,” *IEEE Ultrason. Symp. Proc.*, vol. 62, no. 1, pp. 230–5, 2015.
[51] D. Barbosa, T. Dietenbeck, J. Schaerer, J. D’hooge, D. Friboulet, and O. Bernard, “B-spline explicit active surfaces: an efficient framework for real-time 3-D region-based segmentation.,” *IEEE Trans. Image Process.*, vol. 21, no. 1, pp. 241–51, 2012.
[52] J. Pedrosa, D. Barbosa, B. Heyde, F. Schnell, A. Rösner, Piet Claus, and J. D’hooge, “Coupling Strategies for Left Ventricular Myocardial Segmentation in 3D Ultrasound Recordings,” *Manuscr. Submitt. Publ.*
[53] F. Rademakers, J. Engvall, T. Edvardsen, M. Monaghan, R. Sicari, E. Nagel, J. Zamorano, H. Ukkonen, T. Ebbers, V. Di Bello, J.-U. Voigt, L. Herbots, P. Claus, and J. D’hooge, “Determining optimal noninvasive parameters for the prediction of left ventricular remodeling in chronic ischemic patients.,” *Scand. Cardiovasc.*

J., vol. 47, no. 6, pp. 329–34, 2013.
[54] A. Ramalli, A. Dallai, E. Boni, L. Bassi, V. Meacci, M. Giovannetti, L. Tong, J. D'hooge, and P. Tortoli, "Multi transmit beams for fast cardiac imaging towards clinical routine," *2016 IEEE Int. Ultrason. Symp.*, 2016.
[55] D. Barbosa, T. Dietenbeck, B. Heyde, H. Houle, D. Friboulet, J. D'hooge, and O. Bernard, "Fast and fully automatic 3D echocardiographic segmentation using B-spline explicit active surfaces: feasibility study and validation in a clinical setting," 2013.
[56] F. Orderud and S. I. Rabben, "Real-time 3d segmentation of the left ventricle using deformable subdivision surfaces," *Proc. Comput. Vis. Pattern Recognit. 2008*, 2008.
[57] F. Jurie, M. Dhome, and Others, "Real Time Robust Template Matching.," *Br. Mach. Vis. Conf.*, pp. 1–10, 2002.
[58] D. Barbosa, *Automated assessment of cardiac morphology and function: An integrated B-spline frame work for real-time segmentation and tracking of the left ventricle*. .
[59] Y. Chen, L. Tong, A. Ortega, J. Luo, and J. D'hooge, "Feasibility of multi-plane- transmit beamforming for real-time volumetric cardiac imaging: A simulation study," *IEEE Trans. Ultrason. Ferroelectr. Freq. Control*.

List of publications

Papers in peer-reviewed international journal

1. **A. Ortega**, L. Tong, and J. D'hooge, "A new analytic expression for fast calculation of the transient near and far field of a rectangular baffled piston.," *Ultrasonics*, vol. 54, no. 4, pp. 1071–7, Apr. 2014.

2. P. Santos, L. Tong, **A. Ortega**, L. Løvstakken, E. Samset, and J. D'hooge, "Acoustic Output of Multi-Line Transmit Beamforming for Fast Cardiac Imaging.," *IEEE Trans. Ultrason. Ferroelectr. Freq. Control*, vol. 62, no. 7, pp. 1320–1330, 2015.

3. **A. Ortega**, J. Provost, L. Tong, P. Santos, B. Heyde, M. Pernot, and J. D'hooge, "A comparison of the performance of different multi-line transmit setups for fast volumetric cardiac ultrasound," *IEEE Trans. Ultrason. Ferroelectr. Freq. Control*, vol. 63, no. 12, pp. 1–1, 2016.

4. Y. Chen, L. Tong, **A. Ortega**, J. Luo, and J. D'hooge, "Feasibility of multi-plane- transmit beamforming for real-time volumetric cardiac imaging: A simulation study.," *IEEE Trans. Ultrason. Ferroelectr. Freq. Control, Revision submitted for publication.*

5. **A. Ortega**, J. Pedrosa, B. Heyde, L. Tong, and J. D'hooge, "Anatomical beamforming for volumetric cardiac motion estimation at a high temporal resolution," *Applied Sciences, Revision submitted for publication.*

International conference proceedings

1. **A. Ortega**, L. Tong, and J. D'hooge, "A new analytical expression for fast calculation of the transient far field of a rectangular baffled piston," *IEEE Ultrason. Symp. Proc.*, pp. 1029–1032, 2013.

2. T. Bruyneel, **A. Ortega**, L. Tong, and J. D'hooge, "A GPU-based implementation of the spatial impulse response method for fast calculation of linear sound fields and pulse-echo responses of array transducers," *IEEE Ultrason. Symp. Proc.*, pp. 367–369, Jul. 2013.

3. L. Tong, **A. Ortega**, H. Gao, and J. D'hooge, "Fast three-dimensional ultrasound cardiac imaging using multi-transmit beamforming: A simulation study," *IEEE Ultrason. Symp. Proc.*, pp. 1456–1459, Jul. 2013.

4. **A. Ortega**, L. Tong, P. Santos, B. Heyde, and J. D'hooge, "Fast volumetric cardiac ultrasound : a comparison of different multi-line transmit setups by computer simulation," *IEEE Ultrason. Symp. Proc.*, pp. 2–5, 2014.

5. P. Santos, L. Tong, **A. Ortega**, L. Løvstakken, E. Samset, and J. D'hooge, "Safety of Multi-Line Transmit Beamforming for Fast Cardiac Imaging – A Simulation Study," *IEEE Ultrason. Symp. Proc.*, 2014.

6. **A. Ortega**, J. Pedrosa, B. Heyde, L. Tong, and J. D'hooge, "An automatic method for determining the anatomical relevant space for fast volumetric," *IEEE Ultrason. Symp. Proc.*, pp. 0–3, 2015.

7. **A. Ortega**, D. Lines, J. Pedrosa, B. Chakraborty, V. Komini, and H. Gassert, "HD-PULSE : High channel Density Programmable ULtrasound System based on consumer Electronics," *IEEE Ultrason. Symp. Proc.*, pp. 31–33, 2015.

8. C. Vallecilla, **A. Ortega**, M. Alessandrini, and J. D'hooge, "A simulation frame work to optimize volumetric cardiac imaging on a multiplexed system," *IEEE Ultrason. Symp. Proc.*, pp. 3–6, 2015.

9. L. Tong, **A. Ortega**, J. Luo and J. D'hooge, "Coded excitation for crosstalk suppression during multi-line transmit beamforming: a simulation study," *IEEE Ultrason. Symp. Proc.*, 2015.

Abstracts at international conference

1. L. C. Lervik Nilsen, B. Brekke, C. Missant, P. Haemers, L. Tong, **A. Ortega**, G. Sutherland, J. D'hooge, A. Stoylen, "Detection of mechanical activation by three-dimensional ultra-high frame rate tissue Doppler imaging in an open-chest pig model," *the Annual Meeting of the European Association of Cardiovascular Imaging (EuroEcho)* 2014.

2. L.C. Lervik Nilsen, B. Brekke, C. Missant, **A. Ortega**, P. Haemers, L. Tong, G. Sutherland, J. D'hooge, A. Stoylen, "Detection of mechanical activation by two-dimensional ultra-high frame rate tissue Doppler imaging in an open-chest pig model," the *Annual Meeting of the European Association of Cardiovascular Imaging (EuroEcho)* 2014.

3. C. Vallecilla, **A. Ortega**, and J. D'hooge, "The Matching algorithm for designing Multiplexed Ultrasound array transducers," *IEEE Ultrason. Symp. Proc.*, 2016.

4. Y. Chen, L. Tong, **A. Ortega**, J. Luo, and J. D'hooge, "Multi-plane- transmit beamforming for fast volumetric cardiac imaging – A simulation study," *IEEE Ultrason. Symp. Proc.*, 2016.